UNIVERSITÀ DEGLI STUDI DI NAPOLI

"FEDERICO II"

TESI DI DOTTORATO

IN FISICA FONDAMENTALE ED APPLICATA

CICLO XIII

Stellar Evolution and Nuclear Reaction Rates: an Experimental and Theoretical Study

Candidato: Gianluca Imbriani

Coordinatore: Prof. Renato Musto

Ringraziamenti

Non é stato facile portare a termine questa tesi di dottorato a metá strada fra uno studio teorico e uno sperimentale: spero di essere riuscito nell'ambizioso proposito di approfondire adeguatamente entrambi gli aspetti. Questo lavoro non sarebbe stato possibile senza l'aiuto decisivo di coloro che a suo tempo me lo proposero e che poi hanno collaborato alla sua realizzazione.

Il principale artefice é stato Filippo Terrasi al quale va tutta la mia stima e gratitudine per le opportunitá che mi ha dato in questi tre anni. La sua disponibilitá a capire e far capire tutti gli aspetti delle ricerche che affronta mi ha molto aiutato ad approfondire le mie conoscenze di fisica. Inoltre mi fa piacere ringraziare Antonio D'Onofrio, sempre pronto a dotarmi dei migliori mezzi necessari ai miei calcoli di evoluzione stellare; Mario Romano, per l'amicizia che mi ha sempre dimostrato; Enzo Roca, che durante un esperimento a Catania é stato il primo ad introdurmi alla fisica nucleare sperimentale e Luigi Campajola, per la fiducia e la stima dimostratami durante i turni presso l'acceleratore di Napoli.

Senza il prezioso aiuto di Alessandro Chieffi ed Oscar Straniero la parte di evoluzione stellare di questa tesi di dottorato sarebbe certo risultata meno efficace. Li ringrazio per i numerosi insegnamenti che sono sempre stati disponibili a darmi durante questi anni. Un sincero ringraziamento va anche a Marco Limongi, un "mago" del computer che mi ha sempre ben consigliato nella gestione dei programmi necessari ad analizzare un modello stellare.

Ringrazio, inoltre, Claus Rolfs per l'accoglienza sempre affettuosa che mi ha riservato e per l'esempio di una vita dedicata alla ricerca; colgo l'occasione per ringraziare

a Rocchina e Carmine

Table of Contents

Introduction

The sky appears to the terrestrial observer as an unchanging system, since the typical time scale on which stars evolve is much larger than the human life time. In fact, also the shortest living stars, i.e. the more massive ones [1], live a few million years, thanks to the nuclear burnings which are very efficient energy producers. These burnings can refurnish the stellar structure of the energy lost from the surface for a time proportional to the amount of nuclear "fuel" present in the core; therefore stars spend almost 90% of their life during the hydrogen burning phase. It follows that a large fraction of the stars we observe at night, are burning hydrogen. In spite of this, the more advanced burnings are of great importance, because they produce a large fraction of the nuclides with mass larger than helium. This material is spread in the interstellar medium either via stellar wind, or as a consequence of an explosion when these stars form an iron core (type II supernova) or when they explode as type I supernova.

Basic laws driving these events attain mainly to two branches of physics, astrophysics and nuclear physics. The synergic efforts in both theoretical and experimental research in these two domains have given rise, in the last decades, to the fascinating interdisciplinary field of nuclear astrophysics. The work described in the present thesis is intended to establish a modest contribution to the development of this field.

In particular we will focus our attention on two nuclear reactions: the first one, $^{7}Be(p, \gamma)^{8}B$, taking place in p-p III chain of hydrogen burning; the second, $^{12}C(\alpha, \gamma)^{16}O$, which is a key process in helium burning.

---

[1] Luminosity is proportional to the cubic mass.

A general and brief discussion about stellar equilibrium equations, inputs physics and mathematical tools needed to model the evolution of stars will be given in the first part of chapter I, while in the second part the main nuclear processes in stellar nucleosynthesis will be presented.

In the second chapter we will introduce the relevant nuclear inputs to evolutionary models and discuss the experimental problems encountered in their measurement. A more detailed description of the Recoil Mass Separator Method will be given in the last part of this chapter.

If one admits that the transformation of four protons in a helium nucleus is the basic mechanism by which the Sun replaces the energy lost from the surface (which amounts to $3.82 \cdot 10^{33} \ erg \cdot s^{-1}$), one would expect a neutrino flux (due to the conversion of two protons in neutrons for each of the nuclei produced). In the last forty years five experiments have taken data in different energy windows, and there is a clear evidence that the neutrino flux measured on earth is smaller than expected. As we will discuss in the third chapter, this discrepancy cannot be explained neither by exotic solar models nor by new nuclear cross section measurements. A way to reconcile neutrino observations with expected fluxes is to invoke a theory beyond the standard electroweak model. We will show in the first part of the third chapter how the prediction of a particular theory of neutrino oscillation (MSW) are influenced by the reaction rate of $^7Be(p,\gamma)^8B$, which is the most uncertain nuclear quantity in solar standard models. Moreover, the reaction rate of $^7Be(p,\gamma)^8B$ has been measured using a novel approach, the so called **Recoil Mass Separator** method, at the TTT-3 accelerator of Naples. The aim of this experiment, started in 1995, was to obtain a result not affected by some systematic uncertainties which could be present in previous measurements. We will resume briefly the advantages of this method and the production of a ^7Be radioactive beam together with the first measurements performed. Then, the part of the experiment and the analysis which have been performed in the framework of the present work will be described in detail in chapter III.

The $^{12}C(\alpha, \gamma)^{16}O$ process influences the evolution of a star essentially in two respects: first, it affects the He burning because it directly operates in this evolutionary phase, and, second, it determines all the further evolution of a star because it controls the chemical composition of the matter left by the He burning. Since all stars more massive than, say, $0.55M_\odot$ burn He, it is clear that the $^{12}C(\alpha, \gamma)^{16}O$ process will affect the evolution of stars in a very large mass interval. Theoretical efforts devoted to constrain the rate of this process on the basis of some "observables", as the solar abundances of carbon and oxygen, are useless since, unfortunately, this process works in a convective environment which may alter, also significantly, the final abundances of ^{12}C and ^{16}O. We will discuss in detail in chapter IV the influence of both the treatment of the convection and of the efficiency of the $^{12}C(\alpha, \gamma)^{16}O$ reaction rate in the central He burning of stars in a large mass range. From an experimental point of view, despite the enormous efforts devoted to the measurement of this cross section, the corresponding rate at astrophysical energies is still far from being well established. We plan to measure the $^{12}C(\alpha, \gamma)^{16}O$ using the same approach as above, i.e. the Recoil Mass Separator in inverse kinematics. We will discuss the peculiarities of this reaction which require a modification of the apparatus and we will report on the project of the new device which is being installed at the Dynamitron Tandem Laboratory in Bochum (Germany). In the last part of the chapter IV we will describe in detail some preliminary measurements performed in the present work, which characterize the apparatus and allow a project of the experiment, which aims to extend the explored energy range and to provide information both on the total cross section and the $E1$ and $E2$ amplitudes.

Chapter 1

Quiescent burnings and stellar nucleosynthesis

The understanding of stellar evolution and nucleosynthesis largely improved in the last 50 years, starting with the pioneering works of W. A. Fowler, G. R. Burbidge, E. M. Burbidge and Hoyle [52, 41, 19]. We know the basic laws and the main physical processes, which drive the evolution of stars. Unfortunately fundamental uncertainties are still present concerning e.g. critical quantities as the opacity, the treatment of convection and the reaction rate of processes involved in stellar nucleosynthesis. In fact, in spite of enormous efforts, the only nuclear reaction studied down to the energy of the Gamow peak is the $^{3}He(^{3}He, 2p)^{4}He$ [15].

In this chapter we will firstly derive the physical equations and present the input physics needed to follow the evolution of a star(sections 1.1 and 1.2); secondly, we will describe the mathematical technique we chose to solve the stellar equations (section 1.3); and, last, we will present the main nuclear processes which drive stellar nucleosynthesis.

1.1   Stellar evolution equations

Star may be modeled as self-gravitating spherical objects, in hydrostatic equilibrium. This means that in every point the gravitational force (F_G) must be equilibrated by the pressure force (F_p) [24], for a generic volume dV of edge dr and surface dS and mass dm:

$$G\frac{M_r \cdot dm}{r^2} = F_G = F_p = (P_{r+dr} - P_r) \cdot dS \qquad (1.1)$$

Substituting $dV = dS \cdot dr$ and $dm = \rho \cdot dS \cdot dr$ we obtain the equation of hydrostatic equilibrium:

$$\frac{dP}{dr} = -G\frac{M_r(r)\rho(r)}{r^2} \qquad (1.2)$$

The unknowns of this relation are $P(r)$, M_r and $\rho(r)$. The mass is obviously related to the radius by the equation of continuity:

$$\frac{dM}{dr} = 4\pi r^2 \rho(r) \qquad (1.3)$$

If the equation of state were just a relation between P and ρ (how it actually is in some specific cases), the system would be closed. The equation of state introduces another unknown, the temperature: one is forced to add a new equation.

In principle, the temperature gradient depends on the heat transport mechanism which can be radiative, conductive or convective. In absence of convective motions radiation is driven by photons and conduction by electrons; in absence of degeneration the first mechanism is much more efficient than the conduction. Therefore, if the matter does not contribute to the transport, the temperature gradient is proportional to the photon flux multiplied by the opacity (section 1.2) of the matter, which measures the heat flux resistance ($dT/dr \propto F \cdot \kappa$). The photon flux depends on the mean free path λ and on the pressure gradient:

$$F = \lambda c\frac{dP}{dr} = \lambda c\frac{4a}{3}T^3\frac{dT}{dr} \qquad (1.4)$$

where c is the light speed. We have used the equation of state of an adiabatic thermodynamic system ($P = aT^4/3$ see again section 1.2) and a is the black body constant ($a = 7.6 \cdot 10^{10} erg \cdot cm^{-3} K^{-4}$). From equation 1.4 one can easily obtain:

$$\frac{dT}{dr} = -\frac{3\kappa\rho(r)}{4acT^3}F \qquad (1.5)$$

reminding that $\lambda = 1/(\kappa\rho)$.

Introducing the energy which following a spherical surface $L(r) = 4\pi r^2 F(r)$ (**luminosity**) equation 1.5 becomes:

$$\frac{dT}{dr} = -\frac{3\kappa L_r \rho(r)}{16\pi acr^2 T^3} \qquad (1.6)$$

The appearance of a further quantity, the luminosity, requires the inclusion of a fourth equation, which is simply the energy conservation:

$$\frac{dL_r}{dr} = 4\pi r^2 \rho(r)\epsilon \qquad (1.7)$$

The variation of the energy dL_r implies a production or a destruction of energy (ϵ) in the mass layer $4\pi r^2 \rho(r)$. In general three are the energy contributions: the energy is produced (or consumed) by the nuclear reactions, the energy is lost via neutrino emission and the gravitational energy changes.

Summarising, in order to study the stellar evolution in absence of convective motions it is necessary to solve the 4 differential equation system:

1. *hydrostatic equilibrium* $\mathbf{\frac{dP}{dr}} = -\mathbf{\frac{GM_r(r)\rho(r)}{r^2}}$;

2. *mass continuity* $\mathbf{\frac{dM_r(r)}{dr}} = \mathbf{4\pi r^2}\rho(\mathbf{r})$;

3. *radiative heat transport* $\mathbf{\frac{dT}{dr}} = -\mathbf{\frac{3\kappa L_r \rho(r)}{16\pi acr^2 T^3}}$;

4. *energy conservation* $\mathbf{\frac{dL_r}{dr}} = 4\pi r^2 \rho(r)\epsilon$;

The unknowns are $M_r(r)$, $P(r)$, $L_r(r)$, $T(r)$, $\rho(r)$, $\kappa(r)$ and $\epsilon(r)$. Therefore to solve the system it is necessary to know some input physics: the equation of state $P = P(\rho, T)$,

the opacity coefficient $\kappa = \kappa(\rho, T)$ and the energy coefficient $\epsilon = \epsilon(\rho, T)$. When convection takes place the third equation changes, as we will see in section 1.2.2.

This system describes the equilibrium of a star at a certain time. The temporal changing of the chemical composition within a star is described by the equations:

$$\frac{dY_i}{dt} = \sum_j c_i(j)\lambda_j Y_i + \sum_{j,k} c_i(j, k)\rho N_A <\sigma v>_{j,k} Y_j Y_k +$$
$$\sum_{j,k,l} c_i(j, k, l)\rho^2 N_A^2 <\sigma v>_{j,k,l} Y_j Y_k Y_l \quad i = 1, \cdots, N \quad (1.8)$$

which schematically describe the temporal variation of N nuclear species. The different terms stand for:

1. β-decays, electron captures and photo disintegrations;

2. two body reactions (for instance $^{12}C(\alpha, \gamma)^{16}O$);

3. three body reactions (for instance $^4He(2\alpha, \gamma)^{12}C$).

The coefficients c_i are given by $c_i(j) = \pm N_i$, $c_i(j, k) = \pm N_i/(N_j!, N_k!)$ and $c_i(j, k, l) = \pm N_i/(N_j!, N_k!, N_l!)$, where N_i is an absolute number indicating how many particles i are involved in the reaction, and N_i prevents double counting for reactions involving identical particles. The sign depends on whether the particle i is produced (+) or destroyed (-). As usual, λ stands for the weak interaction or photo disintegration rate, while $N_A <\sigma v>$ stands for the two - or three - body reaction rate (see cap. 2).

1.2   Input physics

As mentioned above, the integration of the equations of the stellar equilibrium requires the knowledge of the equation of state, opacity, energy losses and energy gains as a function of temperature, density and chemical composition in the typical condition met in the interior of a star.

1.2.1 Equation of state and opacity

The plasma stellar pressure can be divided in three components: the ion pressure, electron pressure and radiation pressure

$$P = P_i + P_e + P_r \tag{1.9}$$

Usually the first two terms are called gas pressure. If the Coulomb interaction energy is negligible compared with the kinetic energy, then ions and electrons of the stellar plasma can be considered as free non interacting particles. The condition is:

$$kT >> \frac{(Ze)^2}{d} \tag{1.10}$$

where d is the particle average distance. If we consider ions, the density is:

$$\rho = N_i \mu H \tag{1.11}$$

$$
\begin{aligned}
N_i &\equiv \; ions\,number\,per\,unit\,volume \\
\mu &\equiv \; ions\,molecular\,weight \\
H &\equiv \; hydrogen\,weight
\end{aligned}
$$

Assuming $d_{i,i}$ as ion-ion average distance, then $N_i = 1/d_{i,i}^3$; and:

$$d_{i,i} = (\frac{\mu H}{\rho})^{1/3} \tag{1.12}$$

Now it is possible to re-write the condition:

$$\rho << 4 * 10^{-14} \frac{T^3}{Z^6} gr\,cm^{-3} \tag{1.13}$$

which is largely satisfied during hydrogen burning ($T \sim 10^7 K$, $Z = 1 \implies \rho << 4 * 10^7 gr\,cm^{-3}$) and helium burning ($T \sim 10^8 K$, $Z = 2 \implies \rho << 6 * 10^9 gr\,cm^{-3}$), but not during carbon burning ($T \sim 10^9 K$, $Z = 6 \implies \rho << 8 * 10^8 gr\,cm^{-3}$). For electrons it is enough to underline that the density to compare will be larger, since the distances and the Coulomb attraction decreases.

Stellar plasma is a particle gas and using statistical mechanics it is possible to deduce particle numbers and internal energy [68]:

$$N = \int_0^\infty f(p)g(p)dp \tag{1.14}$$

$$E = \int_0^\infty \varepsilon_p f(p)g(p)dp \tag{1.15}$$

$$
\begin{aligned}
p &\equiv \quad is\ the\ momentum \\
\varepsilon^2 &= \quad p^2c^2 + m^2c^4\ is\ the\ particle\ energy \\
f(p) &\equiv \quad is\ the\ probability\ of\ \varepsilon_p\ energy\ state \\
g(p)dp &= \quad g_s\frac{V4\pi p^2}{h^3}dp\ is\ the\ state\ density\ between\ p\ e\ p+dp
\end{aligned}
$$

Using the first law of thermodynamics:

$$dE = TdS - PdV + \varepsilon_\mu dN \tag{1.16}$$

then:

$$P = -(\frac{\partial E}{\partial V})_{S,N} = -(-\frac{1}{3V}) \int_0^\infty 4\pi p^3 v_p f(p)g_s\frac{V}{h^3}dp \tag{1.17}$$

$$
\begin{aligned}
\frac{d\varepsilon_p}{dV} &= \frac{d\varepsilon_p}{dp}\frac{dp}{dV} = \frac{pc^2}{\varepsilon_p}(-\frac{p}{3V}) \\
v_p &= \frac{pc^2}{\varepsilon_p}
\end{aligned}
$$

The function $f(p)$ defines the distribution:

$$f(p) = \frac{1}{e^{\frac{\varepsilon_p - \varepsilon_\mu}{kT}} + 1} \implies Fermi - Dirac\ particles \tag{1.18}$$

$$f(p) = \frac{1}{e^{\frac{\varepsilon_p - \varepsilon_\mu}{kT}} - 1} \implies Bose - Einstein\ particles \tag{1.19}$$

Both distributions for $f(p) << 1$ approach the one for classical (or Maxwell-Boltzamann) particles:

$$f(p) \cong e^{-\frac{\varepsilon_p - \varepsilon_\mu}{kT}} \tag{1.20}$$

In this condition:

$$P = -(-\frac{1}{3V})e^{-\frac{mc^2 - \varepsilon_\mu}{kT}} \int_0^\infty 4\pi p^4 e^{-\frac{p^2}{2mkT}} g_s \frac{V}{mh^3} dp =$$
$$= kT e^{\frac{\varepsilon_\mu - mc^2}{kT}} g_s \frac{(2\pi mkT)^{3/2}}{h^3} \tag{1.21}$$

using:

$$N = e^{\frac{\varepsilon_\mu - mc^2}{kT}} g_s \frac{V(2\pi mkT)^{3/2}}{h^3} \tag{1.22}$$

we obtain:

$$P = \frac{kTN}{V} \tag{1.23}$$

which is the perfect gas equation.

Quantistic degeneration appears if particle wavelength is of the same order of magnitude as the particle distance ($\lambda = \hbar/p \sim d_{i,i}$). It is easy to show that electrons are the first to feel quantistic effects. In fact, from the equipartition energy principle $m_i v_i^2 = m_e v_e^2$, it follows that:

$$p_i = (\frac{m_i}{m_e})^{1/2} p_e. \tag{1.24}$$

Since ion mass is 1836 times larger than electron mass, then electron wavelength is always much larger then ion one.

Assuming classical non interacting particles, gas pressure is:

$$P_{gas} = P_i + P_e = \left(\frac{N_i + N_e}{V}\right)kT = (n_i + n_e)kT = \frac{k\rho T}{\mu_i H} + \frac{k\rho T}{\mu_e H} \tag{1.25}$$

Using X, Y and Z for chemical abundance of hydrogen, helium and heavy elements, the previous formula for fully ionized matter becomes:

$$P_{gas} = \frac{k\rho T}{H}\left(2X + \frac{3}{4}Y + \frac{Z}{2}\right) \tag{1.26}$$

Radiation pressure is due to photons, which are Bose-Einstein particles and using equations 1.17 and 1.19:

$$P_{rad} = \frac{1}{3}\int_0^\infty h\nu n(\nu)d\nu = \frac{8\pi}{3c^3}\int_0^\infty h\nu \frac{\nu^2}{e^{\frac{h\nu}{kT}} - 1} = \frac{a}{3}T^4 \tag{1.27}$$

where $a = \frac{8\pi k^4}{15h^3c^3}$.

Reassuming, the pressure for classical free no interacting particles is:

$$P = P_{gas} + P_r = \frac{k\rho T}{\mu_i H} + \frac{k\rho T}{\mu_e H} + \frac{a}{3}T^4 \qquad (1.28)$$

The value of equation of state (EOS) used for stellar calculation is the one described by [98] and updated by [94]. Above Log $T = 6.0$ the matter is assumed to be completely ionized, while below such a value partial ionization is taken into account. In the high temperature regime the electron degeneracy, relativistic effects, electron positron pair creation and Coulomb interactions are taken into account. Below such threshold temperature value the ionization stage of both the nuclei and the molecules are derived from the classical Saha equation.

We have already mentioned the existence of a thermal gradient which implies an energy flux, whose largest part is transported by photons. Photons can interact with the matter and the opacity (κ) is a parameter related with the number of interaction per length unity $\kappa\rho \equiv 1/\lambda$, where ρ is the density and λ free mean path. The interaction mechanisms briefly are:

- *Electron Scattering*: photon diffusion from free electron in stellar plasma. Two are the possible approximations: Thompson Scattering, non-relativistic isotropic; Compton Scattering, relativistic.

- *Bound-bound processes*: photon absorption from a bound electron which gains energy still remaining bound.

- *Bound-free processes*: photon absorption from a bound electron which becomes free, this is the well known photoelectric effect.

- *Free-free processes*: photon absorption from a free electron.

Theoretical calculations of opacity is complex, since one must know in detail the equation of state, the electron distribution and all the possible quantistic correction for photon-matter interaction. Experimental tabulations were done during nuclear

explosion tests in Los Alamos [53] which give opacities for different chemical compositions varying ρ and T. In 1992 new tabulations appeared from Roger & Iglesias [88].

The radiative opacity coefficients are derived from [67] for $T \leq 10^4$ K, from [56] (OPAL) for 10^4 K $< T \leq 10^8$ K, and from the Los Alamos Opacity Library (LAOL) [53] for 10^8 K $< T \leq 10^{10}$ K. The heavy element solar mixture of [48] has been adopted. The opacity coefficients due to the thermal conductivity are derived from [58].

1.2.2 Schwartzschild criterion for convection

The set of equations discussed in section 1.1 have been obtained under the assumptions that all the energy is transported by the photons. This is not always true. Let us consider an element of matter, a bubble, and let move it, e.g. upwards, adiabatically. Since the bubble must remain in hydrostatic equilibrium, the pressure of the surface of the bubble must equate that of the surroundings, i.e. the relation: $P_b = \frac{k\rho_b T_b}{\mu m_H} = P_s = \frac{k\rho_s T_s}{\mu m_H}$ must be verified, which means that $\rho_b T_b = \rho_s T_s$. This means that, if the temperature of the matter with in the bubble is lower than in the surrounding its density will be larger and hence the bubble will fall back toward its initial position: the layer is in this case stable with respect to the grow of convective motions. On the contrary, if the temperature in the bubble is larger, the density will be smaller and the bubble will be accelerated away from its equilibrium position. In this case convective motions form. Hence, in a chemically homogeneous region, the condition for the growth of convective instabilities may be written as:

$$\left| \frac{dr}{Td\ln P}\frac{dT}{dr} \right|_{rad} = \left| \frac{d\ln T}{d\ln P} \right|_{rad} = \nabla_{rad} > \nabla_{ad} = \left| \frac{d\ln T}{d\ln P} \right|_{ad} \qquad (1.29)$$

This is usually called the Schwartzschild criterion for the stability analysis of the various layers within a star. If the composition of the layer is not homogeneous but there is a gradient of chemical composition, then the criterion for the growth of

convective instabilities becomes:

$$\nabla_{rad} > \nabla_L = \nabla_{ad} + \frac{d\ln T}{d\ln \mu}\frac{d\ln \mu}{d\ln P} \tag{1.30}$$

In any case since the convective bubbles transport heat very efficiently it can be assumed, from a practical point of view, that the adiabatic gradient is the "real" one in presence of convective motions. In this case the equation 1.5 becomes:

$$\frac{d\ln T}{d\ln P} = \nabla_{ad} \tag{1.31}$$

1.2.3   Energy coefficient

Whenever in the star a neutrino is created, it escapes from the surface subtracting energy to the structure. Generally speaking, stellar neutrinos can be divided into two groups: the ones due to interaction between matter and radiation (thermo neutrinos), and the ones due to nuclear reactions ($\beta-$decays and electron captures).

The processes which belong to the thermo neutrinos are:

- $\gamma + e^{\pm} \rightarrow e^{\mp} + \nu + \overline{\nu}$ **photo-neutrino**;

- $e^+ + e^- \rightarrow \nu + \overline{\nu}$ **pair-neutrino**;

- $\gamma_{plasma} \rightarrow \nu + \overline{\nu}$ **plasma-neutrino**;

- $e^- + Z \rightarrow e^- + Z + \nu + \overline{\nu}$ **bremstralung-neutrino**.

Figure 1.1 [49] shows where the above processes are active in the density temperature plane. In the code which we have used, the energy loss due to photo, pair and plasma neutrinos are properly taken into account following [74] (corrected as reported by [75]). The Weinberg angle is also taken from [74] where three neutrino flavors are included. Bremsstrahlung neutrinos are taken into account following [35] (corrected by [85]) who extended the results obtained by [38] by the inclusion of the neutral current effects. The energy loss due to the recombination processes are included following the prescriptions of [13]. The other neutrino processes are enclosed in the more general nuclear treatment.
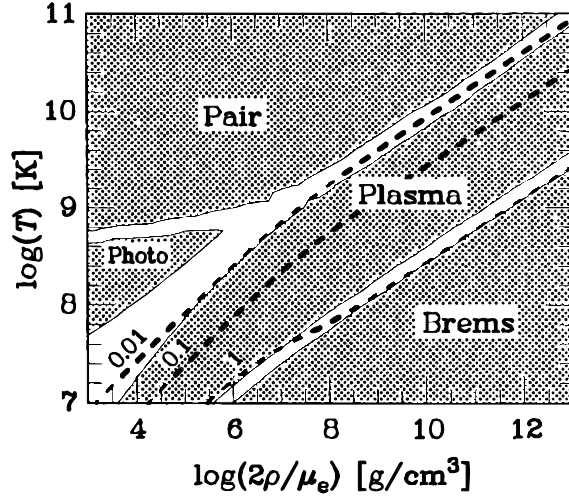
Figure 1.1: **The figure raprensets in the** $Log(t) \div Log(\rho)$ **plane the zones in which the neutrino processes take place.**

Though we will fully discuss nuclear energy generation rates in chapter 2, let us here briefly remind that the evolution of the model presented in this thesis has been obtained by adopting a network including $N = 149$ nuclear species ranging from neutron up to ^{67}Zn. This network is well suited for all the advanced nuclear burnings, ranging from carbon to silicon included. Each isotope is linked to its neighbors by means of all possible binary interactions involving the capture or the release of a proton, neutron, α-particle or photon. In addition to that, all possible links due to the weak interactions (electron or positron captures and β-decays) are taken into account. Also included are the triple-α, ^{12}C $+^{12}$ C, ^{12}C $+^{16}$ O and ^{16}O $+^{16}$ O reactions.

Nuclear reaction cross sections (see next chapter) for strong and electro-magnetic interactions are computed using Thielemann prescriptions, using his tabulation. In particular the reactions are:

- β-decays, electron captures $(a \rightarrow b)$;

- photo disintegrations and neutron β emissions $(a \rightarrow b + c)$;

- three body inverse reactions and two neutrons β emission $(a \rightarrow b + c + d)$;

- charged particle captures with photon γ emission $(a + b \rightarrow c)$;

- charged particle captures with charged particle emission p, n, or α $(a + b \rightarrow c + d)$;

- charged particle captures with two charged particle emission p, n, or α $(a + b \rightarrow c + d + e)$;

- charged particle captures with three charged particle emission p, n, or α $(a + b \rightarrow c + d + e + f)$;

- three body reactions $(a + b + c \rightarrow d \ (+e))$;

In Thielmann tabulation most recent experimental [26, 107, 10, 105, 71] and theoretical data [103, 29] are collected for nuclear cross sections with masses included between $1 \leq A \leq 106$. Data are organized in tables and for each process seven coefficients are given for the interpolating formula of the astrophysical factor:

$$S = exp[A_1 + \frac{A_2}{T_9} + \frac{A_3}{T_9^{1/3}} + A_4 \cdot T_9^{1/3} + A_5 \cdot T_9 + A_6 \cdot T_9^{5/3} + A_7 \cdot \ln(T_9)] \qquad (1.32)$$

where $T_9 = T/10^9 \ K$.

Using this formula experimental data are reproduced in the range of temperature $10^7 \ K \leq T \leq 10^{10} \ K$ with 1% of accuracy in the largest part of reactions. Theoretical data are computed in the temperature range $10^8 \ K \leq T \leq 10^{10} \ K$ and can be extrapolated up to $10^7 \ K$. As we will see in details in the fourth chapter, we use for the $^{12}C(\alpha, \gamma)^{16}O$ cross section also data from [25].

Electronic decay and capture rates are computed using the work of Fuller, Fowler and Newmann [42], for nuclides with mass number $21 \leq A \leq 60$ and Thielemann tabulations for the other nuclides. Screening effects are taken into account using formulations of Graboske, De Witt, Grossman e Cooper [47, 34] and Itoh, Totsuji ed Ichimaru [59, 60].

1.3 The stellar evolution code FRANEC

All the calculations necessary for this thesis, have been obtained by means of the FRANEC code (Frascati RAphson Newton Evolutionary Code) [28, 27]. In the following sections we will briefly describe the main features of this code.

The stellar model is divided in three portions. The most external layers is the **atmosphere**, where each photon has the probability to undergo at most one interaction before leaving the star. This propriety define the optic thickness τ, which is, also, the natural integration variable within atmosphere. Since in this external layer $M_r = M$, $L_r = L$ and $r = R$, the equations to solve become:

$$
\begin{aligned}
\frac{dP}{d\tau} &= \frac{g}{\kappa(\rho,T)} \\
T &= T(\tau, T_{eff}) \\
P &= P(\rho,T)
\end{aligned}
$$

where g is the gravity acceleration on the star surface and T_{eff} is the temperature at $\tau = \frac{2}{3}$ (effective temperature). In the black body approximation it is possible to define the so called "gray atmosphere", and above equation becomes:

$$
T^4(\tau, T_{eff}) = \frac{1}{2}T_{eff}^4 (1 + \frac{3}{2}\tau)
$$

A more detailed approximation is the semi empirical one given by Böhm-Vitense, which takes in to account the Balmer absorption line using solar observations:

$$
T(\tau) = T_{eff}^4 [\frac{3}{4}(\frac{T_{eff}'}{T_{eff}})^4(\tau + 0.727 - 0.146 e^{-2.542\tau}) - B\, e^{-30\tau}] \qquad (1.33)
$$

where

$$
\frac{T_{eff}'}{T_{eff}} = 1.17(T_{eff} * 10^{-4} - 1.1)^4 + 1.046
$$

$$
B = 0.440(\frac{T_{eff}'}{T_{eff}})^4 - (\frac{T_\odot}{T_{eff}})^4
$$

In some stellar codes the values of the parameters at the base of the atmosphere are given as an input boundary condition, using the results of the integration of a set of model atmospheres.

When $\tau = 2/3$ begins the second layer of the star (**sub atmosphere**), which has the pressure, as natural variable of integration, and which includes the 0.1 % of the stellar mass. In this point it is, also, defined the effective temperature T_{eff} of a star by the relation:

$$L = 4\pi R^2 \sigma T_{eff}^4 \qquad (1.34)$$

The remaining 99.9 % is integrated using the lagrangian coordinate mass. In the sub atmosphere and in the interior we solve the complete set of equation, which are:

$$
\begin{aligned}
\frac{dP}{dM_r} &= -\frac{GM_r}{4\pi r^4} \\
\frac{dr}{dM_r} &= \frac{1}{4\pi r^2 \rho} \\
\frac{dT}{dM_r} &= \nabla \frac{GM_r T}{4\pi R^2 P} \\
\frac{dL_r}{dM_r} &= \epsilon_{grav} + \epsilon_{nucl} + \epsilon_\nu \\
\frac{dY_i}{dt} &= \sum_j c_i(j)\lambda_j Y_i + \sum_{j,k} c_i(j,k)\rho N_A < \sigma v >_{j,k} Y_j Y_k + \\
&\quad \sum_{j,k,l} c_i(j,k,l)\rho^2 N_A^2 < \sigma v >_{j,k,l} Y_j Y_k Y_l \qquad i = 1, \cdots, N
\end{aligned}
$$

The boundary conditions are:

$$
\begin{aligned}
for \quad m = 0 &\implies \quad R_m(0) = 0 \qquad L_m(0) = 0 \\
for \quad m = M &\implies \quad P_m(M) = P_{atm} \quad T_m(M) = T_{atm} \\
for \quad t = 0 &\implies \quad Y_i(t = t_0) = Y_i^0 \quad i = 1, \cdots, N
\end{aligned}
$$

These boundary conditions are placed partly at the center and partly on the surface of the star, so that we need to integrate both from center and surface, using 4 testing starting values for the unknown parameters T_c, P_c, L and R. The numerical technique used to solve the system is the so called Raphson-Newton method. For this purpose we divide the model in n meshes and in each mesh we have to zero the $\delta_{i,k}$ which are

(Henyey technique):

$$\frac{dP}{dM} + \frac{GM}{4\pi r^4} \simeq \frac{(P_{k+1}-P_k)}{M_{k+1}-M_k} - \frac{GM_k}{4\pi r_k^4} = \delta_{1,k}$$

$$\frac{dr}{dM} + \cdots\cdots \simeq \cdots\cdots\cdots\cdots = \delta_{2,k}$$

$$\frac{dT}{dM} + \cdots\cdots \simeq \cdots\cdots\cdots\cdots = \delta_{3,k}$$

$$\frac{dL}{dM} + \cdots\cdots \simeq \cdots\cdots\cdots\cdots = \delta_{4,k}$$

$$\frac{dY_i}{dt} + \cdots\cdots \simeq \cdots\cdots\cdots\cdots = \delta_{4,k}$$

To do this we have to solve the system formed by $N + 4$ equations in $N + 8$ unknowns whose template is given by:

$$\delta E_k^i = \sum_{j=1}^{N} \frac{\partial E_k^i}{\partial Y_{j,k}} \delta Y_{j,k} +$$

$$\frac{\partial E_k^i}{\partial R_k} \delta R_k + \frac{\partial E_k^i}{\partial L_k} \delta L_k + \frac{\partial E_k^i}{\partial P_k} \delta P_k + \frac{\partial E_k^i}{\partial T_k} \delta T_k +$$

$$\frac{\partial E_{k+1}^i}{\partial R_{k+1}} \delta R_{k+1} + \frac{\partial E_{k+1}^i}{\partial L_{k+1}} \delta L_{k+1} + \frac{\partial E_{k+1}^i}{\partial P_{k+1}} \delta P_{k+1} + \frac{\partial E_{k+1}^i}{\partial T_{k+1}} \delta T_{k+1} = -\Delta_k^i$$

$$i = 1, \cdots, N + 4 \quad (1.35)$$

where Δ_k^i is the difference between the two members of the $i-th$ linearized equation which must be zeroed in order to solve the system. The first N terms are the derivatives of the equations with respect to the N isotope abundances, while the next 8 terms are the derivatives of the equations with respect to the physical variables (R, L, P and T) corresponding to the adjacent mesh points k and $k + 1$. The chemical composition, between two adjacent mesh points k and $k + 1$, is assumed to be constant and equal to the one corresponding to the mesh k.

1.3.1   Convection treatment

Convective regions are fixed by means of the Schwarzschild (or Ledoux) criterion. Chemical mixing in the convective regions is usually obtained by assuming $\tau_{mix} <<$

τ_{burn}, so that one can write for each isotope:

$$\overline{Y}_i = \frac{1}{\Delta M_C} \sum_k \frac{Y_{i,k} + Y_{i,k+1}}{2}(M_{k+1} - M_k) \tag{1.36}$$

where k is k^{th} mesh in which the convective shell is divided.

This assumption is true during the H and He burnings which are the longest phase of stellar evolution, but not during advanced phases where $\tau_{mix} \sim \Delta t$ and $\tau_{mix} \sim \tau_n$. To solve the first problem it is possible to add a coefficient proportional to the exponential of the ratio between mixing time scale $\tau_{mix}^{k,j}$ of generic k and j meshes and stellar time scale Δt [92]:

$$Y_i = Y_i^o + \frac{1}{\Delta M_C} \sum_j (Y_{i,j} - Y_{i,k})(M_{k+1} - M_k)e^{-\tau_{mix}^{k,j}/\Delta t} \tag{1.37}$$

where $Y_{i,k}^o$ is the initial of isotope i. If $\tau_{mix} \ll \Delta t$ the exponential term is 1 then eq. 1.37 is equal to the 1.36 (flat mixing), otherwise a partial mixing occurs. The mixing time between two adjacent k e j convective meshes is:

$$\tau_{mix}^{k,j} \simeq \frac{\mid R_j - R_k \mid}{\overline{v}_{k,j}} \tag{1.38}$$

where $\overline{v}_{k,j} = \frac{v_k + v_j}{2}$ is the convective bubble average velocity.

To solve correctly the second problem one should couple mixing and nuclear burning, introducing in the equation 1.8 another term, i.e. the diffusion one. Equation 1.8 should be rewritten as:

$$\frac{dY_i}{dt} = \left(\frac{\partial Y_i}{\partial t}\right)_{nuc} + \frac{\partial}{\partial M}\left[(4\pi R^2 \rho)^2 D \frac{\partial Y_i}{\partial M}\right] \tag{1.39}$$

Parameter D is the so called diffusion coefficient, which is almost a free parameter since there is no observational possibility to measure it.

An effective way in which it is possible to simulate the coupling between mixing and nuclear burning is to firstly mix the matter according to eq. 1.36 and then to further evolve locally the matter for a timescale $\Delta\tau$ equal to τ_{mix}. In this way the isotopes where burning timescale is shorter than mixing turnover time will settle at the local equilibrium, while those for which $\tau_{nuc} >, \tau_{mix}$ will be practically unaffected by this further local evolution.

1.4 The stellar nucleosynthesis

In this section we will discuss the main nuclear processes which occur during the evolution of a star to underline how much the evolution and our knowledge of the stellar physics depends on the nuclear reaction rate adopted. We will study in depth these interconnections in the third and fourth chapters by means of two particular processes: the reaction $^7Be(p,\gamma)^8B$ which takes place in the hydrogen burning; and of the reaction $^{12}C(\alpha,\gamma)^{16}O$ which takes place in the helium burning.

The first reaction plays a key role, since the following boron decay produces an high energy neutrino ($E_\nu \sim 15 MeV$), which is measured by Superkamiokande experiment (see chapter 3). A change in the value of the cross section of this reaction could be crucial to understand if we need physics beyond the standard electroweak model to change the neutrino energy spectrum once the neutrinos are produced in the center of the sun.

The second is one of the most studied and unknown reactions in nuclear astrophysics field and it plays a key role in determining the advanced evolutionary phases of a star. The carbon and oxygen abundances at the end of helium burning, in fact, drastically depend on the adopted values of the reaction rate. The choice of a given value means the choice of an evolution with more or less oxygen in the advanced burnings. How we will largely discuss in chapter 4 this is a crucial point in stellar evolution. In addition to that we will discuss also the possibility that a better measurement of $^{12}C(\alpha,\gamma)^{16}O$ reaction rate could constrain our knowledge about the real extension of the convective core.

Coming back to the purpose of this section we will describe the quiescent nucleosynthesis which starts thanks to the protostellar contraction, which strongly increases the gas pressure. Once the star reaches the hydrostatical equilibrium, the virial theorem becomes $2K + \Omega = 0$. If $E = K + \Omega$ is the total energy, substituting in the virial relation, we obtain:

$$E = \frac{1}{2}\Omega \qquad\qquad (1.40)$$

When the star contracts, as the gravitational energy decreases by an amount $\Delta\Omega$, the total energy decreases by $\Delta E = 1/2\Delta\Omega$ and the kinetic energy increases by $\Delta K = -1/2\Delta\Omega$. This means that one half of the energy is radiated and one half is needed to increase the temperature. This is the *Premainsequence* (**PMS**) phase and the characteristic time scale is the thermodynamic one, defined by the Kelvin-Helmoltz formula $t_{KH} = \frac{GM^2}{RL}$ ($\sim 10^7 yr$). During the PMS the central temperature increases, reaching the condition to burn Deuterium, Berillium, Boron, Lithium and ^3He. These elements reach the equilibrium abundances before the reaction p+p starts, since this is a weak process which needs a higher temperature to become efficient. Thanks to this property and to the initial mixing, it is possible to follow the star evolution starting from the end of PMS choosing a mass and an initial chemical composition.

1.4.1 Hydrogen burning

The contraction ("gravitational") phase ends when the progressive increase of the temperature allows the fusion of four protons in He nucleus. This process is energetic enough that the star stops contracting on a thermal timescale and a long lasting phase begins in which the energy losses from the surface are replaced by the energy produced by the fusion of protons in He: this is the so called Main Sequence (MS) phase. Since a long time it has been recognized that the fusion of the hydrogen in He may occur by means of two different sequences of processes: the pp chain and the CNO cycle. The two sequences are shown in fig 1.2 and fig. 1.4, respectively. Fig. 1.3 shows the efficiencies of the two sequences as a function of the temperature. The pp chain becomes efficient well before the CNO cycle because the Coulomb barrier is much lower in this case but it does not increase very much with temperature (because the leading reaction is mediated by a weak process which is mildly dependent on the temperature). In the CNO cycle, vice versa, the processes are characterized by a stronger Coulomb barrier so that it becomes efficient at temperature larger than the pp chain but it increases much more steeply with the temperature. Let us look each
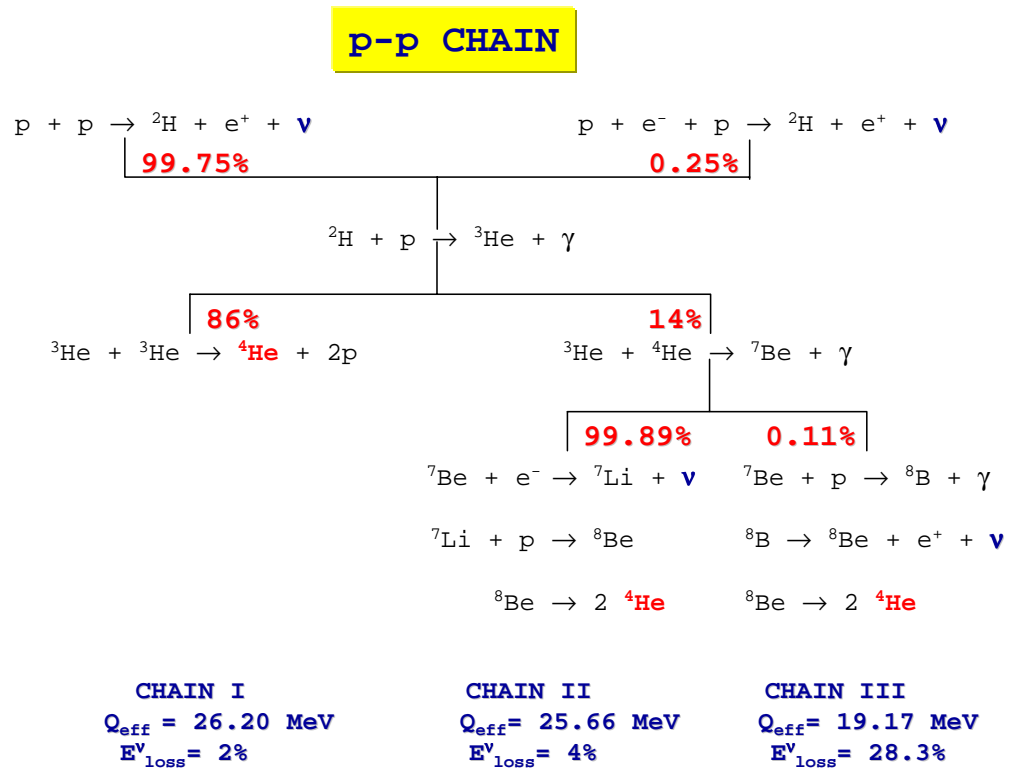
Figure 1.2: **The figure shows all the reactions of the p-p chain. The reactions are divided in the three chains which are the route followed to transform four protons in one helium nucleus.**
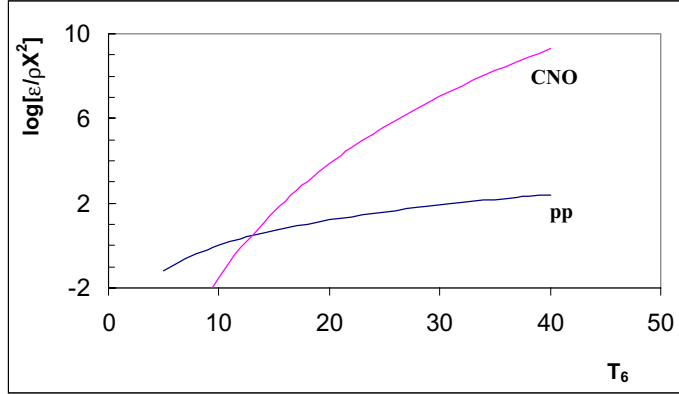
Figure 1.3: **Comparison between the energy produced in the p-p chain ($\epsilon_n = \rho X^2 T^4$) and CNO cycle ($\epsilon_n(CNO) = \rho X Z_{CNO} T^{18}$).**

of these sequences more closely.

When the center of the star reaches a temperature $\sim 6 \cdot 10^6 K$ the proton-proton reaction rate becomes significant; the deuterium so produced reacts with the proton sea giving ^3He, which, in turn, can react with the protons, ^3He and ^4He present in the environment. The proton capture has a very low cross section and it is neglected in the chain, but how we will see in chapter 3 this reaction produces a very high energy neutrino. The reaction $^3He +^3 He$, produces a helium nucleus and two protons (**chain I**); the $^3He +^4 He$ produces ^7Be, which is the first reaction of the second branch of the p-p chain. The ^7Be in unstable and it decays via electron capture in ^7Li and a neutrino of $0.38 MeV$ or $0.86 MeV$. It can also capture a proton, with a much smaller probability, producing ^8B, which decays in ^8Be producing a positron and a high energy neutrino($0\ MeV < E_\nu < 15\ MeV$), which is visible by Kamiokande. The ^8Be at once decays in two ^4He, ending the third chain of the p-p. Coming back to the second chain, the ^7Li captures a proton producing ^8Be which, as before, decays
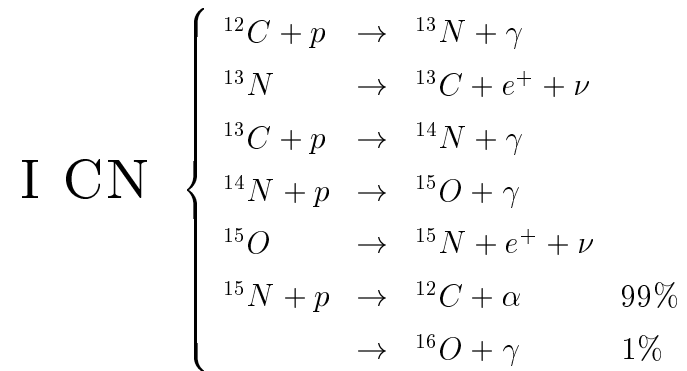
producing two helium nuclei.

The final result in all the three cases is the transformation of four protons in one helium nucleus, with the release of an amount of energy of $Q = 26.75 MeV$. Since, however, the energy lost via neutrino emission depends on the specific chain, we must consider three different Q values corresponding to a specific branch; in particular one has that:

- **pp I** $Q_{eff} = 26.2 MeV$;

- **pp II** $Q_{eff} = 25.66 MeV$;

- **pp III** $Q_{eff} = 19.17 MeV$.

A discussion of the solar neutrino fluxes related to the reaction $^7Be(p, \gamma)^8Be$ will be the subject of chapter 3.

As the central temperature increases the hydrogen burning via CNO cycle becomes more efficient. In fact when $T_C \sim 15 \cdot 10^6 K$ the carbon present in the star can react with the sea of protons, producing ^{13}N, which decays in ^{13}C which, in turn, captures another proton. As it is possible to see below at the end of this first part of the cycle four protons are transformed in one helium nucleus:

$$
\text{I CN} \begin{cases}
^{12}C + p & \to & ^{13}N + \gamma \\
^{13}N & \to & ^{13}C + e^+ + \nu \\
^{13}C + p & \to & ^{14}N + \gamma \\
^{14}N + p & \to & ^{15}O + \gamma \\
^{15}O & \to & ^{15}N + e^+ + \nu \\
^{15}N + p & \to & ^{12}C + \alpha & 99\% \\
& \to & ^{16}O + \gamma & 1\%
\end{cases}
$$

The sum of the starting abundance of carbon and nitrogen remains constant through the cycle. Since the $^{14}N(p, \gamma)^{15}O$ has the lowest cross section in this cycle at the end of the hydrogen burning almost all carbon is transformed in nitrogen. The time-scale of the cycle is lower than the p-p one and it is larger than million of years. When T_C
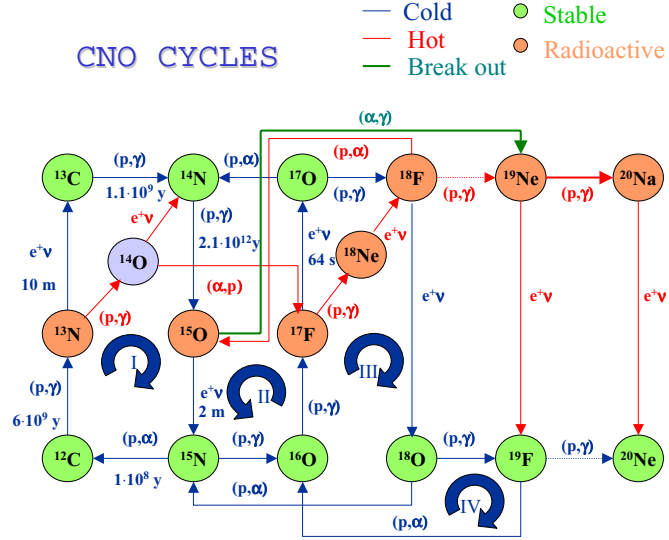
Figure 1.4: **Each reaction of the CNO cycles are shown with all the possible hot shotcuts (red line) and the breack out (green line).**

reaches $20 \cdot 10^6 K$ also the NO part of the cycle starts with the proton capture of the oxygen:

$$
\text{II NO} \quad
\begin{cases}
{}^{16}O + p & \to & {}^{17}F + \gamma \\
{}^{17}F & \to & {}^{17}O + e^+ + \nu \\
{}^{17}O + p & \to & {}^{14}N + \alpha \\
& \to & {}^{18}F + \gamma
\end{cases}
$$
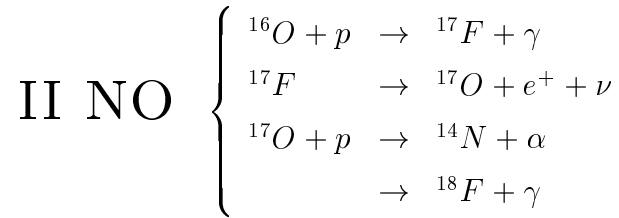
Two protons and one oxygen nucleus are transformed in one helium and nitrogen nuclei. The last two possible *cold* cycles are:

$$
\text{III} \quad
\begin{cases}
{}^{18}F & \to & {}^{18}O + e^+ + \nu \\
{}^{18}O + p & \to & {}^{15}N + \alpha \\
& \to & {}^{19}F + \gamma
\end{cases}
$$

$$
\text{IV} \quad
\begin{cases}
{}^{19}O + p & \to & {}^{16}O + \alpha \\
& \to & {}^{20}Ne + \gamma
\end{cases}
$$
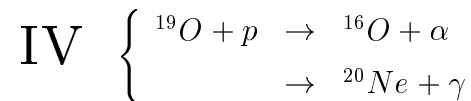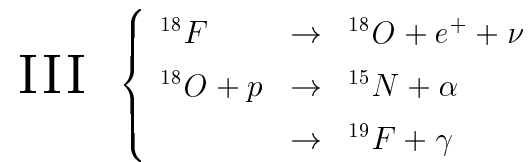
In figure 1.4 all the possible reactions are drawn considering also the possible hot shortcuts. Total result of the cycle is, as in the p-p chain, the transformation of four proton in one helium nucleus. It is important to underline that the cycle increases the initial abundance of nitrogen.

As already discussed, the energy rate of the CNO cycle increases with the temperature much more than that of the p-p chain: in fact the two relations are:

$$\epsilon_n(CNO) = \rho X Z_{CNO} T^{18} \tag{1.41}$$

$$\epsilon_n(p-p) = \rho X^2 T^4 \tag{1.42}$$

This means that when the central temperature exceeds $15 \cdot 10^6 K$ the hydrogen burning occurs via the CNO cycle (see fig. 1.3). The low mass stars, which burn hydrogen via the pp chain, have a thermal gradient not large enough to induce convective instability; therefore the core of those stars will be radiative. On the contrary stars which burn hydrogen via the CNO cycle form a convective core.

1.4.2 Helium burning

When T_C exceeds $10^8 K$ the fusion of two α particles can be followed by the capture of another α particle, before ^8Be decays. This is the first reaction of the helium burning and it can be interpreted as a three body reaction between 3α nuclei, because of the very short life time of ^8Be. The carbon produced by this reaction can capture another α particle forming an oxygen nucleus.

The $^{12}C(\alpha, \gamma)^{16}O$ is, together to the triple-α reaction, the most important process in the helium burning. In general, in the first part of helium burning, since the ^{12}C density is too low, the only active process is the triple-α reaction. In the last part of the helium burning the leading process is the $^{12}C(\alpha, \gamma)^{16}O$ reaction. The larger is the reaction rate of this reaction the larger is the helium burning time, because the Q value of the two processes is very similar but the $^{12}C(\alpha, \gamma)^{16}O$ consumes only one α particle instead of the 3 which are consumed by 3α reaction. The $^{12}C(\alpha, \gamma)^{16}O$ is

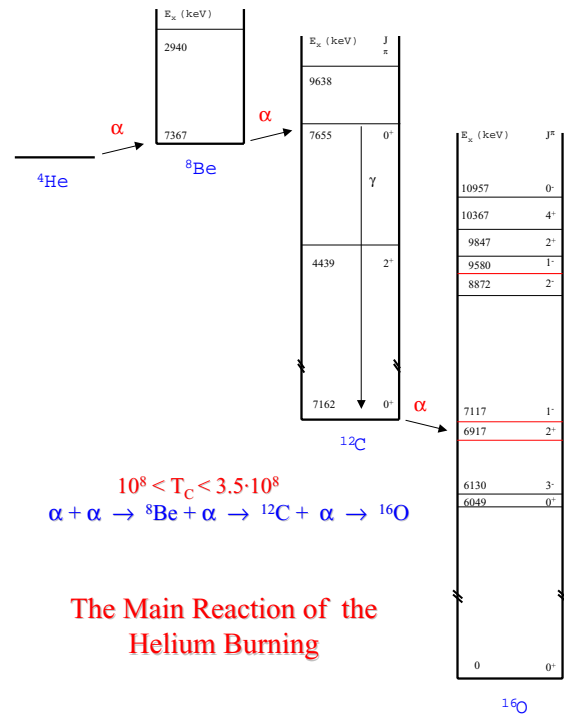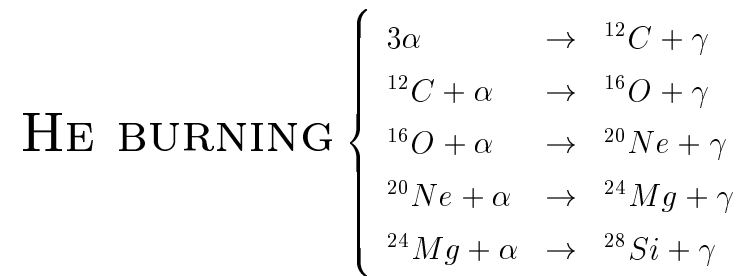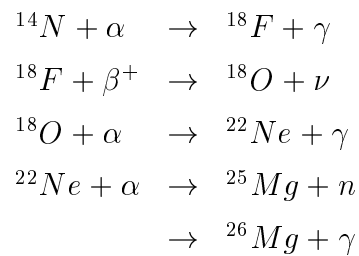Figure 1.5: **The main reaction of the Helium burning with the nuclear levels of the particles involved.**

a crucial reaction to understand the last stages of the stellar evolution (see chapter 4 and figure 1.5).

The complete set of reactions which take place during the helium burning are:

$$\text{HE BURNING} \begin{cases} 3\alpha & \rightarrow & {}^{12}C + \gamma \\ {}^{12}C + \alpha & \rightarrow & {}^{16}O + \gamma \\ {}^{16}O + \alpha & \rightarrow & {}^{20}Ne + \gamma \\ {}^{20}Ne + \alpha & \rightarrow & {}^{24}Mg + \gamma \\ {}^{24}Mg + \alpha & \rightarrow & {}^{28}Si + \gamma \end{cases}$$

In addition to this main channel the α capture by a ${}^{14}N$ is also possible, and a sequence of processes activate:

$$\begin{aligned} {}^{14}N + \alpha & \rightarrow & {}^{18}F + \gamma \\ {}^{18}F + \beta^+ & \rightarrow & {}^{18}O + \nu \\ {}^{18}O + \alpha & \rightarrow & {}^{22}Ne + \gamma \\ {}^{22}Ne + \alpha & \rightarrow & {}^{25}Mg + n \\ & \rightarrow & {}^{26}Mg + \gamma \end{aligned}$$
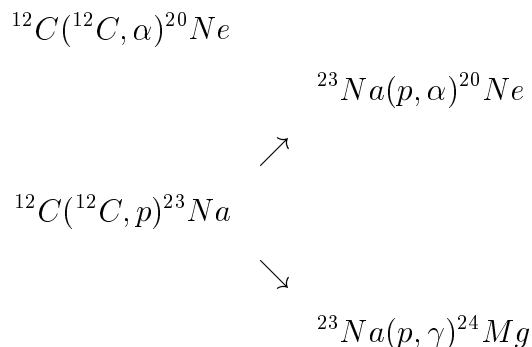
Note, by the way, that the process ${}^{22}Ne(\alpha, n){}^{25}Mg$ is one of the main producers of neutrons.

At the end of the core helium burning the chemical composition of the exhausted core will be dominated by the C and O in a ratio which depends on the ${}^{12}C(\alpha, \gamma){}^{16}O$ reaction rate plus a very small fraction of ${}^{20}Ne$, ${}^{24}Mg$ and ${}^{28}Si$.
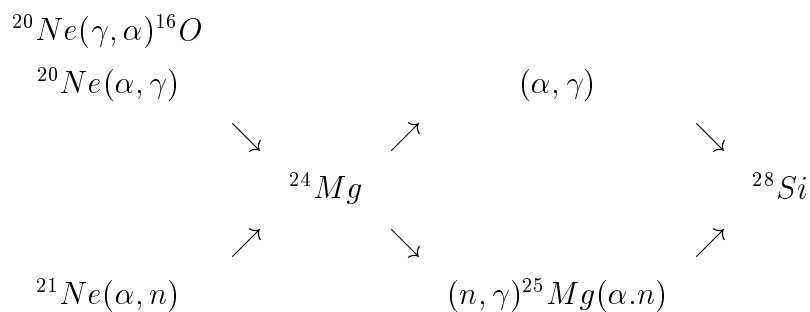
1.4.3   Advanced burning and the end of hydrostatic equilibrium

When the central temperature reaches $0.8 \cdot 10^9 K$ the central carbon burning takes place. The carbon burning main reactions are:

$$^{12}C(^{12}C, \alpha)^{20}Ne$$

$$^{23}Na(p, \alpha)^{20}Ne$$

$$\nearrow$$

$$^{12}C(^{12}C, p)^{23}Na$$

$$\searrow$$

$$^{23}Na(p, \gamma)^{24}Mg$$

At the end of the burning almost all of the carbon nuclei are transformed in ^{20}Ne, while only a small fraction of ^{24}Mg is produced. Note, however, that this fraction grows proportionally with the initial amount of ^{12}C.

Neon burning starts when T_C reaches about $1.2 \cdot 10^9 K$. The main reactions of neon burning are:

$$^{20}Ne(\gamma, \alpha)^{16}O$$
$$^{20}Ne(\alpha, \gamma) \qquad\qquad\qquad (\alpha, \gamma)$$
$$\searrow \qquad \nearrow \qquad\qquad\qquad \searrow$$
$$^{24}Mg \qquad\qquad\qquad\qquad ^{28}Si$$
$$\nearrow \qquad \searrow \qquad\qquad\qquad \nearrow$$
$$^{21}Ne(\alpha, n) \qquad\qquad (n, \gamma)^{25}Mg(\alpha.n)$$

At the end of this burning almost all the neon nuclei are transformed in oxygen with some amount of ^{24}Mg and ^{28}Si, which depends on the initial Ne abundance.

When the T_C raises above $2.5 \cdot 10^9 K$ the oxygen burning starts. All the oxygen is transformed in ^{28}Si, ^{30}Si, ^{32}S and ^{34}S and its duration is about one year.

The last quiescent burning involves the silicon and it begins when $T_C \sim 3.5 \cdot 10^9 K$. The typical time-scale of this burning is of the order of the months. This last burning

produces an iron core of almost $1.5M_\odot$. At this moment the star appears as an onion, where the various layers keep memory of the burnings occurred locally: moving from the center outward lighter and lighter elements are present starting from silicon up to the hydrogen. As we will see in the third chapter it is very important to understand how these layers are interconnected and how much the thickness and spatial location of the layers depend on the reaction rate of the $^{12}C(\alpha, \gamma)^{16}O$.

Once the central temperature exceeds 5 billion degrees, the idea of "real" processes which change the chemical composition of the matter becomes meaningless. The matter settles in a condition called Nuclear Statistical Equilibrium in which all the (strong) direct and reverse reactions are at the equilibrium. Since the changing of the NSE distribution with the temperature requires the absorbtion of energy, indeed of a release, a collapse of the core starts. This collapse ends when the matter reaches the nuclear density; at this stage a rebound occurs which leads to a shock wave moving outward. In a very small time (less the 1 s) almost $10^{53}erg$ of energy are produced:

- 99% of the energy is lost via neutrinos;

- 0.99% ($10^{51}erg$) is used to expel the envelope;

- "only" 0.01% ($10^{49}erg$) are shined on as visible photons.

Before closing this section we briefly schematize the kind of burnings which are experienced by the stars in the various mass ranges:

- if $M \leq 0.1M_\odot$ $\rightarrow$ the star is not able to ignite the hydrogen. The contraction stops when the interior of the star crystallizes (brown dwarfs and planets).

- If $0.1M_\odot \leq M \leq 0.5M_\odot$ $\rightarrow$ the star burns the hydrogen, but it can not ignite the helium (helium white dwarf).

- If $0.5M_\odot < M \leq 8M_\odot$ $\rightarrow$ the star burns the hydrogen and the helium and ends its life as a CO white dwarf.

- If $M > 8 M_\odot$ $\rightarrow$ the star can proceed through all the various burnings and eventually explode as a type II Supernova.

Chapter 2

The measurement of nuclear reaction rates

In the previous chapter we have described in detail the stellar evolution laws and we have shown the importance of the nuclear energy coefficient. It is one of the most important ingredients in the input physics to evolutionary models (section 1.2).

In this chapter we will remind briefly the basic laws which drive nuclear interactions in the stars (2.1, 2.2) and the basic measurement techniques (section 2.3). In the last section we will focus our attention on the Recoil Mass Separator method, which is the technique adopted for the measurement of the cross section of $^7Be(p,\gamma)^8B$ and $^{12}C(\alpha,\gamma)^{16}O$ reactions.

2.1 Nuclear energy coefficient

Nuclear reactions are the "engine" which supplies the stellar "machine"; therefore, the understanding of stellar evolution largely depends on our knowledge on nuclear reaction rates. If we consider the strong interaction between nuclides $(1+2 \rightarrow 3+4)$, then, using energy conservation, the energy consumed or produced by the reaction is:

$$Q_n = (M_{n,1} + M_{n,2} - M_{n,3} - M_{n,4})c^2 \tag{2.1}$$

where $M_{n,i}$ are the masses of the interacting particles. The main reactions in the stellar burnings, which involve particles lighter than iron, are esoenergetic ($Q > 0$). This occurrence allows stars to stop gravitational contraction, living in hydrostatic equilibrium and shining photons and neutrinos for such a long time.

To obtain the energy produced by nuclear reactions per second, the first step is to calculate the probability that a reaction takes place. This is proportional to the cross section σ. Considering N_X and N_Y particles per cubic centimeter of two differents species, which constitute the stellar gas, the reaction rate is (X = projectile and Y = target):

$$r = N_X N_Y v \sigma(v) \tag{2.2}$$

where $F = \sigma(v) N_Y$ is the effective cross section and $J = N_X v$ is the projectile flux.

In the stellar plasma the product between cross section and particle velocity has to be averaged over the probability $\phi(v)$:

$$< \sigma v >= \int_0^\infty \phi(v) v \sigma(v) dv \tag{2.3}$$

It follows that the reaction rate becomes:

$$r = N_X N_Y < \sigma v > (1 + \delta_{XY})^{-1} \tag{2.4}$$

where δ_{XY} is the Kronecker symbol.

Note that, deriving respect to the time N_X, we obtain the average life time of X interacting with Y:

$$\frac{dN_X}{dt}\bigg|_Y = -\frac{1}{\tau_Y(X)} N_X = -(1 + \delta_{XY}) r \ \Rightarrow \ \tau_Y(X) = \frac{1}{N_Y < \sigma v >} \tag{2.5}$$

In the majority of hydrostatic equilibrium phases the stellar plasma can be considered as a non degenerate and non relativistic gas (see section 1.2), therefore the velocity distribution follows the Maxwell-Boltzmann law:

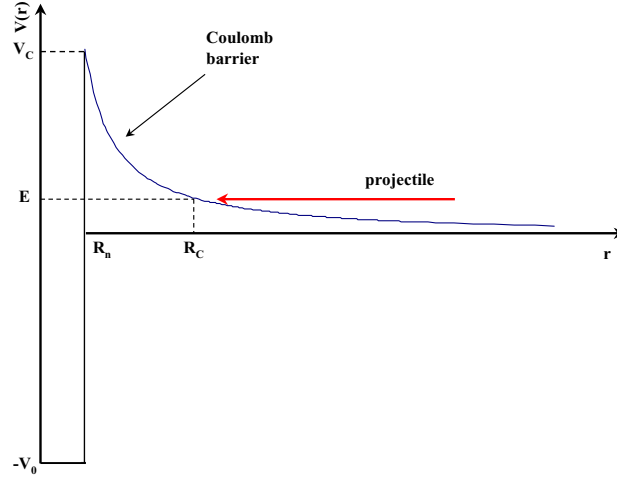$$\phi(v) = 4\pi v^2 \left(\frac{m}{2\pi kT}\right)^{3/2} \exp\left[-\frac{mv^2}{2kT}\right] \tag{2.6}$$

Figure 2.1: **Schematic rapresantation of the nuclear interaction.** R_C **is the Coulomb radius, i.e. the point starting on which the incident particle feels the Coulomb repulsion,** R_n **the nuclear radius and** V_C **the Coulomb potential.**

or:

$$\phi(E) \sim E \exp\left[-\frac{E}{kT}\right] \tag{2.7}$$

In the center of mass system, equation 2.3 becomes:

$$< \sigma v > = \left(\frac{8}{\pi\mu}\right)^{1/2} \frac{1}{(kT)^{3/2}} \int_0^\infty \sigma(E)E \exp\left[-\frac{E}{kT}\right] dE \tag{2.8}$$

where $\mu = m_X m_Y/(m_X + m_Y)$ is the reduced mass. With these assumptions we can re-write equation 2.4:

$$r = N_X N_Y \left(\left(\frac{8}{\pi\mu}\right)^{1/2} \frac{1}{(kT)^{3/2}} \int_0^\infty \sigma(E)E \exp\left[-\frac{E}{kT}\right] dE \right)(1 + \delta_{XY})^{-1} \tag{2.9}$$

Therefore the energy coefficient for reaction $1 + 2 \rightarrow 3 + 4$ is:

$$\epsilon_{nuc} = \epsilon_{12} + \epsilon_{34} = (r_{12} - r_{34})\frac{Q}{\rho} \tag{2.10}$$

2.2   The nuclear cross section in the stellar interior

In order to determine the temperature dependence of the reaction rate one has to know the cross section in the relevant energy range to evaluate the integral in equation 2.9. Due to the strong energy dependence of the penetrability of the Coulomb barrier, the astrophysical S factor is usually introduced by the following parameterization of the cross section:

$$\sigma(E) = \frac{1}{E} \exp[-2\pi\eta] S(E) \qquad (2.11)$$

in terms of the de Broglie wavelength ($\lambda^2 \propto 1/p^2 \propto 1/E$), the s-wave barrier penetration factor (in the approximation valid for $E << E_C$ [14]) and the slowly varying factor $S(E)$ which accounts for the nuclear properties of the process. In the above expression, η is the Sommerfeld parameter: $\eta = \frac{Z_1 Z_2 e^2}{h\nu}$. Substituting this expression for the cross section in equation 2.8, we have:

$$< \sigma v > = \left(\frac{8}{\pi\mu} \right)^{1/2} \frac{1}{(kT)^{3/2}} \int_0^\infty S(E) \exp\left[-\frac{E}{kT} - \frac{b}{E^{1/2}} \right] dE \qquad (2.12)$$

where $b = (2\pi)^{1/2} \pi e^2 Z_1 Z_2 / h$.

In those cases in which S(E) can be considered constant in the energy range in which the exponential in the integrand of equation 2.12 is significantly larger than zero, the latter shows a maximum (**Gamow peak**, see fig. 2.2) in:

$$E_0 = \left(bk\frac{T}{2} \right)^{2/3} = 1.22(Z_1^2 Z_2^2 \mu T_6^2)^{1/3} keV \qquad (2.13)$$

An estimate of the width of the Gamow peak can be obtained by $\Delta = \frac{4}{3^{1/2}}(E_0 kT)^{1/2}$.

The above treatment is valid when S(E) can be considered constant across the Gamow peak. A better approximation can be obtained performing a series expansion of the S(E) function around the energy axis origin (the Gamow peak is always lying at very low energies), involving not only the S(0) value, but also the first and, in some cases, the second derivative $S'(0)$ and $S''(0)$, obtained from fits to experimental data (see next section). In all cases the insertion of this expansion of S(E) in equation
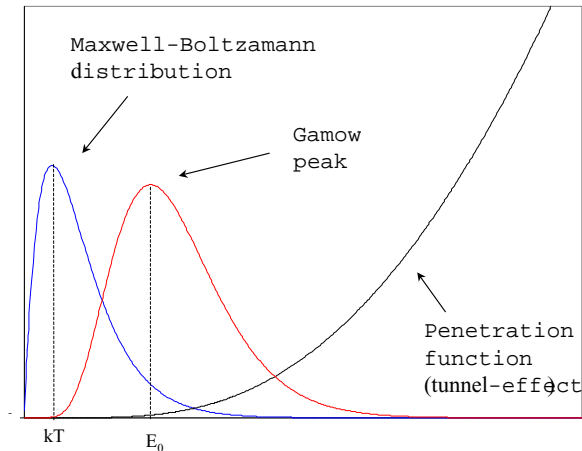
Figure 2.2: **The dominant energy-dependent functions are shown for nuclear reactions between charged particles. While both M-B distribution and tunneling function are small for the overlap region, the convolution of the two functions have a peak in E_0.**

2.12 and the approximation of the Gamow peak with a Gaussian function including a correction factor [89] leads to an analytic expression of the reaction rate of the kind:

$$< \sigma v >= AT^{-2/3}exp[-BT^{-1/3}] \sum_{i=1}^{5} \alpha_i T^{i/3} \qquad (2.14)$$

with the coefficients depending on $S(0)$, $S'(0)$ and $S''(0)$.

The quadratic approximation for $S(E)$ is valid in the non resonant case, i.e. when the contributions to the cross section arising from resonances in the compound nucleus in the relevant energy range are negligible. In this case, the cross section is dominated by direct reaction mechanisms. In the frequent case of radiative capture, i.e. the reaction in which the exit channel consists of a photon plus a residual nucleus, the direct capture is a process in which the electromagnetic interaction induces a transition of the target+projectile system in a state in the continuum to a final bound state with a well defined orbital angular momentum, accompanied by the emission of a γ-ray. The reaction proceeds without the formation of an intermediate (compound

nucleus) state, and the partial wave(s) involved, in the incident plane wave expansion, are selected by the selection rules of the relevant electric or magnetic multipole operators.

If, on the other hand, at the excitation energy of the compound system $E_x = E_{cm} + Q$ a virtual unbound state of the compound nucleus exists, the resonant excitation of this state in the entrance channel a and the subsequent decay in the exit channel b is described by the Breit-Wigner equation (see again [89]):

$$\sigma(E) = \pi\lambda^2 \frac{2J+1}{(2J_1+1)(2J_2+1)}(1+\delta_{12})\frac{\Gamma_a\Gamma_b}{(E-E_R)^2 + \left(\frac{\Gamma}{2}\right)^2} \qquad (2.15)$$

where J is the angular momentum of the compound nucleus, J_1 and J_2 those of the projectile and target, E_R is the resonance energy and Γ_a, Γ_b and Γ are the partial and total widths of the resonance. In the case of narrow resonances, i.e. when the total width is much smaller than the resonance energy, the integrand in equation 2.12 is dominated by the cross section term, and the other terms can be assumed to be a constant equal to the value assumed at $E = E_r$. Moreover, the energy dependence of total and partial widths can be neglected across the resonance, so that the reaction rate can be written as:

$$< \sigma v > = \left(\frac{2\pi}{\mu kT}\right)^{3/2}\hbar^2(\omega\gamma)_R exp\left[\frac{-E_R}{kT}\right] \qquad (2.16)$$

where ω is the statistical weight $\frac{2J+1}{(2J_1+1)(2J_2+1)}(1+\delta_{12})$ and γ, the strength of the resonance, is given by $\gamma = \frac{\Gamma_a\Gamma_b}{\Gamma}$. The exponential term indicates that at given stellar temperature the reaction rate is dominated by resonances with energy E_R close to kT.

Finally, the case of broad resonances, i.e. when the total width is comparable with the resonance energy, can be treated similarly to the non resonant case, with the difference that the S factor at the Gamow energy can be expressed in terms of the parameters of the resonance contributing with its tail to the cross section. It has to be noted that, in this case, more than one resonance in the vicinity of the Gamow energy, including subthreshold resonances (i.e. the tail of a bound state lying

slightly below the particle emission threshold), can contribute to the cross section, and interference terms between different amplitudes have to be taken into account. The reactions studied in the present work are characterized by the first and the last of the situations described above, respectively.

For the $^7Be(p, \gamma)^8B$ reaction from eq. 2.13 one obtains $E_0 = 18 keV$ for $T_6 = 15$. The Q-value of the reaction is $Q = 0.137\ MeV$, while ground state spins and parities of ^7Be and ^8B are $3/2^-$ and 2^+ respectively. No narrow resonances exist in the vicinity of $E = kT$, while the contribution of the 1^+ resonance at $E = 778\ keV$ ($E_R = 640\ keV$, $\Gamma = 36\ keV$) to the astrophysical energy region is negligible. The direct capture process is initiated by the $l = 0$ partial wave (with a small admixture of $l = 2$) with the emission of an $E1$ γ-ray directly to the $l_f = 1$ final state. The γ decay of the 1^+ resonance is a pure $M1$ transition which, as already noted, does not interfere with the low energy amplitude. As we will see in the following the presence of this resonance can give some effects (essentially for the elastic scattering cross section used for normalization) when measurements at high energy are performed in order to extrapolate to lower energies (see next section and figure 2.3).

Much more complicated is the situation for the $^{12}C(\alpha, \gamma)^{16}O$ reaction (Q-value= $7.15\ MeV$). Indeed, it has a large resonance ($\Gamma = 400\ keV$) at the energy $E_{cm} = 2.42\ MeV$ and spin and parity $J^\pi = 1^-$, which influences the reaction in the relevant stellar energy region and two sub-threshold resonances - $E = -45\ keV$, $J^\pi = 1^-$ and $E = -245\ keV$, $J^\pi = 2^+$ respectively -, which can enhance the stellar burning (see again figure 2.3) at the Gamow energy ($E_0 = 300\ keV$ at $T_9 = 0.2$). The first two resonances give rise to $E1$-decay to the 0^+ ground state of ^{16}O, while the decay of the 2^+ resonance and the direct capture process proceed via an electric quadrupole transition. For a detailed treatment of the energy behavior of such contributions to the reaction cross section we refer the reader to [46]. We want to stress here that for a complete description of the process one needs extensive measurement over a wide energy range (see below).
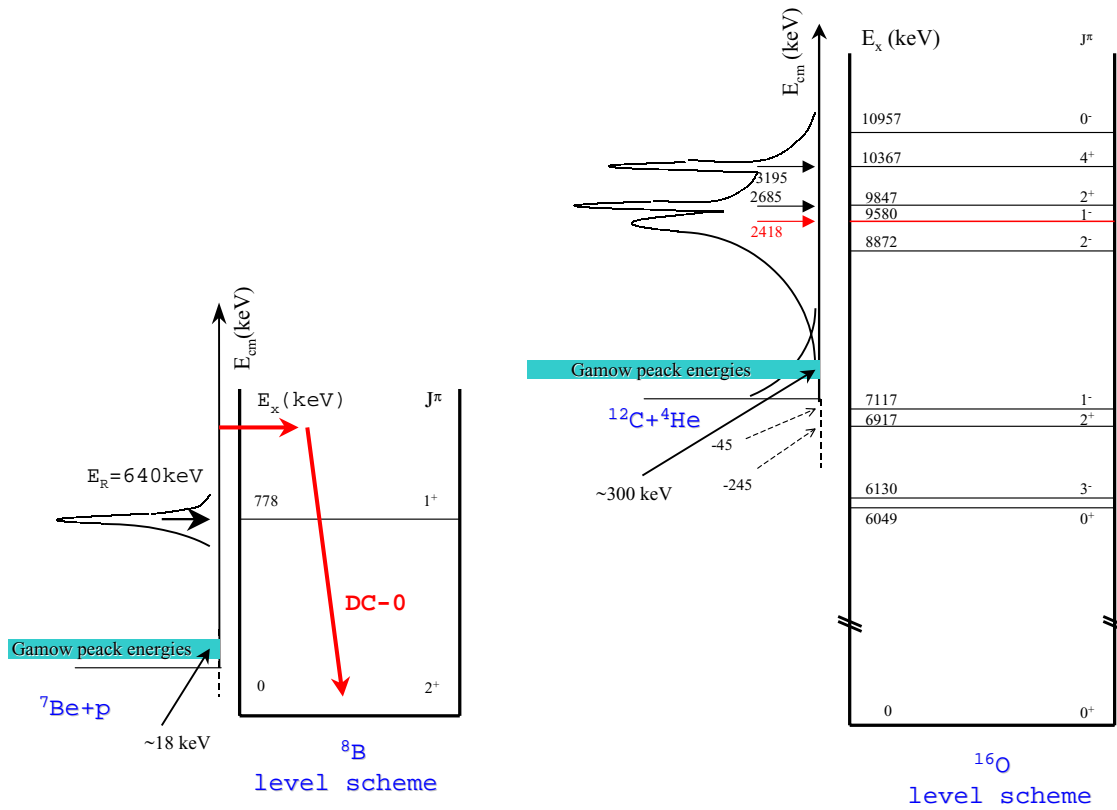
38

Figure 2.3: **Level scheme for ^{8}B and ^{16}O with the corresponding excitation function for ^{7}Be(p,γ)^{8}B and ^{12}C(α,γ)^{16}O reactions.**

2.3 The problem of the measurement at the astrophysical energies

As we have seen the Gamow energies for the astrophysical processes are very low. For the reaction of our interest, the expected cross sections at the respective Gamow energies are $\sigma(E = 18\ keV)_{^7Be(p,\gamma)^8B} = 1.1 \cdot 10^{-9}\ b$ and $\sigma(E = 300\ keV)_{^{12}C(\alpha,\gamma)^{16}O} = 2.5 \cdot 10^{-17}\ b$. This means that in realistic experimental conditions, the expected counting rate is prohibitively low. Even in those cases in which the event rate is compatible with human lifetime (i.e. in reactions between very light nuclei) the competition with cosmic background almost hampers to obtain statistically significant results. The only experiment which has been able to go down to Gamow peak is LUNA, exploiting the shielding of the almost $2\ km$ rock layer in the Gran Sasso National Laboratories [15] for the study of $^3He(^3He, 2p)^4He$ reaction.

As an alternative to the direct laboratory measurement of the $S(E_0)$ value, indirect methods can be used to reach information at the Gamow energy. With this it is usually meant measurements which can provide information about the process under study by the measurement of the nuclear properties which determine the desired cross section (such as resonance strengths, spectrospic factors, reduced widths) performed using different reactions which involve the same physical quantities. These are usually in a way model dependent, so that their applicability has to verified by comparison with direct methods, when applicable. Some of these are the Coulomb Break-Up, Direct Transfer, Trojan Horse or β-delayed α emission. The first method has been used to measure $^7Be(p, \gamma)^8B$ [61], and it consists in the study of the inverse reaction ($^8B(\gamma, p)^7Be$ photodisintegration). The inverse reaction cross section is related to the direct one by the detailed balance principle:

$$\sigma(^7Be(p, \gamma)^8B) = \frac{(2j_{^8B} + 1)}{(2j_{^7Be} + 1)(2j_p + 1)} \frac{k_{inv}^2}{k_{dir}^2} \sigma(^8B(\gamma, p)^7Be) \qquad (2.17)$$

where j are the spins, $k_{inv} = \frac{E_\gamma}{\hbar c}$ and $k_{dir} = \frac{2\mu E_{cm}}{\hbar^2}$. Since $k_{inv} << k_{dir}$, then photodisintegration cross section is larger than proton capture and so low energy regions are
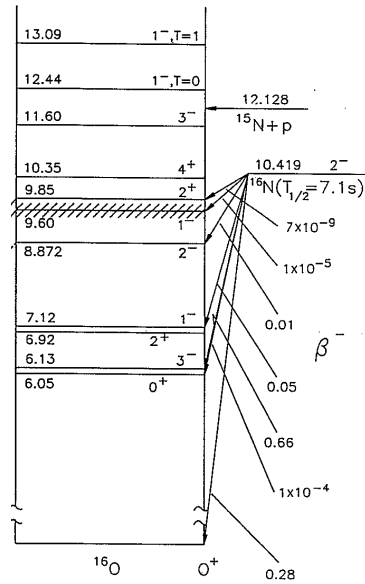
Figure 2.4: **Level scheme ^{16}O and main decays of ^{16}N which represents an indirect method to study the $E1$ component of the ^{12}C$(\alpha, \gamma)^{16}$O reaction.**

accessible to the measurement.

As γ-induced photodisintegration experiments are difficult to be performed, a virtual γ flux is produced by means of inelastic scattering of ^8B on a heavy nucleus, e.g. ^{208}Pb, and the reaction to study is:

$$^8B +^{208} Pb \rightarrow\ ^7Be + p +^{208} Pb_{gs} \tag{2.18}$$

The study of the β-delayed α spectrum from ^{16}N $(\tau_{1/2} = 7.13\ s)$ is another indirect measurement which can provide a constrain to the low energy E1 cross section of $^{12}C(\alpha, \gamma)^{16}O$. Indeed, the β-decay matrix element to the subthreshold 1^- state depends on the reduced width of the state. The α spectrum following decay can then be related to this observable. This represents a complementary route to the determination of the E1 cross section at low energy [6] (see fig. 2.4).

Coming back to direct measurements of the cross section of the reaction under study itself, owing to the impossibility of reaching the energy region of interest a

possible approach is to measure the cross section in a wide energetic window down to lowest accessible energy. After, one can extrapolate the data to astrophysical energies, once the nuclear parameters determining the energy dependence of the cross section have been obtained from a fit to experimental data. This procedure is in principle straightforward, also with the guidance of some theoretical considerations, but in many cases several complications may lead to considerable uncertainties. In the cases of our interest: an experiment aiming to the measurement of the $^7Be(p,\gamma)^8B$ cross section by bombardment of a ^7Be target with a proton beam and the detection of the reaction γ-ray, the ^7Be target radioactivity hampers the identification of reaction γ-rays. The existence of subthreshold resonances in $^{12}C(\alpha,\gamma)^{16}O$, the complicated interplay between different amplitudes and the strong background which may arise from the (α,n) reactions induced on ^{13}C impurities present in the ^{12}C target makes very uncertain the extrapolation to the Gamow energy.

To circumvent the above difficulties, the following approach has been adopted for the $^7Be(p,\gamma)^8B$ reaction. The ^8B, formed in the $^7Be + p$ reaction, has a life time $\tau = 0.8$ s. Then it decays, emitting a positron and a neutrino, in ^8Be, which in turn decays in two α particles (see figure 1.2). By means of these two sequential decays one can measure either the positron or α particles using a rotating ^7Be solid target, which moves alternately away from the beam line allowing the measure of the **delayed activity**. Usally the beryllium target is obtained by the reaction $^7Li(p,n)^7Be$, a further uncertainty in this method coming from the determination of the number density of ^7Be [95, 96]. In spite of these difficulties many experiments have been performed using this technique [64, 80, 65, 104, 108, 39, 50, 97] and the resulting data cover a wide range of energies. The possible presence of systematic uncertainties arising from the uncertain target stoichiometry and other effects will be discussed in the following chapter.

For $^{12}C + \alpha$ many experiments have been performed, based on the detection of γ-rays [37, 83, 84, 79, 66, 77, 78, 90, 46]. All these measurements extend to a minimum energy of about 1 MeV. The problem of ^{13}C contamination has been solved in some of

them using the inverse kinematics approach, i.e. the roles of the target and projectile have been inverted bombarding with a ^{12}C beam a gaseous ^{4}He target. In spite of this the $S(300\ keV)$ value is still known with a very large uncertainty [3].

In both cases the use of the inverse kinematics offers the possibility of reducing the systematic uncertainties and/or of extending the explored energy range. In particular it allows identification and counting of the recoil nuclei (e.g. ^{8}B and ^{12}C) which are formed in the reactions. Since they travel in the same direction of the beam, their direct detection, with high efficiency detectors, would greatly improve the experimental sensitivity. An obvious problem is the separation between beam and recoil nuclei. A useful technique is the Recoil Mass Separator method which has been used for the study of one of the reactions above mentioned and will be used for the other.

2.4 Measurement of nuclear reaction cross sections using the Recoil Mass Separator

In order to introduce the Recoil Mass Separator technique, let us assume that the radiative capture reaction $\mathbf{t}(\mathbf{b}, \gamma)\mathbf{r}$ is being studied in inverse kinematics. In this case $\mathbf{b}$ is a heavy ion (beam) and $\mathbf{t}$ a light particle, namely a $\mathbf{H}$ or $\mathbf{He}$ isotope (target). For given center of mass energy $\mathbf{E}$, the laboratory energy $\mathbf{E_b}$ of the beam will be higher than that needed to study the same reaction in direct kinematics (by the ratio $\mathbf{m_b/m_t}$). This means that the velocity of the center of mass and that of the recoiling nucleus $\mathbf{r}$, can be, even for $E < 1\ MeV$, large enough to allow the recoil to emerge from the target and to be identified. We will see in the following that many advantages can be obtained if a gas target is used. We assume then that a particle accelerator produces a beam impinging on a gas target and some magnetic and electrostatic elements are used downstream which are able to separate the two traveling beams (i.e. projectiles and recoils). Generally speaking, the beam direction has to be well defined by a set of collimators. If the gas target is rather thin the recoil nuclei do not have significant energy loss or straggling due to the interaction with target particles

and will emerge with a charge state distribution $\phi(q)$. If we assume (see the following) that recoils with charge state q^* are identified and detected with efficiency ε_r, their number can be related to the elastic scattering yield (N_{el}), measured concurrently.

Indeed, the number of the recoil particles is:

$$N_r = \Phi_q \varepsilon_r N_b N_t l^r_{eff} \sigma_r(E_{cm}) \tag{2.19}$$

where the quantity ϕ_q is the probability of the recoils to emerge from the gas target with the selected charge state, ε_r represents the transmission of the recoils through the separator, N_b and N_t are the number of beam and target particles, l^r_{eff} is the effective target length along the beam axis producing recoil nuclides and $\sigma_r(E_{cm})$ is the unknown cross section. If, during the same run, the elastic scattering yields N_{el} is measured by detection of scattering recoils, observed with particles detectors placed at an angle θ_{lab} in the gas target chamber, we have:

$$N_{el} = N_b N_t l^{el}_{eff} \Omega_{lab} \sigma_{cm}(\theta, E) \Omega_{cm}/\Omega_{lab} \tag{2.20}$$

where l^{el}_{eff} is the effective target length seen by the particle detector, $\sigma_{cm}(\theta, E)$ is the elastic scattering cross section at the associated center-of-mass angle θ, and Ω_{cm}/Ω_{lab} is the ratio of center-of-mass solid angle to laboratory solid angle. From the ratio of the above formulae, obviously, we obtain for the reaction cross section:

$$\sigma_r(E_{cm}) = \frac{N_r}{N_{el}} \frac{l^{el}_{eff} \Omega_{lab}(\Omega_{cm}/\Omega_{lab})}{(\Phi_q \ \varepsilon_r)} \ \sigma_{cm}(\theta, E_{cm}) \tag{2.21}$$

which allows a normalization of the unknown cross section avoiding the measurement of N_b and N_t. This ratio between the recoil and beam particles is extremely small: for $p(^7Be, \gamma)^8B$ reaction, considering a number of target particles of about $5 \cdot 10^{17} \ atoms/cm^3$, a gas target length of about $30 \ cm$ and a cross section $\sigma(E_{cm} = 1 \ MeV) = 0.5\mu \ b$, it values $\frac{N_r}{N_b} \simeq \mathbf{1 \cdot 10^{-12}}$ with $\varepsilon_r = 100\%$ and $\phi_{5+} = 65\%$. For $^{12}C(\alpha, \gamma)^{16}O$, considering a number of target particles of about $2 \cdot 10^{17} \ atoms/cm^3$, a cross section $\sigma(E_{cm} = 1 \ MeV) = 10 \ p \ b$, it values $\frac{N_r}{N_b} \simeq \mathbf{1 \cdot 10^{-18}}$. The identification of recoil particles cannot be performed in a detector by the identification of

their atomic number **z**. The detector would be "*killed*" by the huge rate associated with the beam. Rather, a dispersive analysis, based on a combination of magnetic and eletrostatic elements, has to be performed before the identification in the final detector. Note that the two beams have the same momentum and then, for equal charge state, the same magnetic rigidity $\mathbf{B}\rho = \sqrt{\mathbf{2mE}}/\mathbf{q}$.

Another experimental problem is due to the angle dispersion of the recoil beam. Indeed, since in the radiative capture part of the momentum $\vec{p_i}$ of the incident beam is transferred to the γ-rays ($\vec{p_\gamma} = E_\gamma/c$), then the recoil nuclei are emitted in a cone of half-angle $\theta/2 \simeq E_\gamma/p_i c$. The momentum of the recoil beam is on the average the same as the projectile with a spread, due to the γ emission, of:

$$\frac{\Delta p}{p} = \frac{E_\gamma}{(2m_i c^2 E_i)^2} \tag{2.22}$$

where m_i and E_i are the mass and energy of the incident beam. It is worth to note that the momentum spread is proportional to the Q-value of the reaction, since E_γ is proportional to Q-value. For $^7Be(p,\gamma)^8B$ ($Q = 0.137\ MeV$) and $^{12}C(\alpha,\gamma)^{16}O$ ($Q = 7.16\ MeV$) reactions, considering $E_{cm} = 1\ MeV$, the cone half angle and momentum spread are $\frac{\theta}{\mathbf{2}} = \mathbf{0.2}°$ and $\frac{\Delta\mathbf{p}}{\mathbf{p}} = \mathbf{0.7}$ % and $\frac{\theta}{\mathbf{2}} = \mathbf{1.5}°$ and $\frac{\Delta\mathbf{p}}{\mathbf{p}} = \mathbf{5}$ % respectively. It is fundamental that at the end of the gas target the exit collimators contain the cone of the recoil beam, in order to have a recoil transmission as close as possible to 100 %. A quadrupole lens should focus the divergent beam recoil nuclei to a narrow spot near the detectors. Obviously each magnetic and/or eletrostatic elements of the Recoil Mass Separator must have an angular and momentum acceptance larger than the dispersion of the reaction taken into account.

If to separate the recoil and incident beams we use a magnet placed between gas target and the detector (see upper diagram in fig. 2.5), then the separation power is due to the rigidity $R = p/q$, where p and q are momentum and charge state. Since the capture products have the same momentum of the beam, then the separation between intense incident beam and low recoil beam will be efficient only in the occurrence that recoil particles can have higher charge state than the maximum one allowed to the projectiles ($q_r > z_i$). This favourable condition is verified for the $p(^7Be,\gamma)^8B$ case,
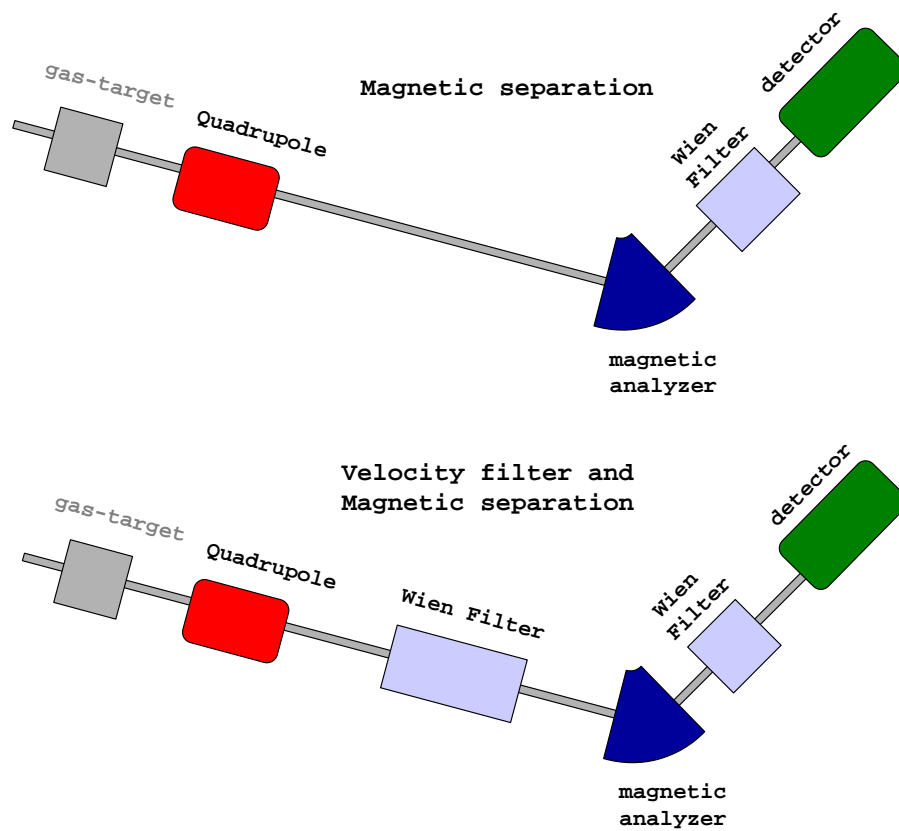
Figure 2.5: **Two possible waies to realize selection using the Recoil Mass Separator: the one (upper diagram) using only the rigidity selection induced by magnetic analizer, the second (lower diagram) peerforming also a velocity selection with a Wien Filter placed between gas target and magnetic analizer.**

since the well populated 5^+ charge state is not allowed to ^7Be ($z = 4$). As we will see in the next chapter this dispersive analysis is not sufficient to suppress the incident beam intensity to an acceptable level and a further selection, based on the velocities of the two beams, has to be performed.

In the case of $\alpha(^{12}C, \gamma)^{16}O$ reaction ^{16}O charge states between 7^+ and 8^+ have almost zero probability around $E_r = 3\ MeV$ ($E_{cm} = 1\ MeV$), therefore it is impossible to distinguish ^{16}O recoil particles from the ^{12}C projectiles (see fourth chapter). As an alternative technique, a Wien filter can be placed before the magnetic analyser (see lower diagram in fig. 2.5), which leaves undeflected all the particles of a given velocity v, independently of their charge state. The velocity of incident and recoil beams are different and the ratio is:

$$\frac{v_i}{v_r} = \frac{m_i + m_t}{m_i} \tag{2.23}$$

This feature allows to well separate recoil and incident beam, then the analysing magnet can unambiguously select one recoil beam charge state. Note that as the velocity resolution $\Delta v/v$ of the Wien filter decreases as the difference in mass between projectile and target particles decrease .

The specific features of the two reactions and the subsequent characteristcs of the design of the recoil separator for each of them will be discussed in the next two chapters.

Chapter 3

The $^7\text{Be}(\text{p}, \gamma)^8\text{B}$ reaction

The solar neutrino detection in the Homestake mine filled with chlorine [30, 31, 32] was one of the most important events for physics in this century. For the first time there was a direct evidence that sun shines because of nuclear fusion reactions, since neutrinos are produced in the center by solar nucleosynthesis and they escape from the surface "almost" not interacting with the environment.

Unfortunately the neutrino flux predicted by the solar model does not agree with the Homestake measurements: using solar neutrino units (SNU) [1] we expect about 8 SNU and the Homestake experiment measured only 2.56 ± 0.23 SNU. This discrepancy still persists today, in spite of three decades of data from Homestake and new results from Kamiokande [63], Super Kamiokande [100], SAGE [91] and GALLEX [43] experiments. In the next sections we will describe in detail the solar neutrino problem or, actually, the solar neutrino **problems**, and we will show that neither an astrophysical nor a nuclear solution are possible. This implies the need of a new neutrino physics, namely the so-called neutrino oscillations. We will see that, in the framework of the MSW theory, an important role is played by nuclear inputs to solar models: in particular the $^7Be(p, \gamma)^8B$ reaction rate strongly influences the high energy neutrino flux, so that an accurate determination of the cross section is highly desiderable. As the present knowledge of this cross section is possibly affected
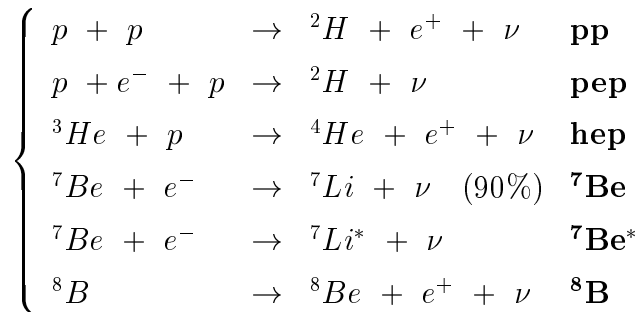
---

[1] $[1\ SNU \equiv 10^{-36}\ captures \cdot (target\,atom)^{-1} \cdot s^{-1}]$ see also next section.

by systematic uncertainties, a new direct measurement of the absolute cross section of the $^1H(^7Be, \gamma)^8B$ reaction using in inverse kinematics at $E_{cm} = 990 \ keV$ has been undertaken five years ago at the Naples TTT-3 accelerator.

3.1 The solar neutrino problem

The Sun (as mentioned before) is burning hydrogen mostly ($\simeq 85\%$) by means of the p-p chain: the reactions taking place during this phase have been shown in figure 1.2. Five of the reactions involved in this chain produce neutrinos:

$$
\left\{
\begin{array}{lll}
p \ + \ p & \rightarrow \ ^2H \ + \ e^+ \ + \ \nu & \textbf{pp} \\
p \ + e^- \ + \ p & \rightarrow \ ^2H \ + \ \nu & \textbf{pep} \\
^3He \ + \ p & \rightarrow \ ^4He \ + \ e^+ \ + \ \nu & \textbf{hep} \\
^7Be \ + \ e^- & \rightarrow \ ^7Li \ + \ \nu \ \ (90\%) & \textbf{^{7}Be} \\
^7Be \ + \ e^- & \rightarrow \ ^7Li^* \ + \ \nu & \textbf{^{7}Be}^* \\
^8B & \rightarrow \ ^8Be \ + \ e^+ \ + \ \nu & \textbf{^{8}B}
\end{array}
\right.
$$

In the center of the sun the CNO cycle is also partially active and so we have to add other three neutrinos coming from the ^{13}N, ^{15}O and ^{17}F decays. The flux and the energy distribution of ν's emitted from the Sun is of course dependent on the number of each of the above reactions taking place, and then on the details of the present state of the evolutionary path of the star (solar model). To estimate the expected neutrino flux we used the FRANEC code, considering element diffusion according to equation 1.39. Table 3.1 shows the comparison between the expected fluxes (for each solar neutrino) computed with FRANEC and those calculated by Bahcall and Pinsonneault 1998 [7]. Using our value for the flux we calculate the spectrum assuming the standard electroweak theory [82] (see figure 3.1).

Solar neutrino experiments measure the flux using radiochemical or water Cherenkov detectors. Homestake [32], SAGE [91] and GALLEX [43] belong to the first group: they used chlorine and gallium detectors exploiting the reactions:
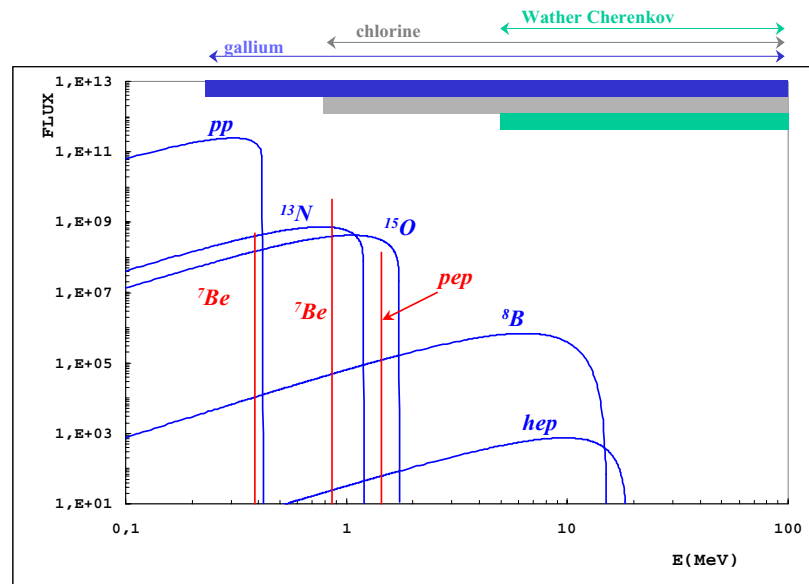
Figure 3.1: **The Solar Neutrino Spectrum is shown in the figure. The neutrino fluxes for continuum sources are given in the units of number per cm^2 per second per MeV at one astronomical unit; while line fluxes are given in number per cm^2 per second. The coloured lines on the top of the figure indicate the energy thresholds for the ongoing neutrino experiments.**

Table 3.1: **Solar neutrino flux expected on earth calculated by means of the FRANEC code for the 9 solar nuclear reactions which produce a neutrino in** $cm^{-2}s^{-1}$. **The second column reports the energy range for continuum source and the energy for line source of the neutrino, while in the fourth column we report for comaprison the calculated values by Bahcall [7].**

		E_ν $[MeV]$	Flux at earth $[cm^{-2}s^{-1}]$	
			FRANEC	BP98
pp	$0 \rightarrow$	0.42	$6.03 \cdot 10^{10}$	$5.94 \cdot 10^{10}$
pep		14	$1.43 \cdot 10^{8}$	$1.39 \cdot 10^{8}$
hep	$0 \rightarrow$	18.7	$7.68 \cdot 10^{3}$	$2.10 \cdot 10^{3}$
^{7}**Be**		0.86	$4.46 \cdot 10^{9}$	$4.32 \cdot 10^{9}$
^{7}**Be***		0.38	$4.96 \cdot 10^{8}$	$4.80 \cdot 10^{8}$
^{8}**B**	$0 \rightarrow$	15	$5.18 \cdot 10^{6}$	$5.15 \cdot 10^{6}$
^{13}**N**	$0 \rightarrow$	1.2	$5.34 \cdot 10^{8}$	$6.05 \cdot 10^{8}$
^{15}**O**	$0 \rightarrow$	1.7	$4.52 \cdot 10^{8}$	$5.32 \cdot 10^{8}$
^{17}**F**	$0 \rightarrow$	1.7	$5.53 \cdot 10^{6}$	$6.33 \cdot 10^{6}$

- **Homestake** $\Rightarrow$ $\nu_e + \,^{37}Cl \rightarrow \,^{37}Ar + e$

  which has an energy threshold at 0.814 MeV;

- **SAGE and GALLEX** $\Rightarrow$ $\nu_e + \,^{71}Ga \rightarrow \,^{71}Ge + e$

  which has an energy threshold at 0.233 MeV.

Super Kamiokande [100] is a water Cherenkov experiment and solar neutrinos are detected by virtue of their elastic scattering on the electrons bound in the water molecules ($\nu + e \rightarrow e + \nu$) and it is able to measure the energy spectrum with an energy threshold of about $6 MeV$. Therefore this experiment measures almost only the neutrinos coming from ^{8}B decay. The expected flux at the earth surface, considering the energy range from 0 to 15 MeV, is $5.18 \cdot 10^{6}$ cm^{-2} s^{-1} (while BP98 estimates $5.15 \cdot 10^{6}$ cm^{-2} s^{-1}) and the measured value (taking into account the extrapolation from the threshold energy down to zero energy) is $2.44^{+0.09}_{-0.07} \cdot 10^{6}$ cm^{-2} s^{-1}.

Table 3.2: **Flux expected for reaction in each experiment. The values are given in SNU for chlorine and gallium experiments, while that for Kamiokande is given in $10^6\ cm^{-2}\ s^{-1}$. The last line reports the expected totals and the flux measured.**

	Cl [SNU]		Homestake [SNU]	Ga [SNU]		SAGE [SNU]	GALLEX [SNU]	H₂O [$10^6\ cm^{-2}\ s^{-1}$]		SuperKam [$10^6\ cm^{-2}\ s^{-1}$]
	FRA	BP98		FRA	BP98			FRA	BP98	
pp	0.0	0.0		72.1	69.6			0.0	0.0	
pep	0.2	0.2		3.0	2.8			0.0	0.0	
hep	0.0	0.0		0.1	0.0			$7.68 \cdot 10^{-3}$	$2.10 \cdot 10^{-3}$	
^{7}Be	1.1	1.15		33.8	34.4			0.0	0.0	
^{7}Be*	0.0	0.0		1.1	.....			0.0	0.0	
^{8}B	5.9	5.9		12.3	12.4			5.18	5.15	
^{13}N	0.3	0.1		3.2	3.7			0.0	0.0	
^{15}O	0.2	0.4		5.1	6.0			0.0	0.0	
Tot.	7.8	7.7	2.56 ± 0.23	130.6	129	77^{+8}_{-7}	66^{+7}_{-8}	5.18	5.15	$2.44^{+0.09}_{-0.07}$

In table 3.2 we show the comparison between the predicted values and the measured ones by the four experiments. The predicted values for radiochemical experiments result from a folding of the calculated neutrino spectra with the cross sections of the relevant detection process, i.e. from experimental details (volume of the tank and cross sections) one can calculate the number of captures expected for each experiment:

$$N_C = \int \frac{dN}{dEdSdt} \sigma(E) nlSdE \qquad (3.1)$$

where S is the surface and l the height of the tank and n is the number of atoms per unit volume. From the above equation the Solar Neutrino Unit is defined:

$$1 \ SNU = \frac{N_C}{N_{atm}} = \int \frac{dN}{dEdSdt} \sigma(E) dE \qquad (3.2)$$

where N_{atm} is the number of target atoms in the experimental tank.

SAGE and GALLEX experiments are sensitive to almost all the solar neutrino energy window, then they should measure almost all the flux expected. They measure **only** $75^{+8}_{-7} \ SNU$ and $74^{+7}_{-8} \ SNU$, instead of the 130.6 SNU expected: this is usually called **the missing neutrino** problem.

Analysing the information coming from the three regions explored by the experiments, on can see that there is not only a problem of "missing neutrino". Indeed independently from the actual strength of the ^8B neutrino source, from the measurement of part of the spectrum (water experiment) one can calculate the expected flux in any other energy window. Then folding the latter with the detection process cross section the expected measurement for the other experiments can be estimated. Using this kind of mutual re normalization of the different experiments, one could halve the flux expected from ^8B, reconciling it with Super Kamiokande measurement, which gives a direct information about ^8B neutrinos. Doing so we have no "room" for ^7Be neutrinos: in fact, the neutrino flux in the Homstake energy window, is, still, overpowered by the ^8B neutrino flux ($\sim 3SNU$) [9]. The incompatibility of the chlorine and the Kamiokande experiment is the so called **^{7}Be/^{8}B anomaly**. To solve this

problem one needs a new neutrino physics including not standard electroweak theory, which changes the shape of ^8B neutrino spectrum.

The irreconcilability between the expected ^7Be neutrino flux and measurements remains considering also the GALLEX and SAGE, since the number of neutrinos detected ($\sim 75\ SNU$) is too small. In fact, in the gallium unit, we should expect 73 SNU from pp neutrino and 7 SNU from ^8B - normalizing the value to Superkamiokande measurement -. There is again no room for the 34 SNU expected from beryllium (this is the so called **missing ^{7}Be neutrino**).

It is worth to stress that the above discrepancy is independent on any assumptions on the solar model (see next paragraph) or on nuclear inputs. It is only based on the shape of the ^8B neutrino spectrum, which is in turn dependent only on the electroweak theory.

3.1.1   Uncertainty in the Standar Solar Model

We perform solar model calculations using FRANEC code with the prescription shown in the first chapter and taking into account element diffusion [94]. To reproduce the sun we evolve a model trying to fit the two experimental data. We have for the sun: luminosity ($L_\odot = 3.85 \cdot 10^{33} erg\ s^{-1}$) and radius ($R_\odot = 6.96 \cdot 10^{10}\ cm$). Helioseismology data helps us to verify the goodness of the model, since we have independent observational measurements for the helium surface abundance (Y_S) and for the depth of surface convection (R_{CS}). Our data for helium is $Y_S = 0.251$ and for convection $R_{CS} = 0.710\ R_\odot$ which are in good agreement with helioseismology data $Y_S = 0.249 \pm 0.003$ [11] and $R_{CS} = 0.713 \pm 0.001\ R_\odot$ [12]. We remind that values obtained by Bahcall and Pinsonneault in 1998 [7] are: $Y_S = 0.243$ and $R_{CS} = 0.714\ R_\odot$.

The element diffusion provides a larger temperature and density in the interior of the sun [8] and therefore a smaller central hydrogen abundance for solar model: our value is $X_C = 0.3343$, the one in [8] is $X_C = 0.3333$, while without diffusion it is $X_C = 0.3613$. The other consequence of higher temperature and density is the

increasing of expected neutrino flux. Predictions without diffusion gave for gallium experiment 126 SNU, for chlorine 7 SNU and for ^8B neutrino $4.9 \cdot 10^6 \ cm^{-2} \ s^{-1}$ [8].

A possible source of uncertainty in standard solar models (SSM) is the opacity, since we do not know with sufficient precision the solar chemical composition and, in particular, the central metal content. Quantavely an opacity reduction of 10% means a reduction of T_c of 1%, which has not a one-to-one correspondence with the neutrino flux since it is not possible to adjust T_c leaving all the rest unchanged. The dependence of the most important neutrino flux on T_c is:

$$
\begin{cases}
\mathbf{pp} & \propto \quad T_C^{-1/2} \\
\mathbf{^7Be} & \propto \quad T_C^{8} \\
\mathbf{^8B} & \propto \quad T_C^{18}
\end{cases}
$$

The important conclusion is that a 1% uncertainty in T_c means almost 20% uncertainty in boron flux which confirms the impossibility to solve $^7Be/^8B$ anomaly by using astrophysical arguments. Again helioseismology help us: in fact the comparison between sound speeds in the sun from helioseismological measurements and model is in good agreement using the OPAL [57, 2] value for opacity.

The nuclear reaction rate is another source of uncertainty, since no reaction, with the exception of the $^3He(^3He, 2p)^4He$ [15], is explored down to the Gamow energy and since the $p + p$ reaction rate has only a theoretical estimate. We use, as we said in section 1.3, for nuclear reaction rate data the 1988 Fowler compilation, and for $^7Be(p, \gamma)^8B$ value the compilation of NACRE. In spite of that, the missing ^7Be neutrino problem can not be explained by uncertainties on the value of beryllium electron capture rate, since the ^8B neutrinos, observed in Superkamiokande experiment, are produced in competition with the undetected ^7Be neutrino. Reducing the reaction rate of production of ^7Be, to reconcile ^7Be flux with observation, reduces accoringly the boron neutrino flux. Moreover, the beryllium neutrino flux is independent of measurement uncertainties in the cross section of $^7Be(p, \gamma)^8B$ reaction, which is the most uncertain nuclear quantity in SSM, because the electron capture probability is

much larger than proton capture [2]. Therefore one should increase the reaction rate of proton capture of a factor larger than 100 to affect the calculated beryllium neutrino flux. Unfortunately, this makes the boron neutrino prediction completely inconsistent with Superkamiokande experiment.

The solution of solar neutrino problem is not in the uncertainty of SSM. Moreover the possibility of existence of Non-Standard Solar Model seems to be ruled out by the good agreement between SSM and helioseismological data. We need physics beyond the standard electroweak model to change the neutrino energy spectrum after the neutrinos are produced in the center of the sun.

3.1.2   Neutrino oscillations: a possible solution

The standard electroweak model requires massless neutrino. Nevertheless, admitting the possibility that neutrino would have masses no fundamental symmetry would be violated. Pontecorvo [81] first suggested to test the hypothesis of massive neutrino by means of the solar neutrino. The basic idea is that massive neutrino ν_e produced in the center of the sun could be transformed into $\overline{\nu}_e$ or into other neutrino flavors (ν_μ, ν_{tau}) and consequently the measurable flux on the earth would be depleted.

If we consider only two oscillating flavors, the mass eigenstates $\mid \nu_1 >$ and $\mid \nu_2 >$ are related to the weak interaction eigenstates by [82]:

$$\mid \nu_e >= \cos\theta_v \mid \nu_1 > + \sin\theta_v \mid \nu_2 >$$

$$\mid \nu_\mu >= -\sin\theta_v \mid \nu_1 > + \cos\theta_v \mid \nu_2 > \tag{3.3}$$

where θ_v is the mixing angle. For the case of vacuum oscillation the survival probability for a distance x is:

$$P^{ext} = 1 - \sin^2 2\theta_v \sin^2\left(\frac{\delta m^2 x}{4E_\nu}\right) \tag{3.4}$$

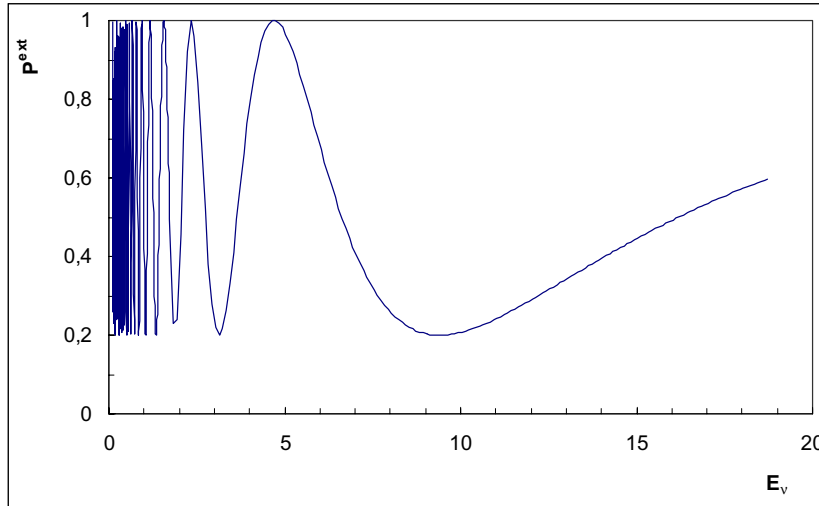
[2]Using standard parameters almost 1000 times larger.

Figure 3.2: **Survival probability for the vacuum oscillation solution.**

where E_ν is the neutrino energy and $\delta m^2 = m_2^2 - m_1^2$. From the last equation we define the oscillation length:

$$L_0 = \frac{4\pi E_\nu}{\delta m^2} \qquad (3.5)$$

Since the average distance x between Sun and Earth is $1\ AU = 1.496 \cdot 10^{13}\ cm$, to achieve correct prediction of measured neutrino flux we need a large mixing angle and a very small δm^2. The obtained in our calculation are:

$\mathbf{sin^2 2\theta = 0.910^{+0.020}_{-0.025}}$, which means $\theta \sim \mathbf{72°}$ and $\mathbf{\delta m^2 = (2.80 \pm 0.1) \cdot 10^{-10}\ eV^2}$. The fit with this values gives a $\mathbf{\chi^2 = 0.70}$. In figures 3.2 and 3.3 we report the survival probability and neutrino spectra. The oscillation provides ^7Be missing neutrino and a raising survival probability for large E_ν.

The understanding of solar neutrino problem changed radically when Mikheyev and Smirnov [72, 73] showed that the density dependence of the neutrino effective mass can provide a solution even for small mixing angle because of medium-induced
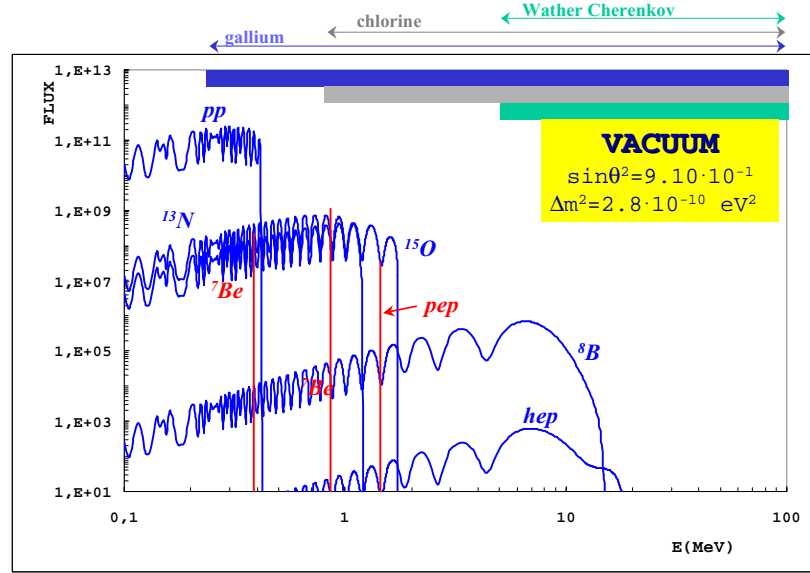
Figure 3.3: **Solar Energy Spectrum considering the vacuum solution.**

resonant oscillations: this is the so called **MSW** effect.

Solving the oscillation eigenstate equations taking into account sun density ($\rho(r)$) [72, 73, 51], we find for:

$$\gamma_c = \frac{\sin^2 2\theta_f}{\cos 2\theta_f} \frac{\delta m^2}{2E} \frac{1}{\mid \frac{1}{\rho_c} \frac{d\rho(r)}{dr} \mid_{r=r_c} \mid} >> 1 \tag{3.6}$$

a survival probability of:

$$P^{ext} = \frac{1}{2} + \frac{1}{2} \cos 2\theta_f \cos 2\theta_i (1 - 2P_{hop}) \tag{3.7}$$

where θ_i is the mixing angle at the production point, θ_f is the mixing angle at the detection point and P_{hop} is the *hopping probability* which, considering an exponential profile for density in the sun ($\rho(r) = \rho_c \cdot e^{-k \cdot \frac{r}{R_S}}$), is:

$$P_{hop}^{exp} = \frac{e^{-(\pi\gamma_c/2)(1-\tan^2\theta_f)} - e^{-(\pi\gamma_c/2)(1-\tan^2\theta_f)/\sin\theta_f}}{1 - e^{-(\pi\gamma_c/2)(1-\tan^2\theta_f)/\sin\theta_f}} \tag{3.8}$$
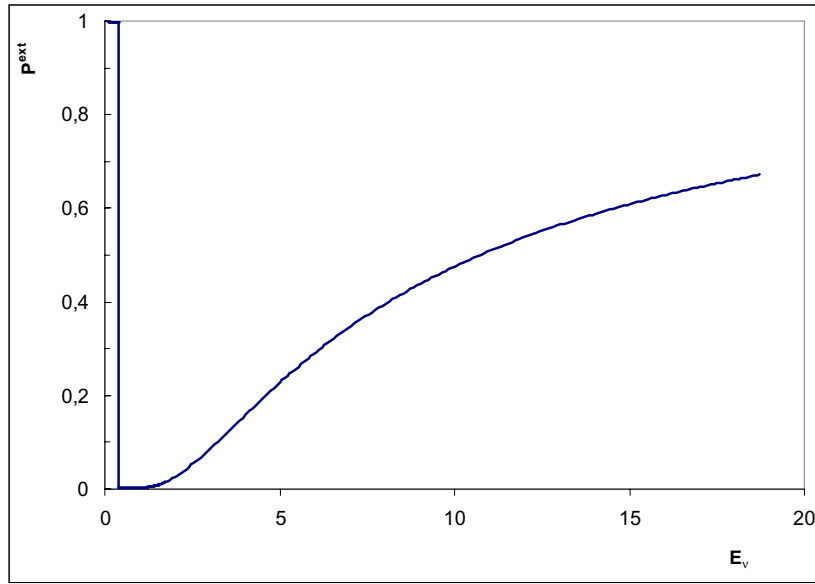
Figure 3.4: **Survival probability for the small angle solution in the MSW framework.**

Using the starting and measurement values for neutrino flux seen in the previous sections and the solar density profile calculated with FRANEC ($k = 8.81$), we find a large and a small mixing angle solution (see figures 3.6, 3.7, 3.4 and 3.5). For large mixing angle we have $sin^2 2\theta = 0.977$ and $\delta m^2 = (5.11 \cdot 10^{-5} \ eV^2$ with a $\chi^2 = 13$. The small angle solution gives a better fit with $\chi^2 = \mathbf{1.33}$. The values of $sin^2 2\theta$ and δm^2 for small mixing solution are:

$\mathbf{sin^2 2\theta = (6.69^{+0.36}_{-0.34}) \cdot 10^{-3}}$, which means $\theta \sim \mathbf{5^\circ}$ and $\mathbf{\delta m^2 = (3.54 \pm 0.12) \cdot 10^{-6} \ eV^2}$.

As we see in figure 3.4 the survival probability in the small mixing angle picture is almost 100% in the range of **pp** flux energy, after it falls to zero in the range of beryllium flux, raising again for energy larger than 2 Mev. This shape reconciles measurements and theory. In the case of large mixing, the shape (figure 3.6) is essentially a step which provides a larger probability for lower energy. One should note
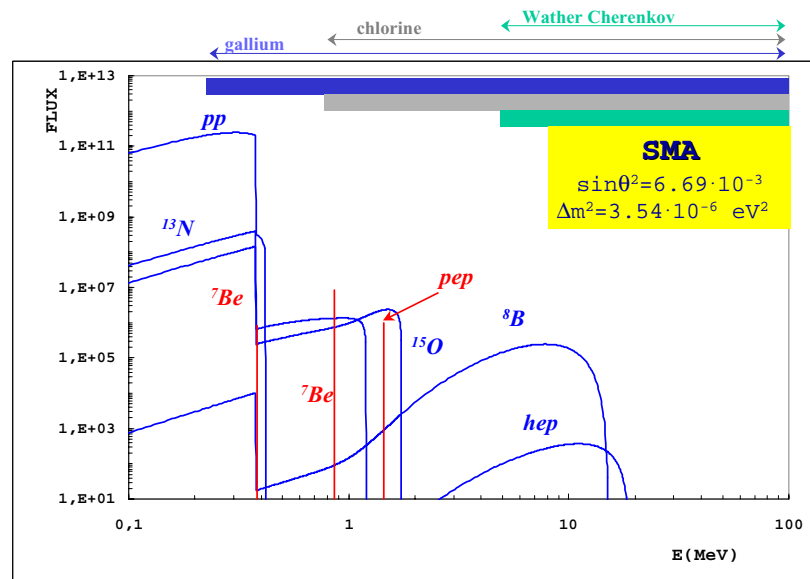
Figure 3.5: **Solar Energy Spectrum considering the small angle solution in the MSW framework.**
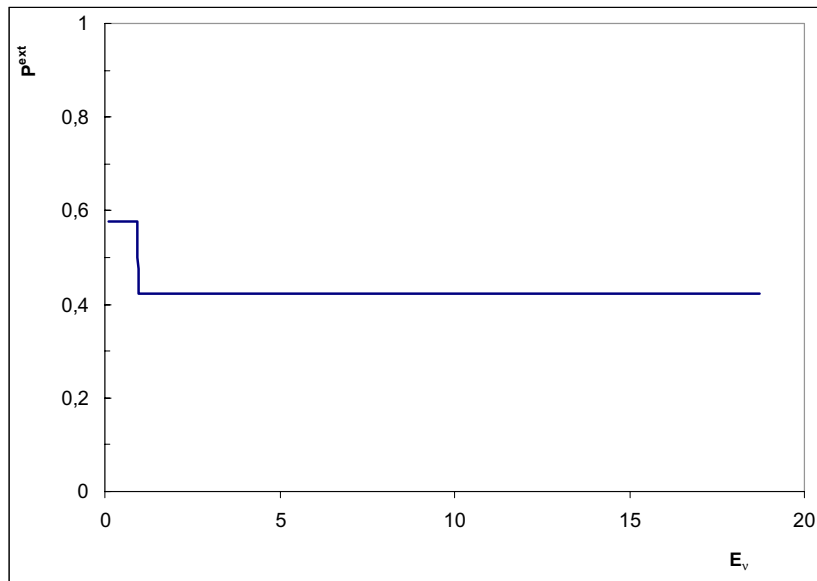
Figure 3.6: **Survival probability for the large angle solution in the MSW framework.**
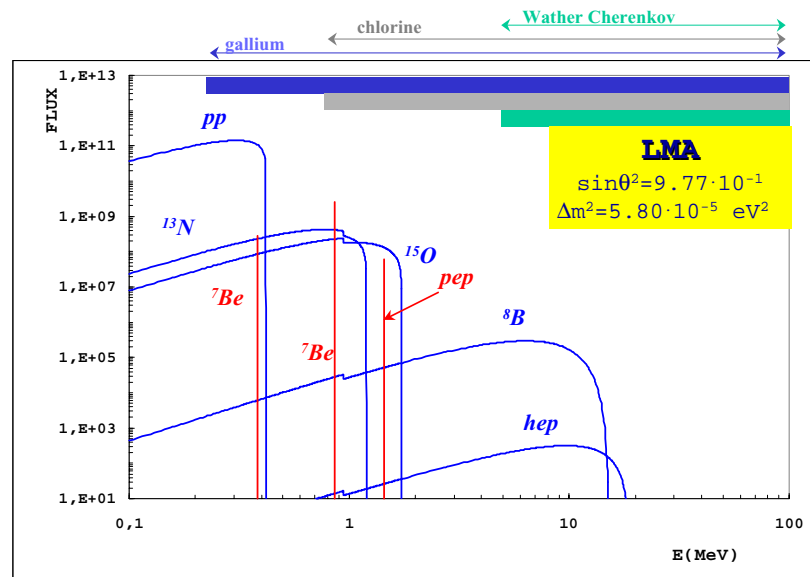
Figure 3.7: **Solar Energy Spectrum considering the large angle solution in the MSW framework.**

that the above values have been obtained using the compilation value $S_{17} = 21\ eV\ b$ for the astrophysical S factor at zero energy of the ${}^7Be(p,\gamma){}^8B$ reaction. We will see at the end of this chapter the changes in the fitting parameters due to a new determination of $S_{17}(0)$.

3.2 Direct measurement of the absolute cross section of $p({}^7Be,\gamma){}^8B$

Many authors in the last forty years have been involved in measuring the ${}^7Be(p,\gamma){}^8B$ reaction rate. Most of them have used the direct kinematic approach, using a proton beam and a beryllium target. The reaction proceeds at energy far from the resonance at $E_R = 640\ keV$ $(J^\pi = 1^+, \Gamma = 36\ keV)$ via the direct capture (DC) mechanism. Since ${}^7Be$ target emits an intense γ-ray flux of 478 keV energy $(T_{1/2} = 53\ d)$, the direct measurement of DC γ-rays is hampered. The process has, therefore, been studied indirectly by observing either the delayed positron or the delayed α-particles emitted in the decay of the produced ${}^8B$ nuclei, by means of a rotating target, which wavers between beam line and detectors.

The present knowledge of the cross section is based essentially on measurements with this technique performed using radioactive ${}^7Be$ targets produced by hot chemistry [64, 80, 65, 104, 108, 39, 50]. Other available data result from experiments with the inverse process, i.e. ${}^8B$ coulomb dissociation [61] (see section 2.3).

The measurements provided $\sigma(E)$ data covering a wide center-of-mass energy range (see figure 3.9), which show, however, a considerable scatter and, so, it is problematic to combine the results in a sort of "world average" [62]. The main uncertainty lies in discrepancies on absolute values larger then the quoted errors. The ${}^7Li(d,p){}^8Li$ cross section [95, 96] is commonly used to normalize data [3]. In 1998 Weissman et al. [106] suggested - on the basis of TRIM [93] simulations - that a significant backscattering of the recoiling ${}^8B$ nuclides out of the target could occur affecting significantly the deduced cross section values: a loss of up to 15% was predicted depending on
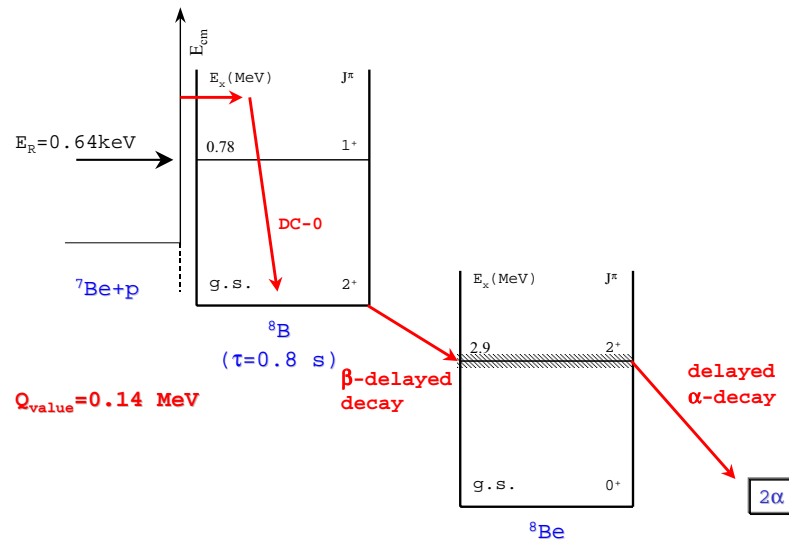
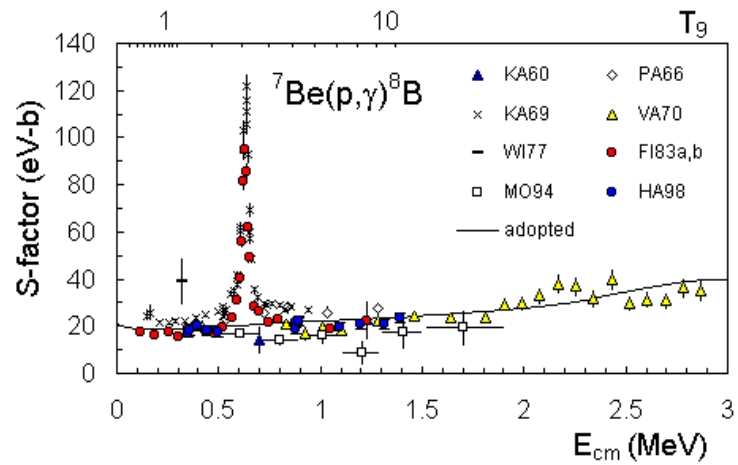Figure 3.8: **Schematic rapresentation of ^{7}Be(p, γ)^{8}B and following β and α decays.**

Figure 3.9: **State of the art of the ^{7}Be(p, γ)^{8}B measurements.**

the backing material (large effects for heavy backings such as Pt) and on the thickness of the target (large effects for thin targets). Similar predictions for the loss of ^8Li recoil nuclei in $^7Li(d,p)^8Li$ have been confirmed experimentally [95, 96], which could also influence the $^7Be(p,\gamma)^8B$ results when the former reaction is used for normalization. It was thus suggested [96] that the reported $\sigma(E)$ values should include an additional systematic uncertainty of the order of 15%. Omitting some data sets and using different model calculations [62][33], values of $\mathbf{S(0)} = \mathbf{19^{+4}_{-2}}$ **eV b** [1] and $\mathbf{S(0)} = \mathbf{21 \pm 2}$ **eV b** [3] have been recommended for the astrophysical $S(E)$ factor at zero energy.

"It would be especially informative to reverse the usual experimental situation and use a gaseous target of protons and a beam of ^7Be; this reversal would involve different systematic uncertainties, which are often the most important source of errors in difficult experiment" [9].

This approach has been adopted at the 3 MV tandem accelerator in Naples (see figure 3.10), where the absolute cross section $\sigma(E)$ value of $p(^7Be,\gamma)^8B$ (inverted kinematics) in the non-resonant energy region, i.e. at $E_{cm} = 1 \; MeV$ ($E_{lab} = 8 \; MeV$) has been measured. The experiment started 5 years ago with testing procedure using another reaction (in particular the $^{12}C(p,\gamma)^{13}N$ [45]) to verify the feasibility of the measurement of nuclear cross section using the Recoil Mass Separator technique (see section 2.4).

The study involved a ^7Be radioactive ion beam, a windowless H_2 gas target, and a recoil mass separator for the detection of the ^8B recoils. The approach avoided the problems of ^7Be target stoichiometry and allowed to identify the ^8B recoils on the basis of their energy and $\Delta E - E$ characteristics (using a telescope placed at the end of the separator, see previous chapter). Since the ^8B yield was measured concurrently with the $^7Be + p$ elastic scattering yield, the method related ultimately $\sigma(E)$ to the elastic scattering cross section.

Figure 3.10: **Tandem TTT-3 machine available in Naples (upper pannel) and analysing instruments (lower pannel). It is possible recognize the gas target and the Recoil Separator.**
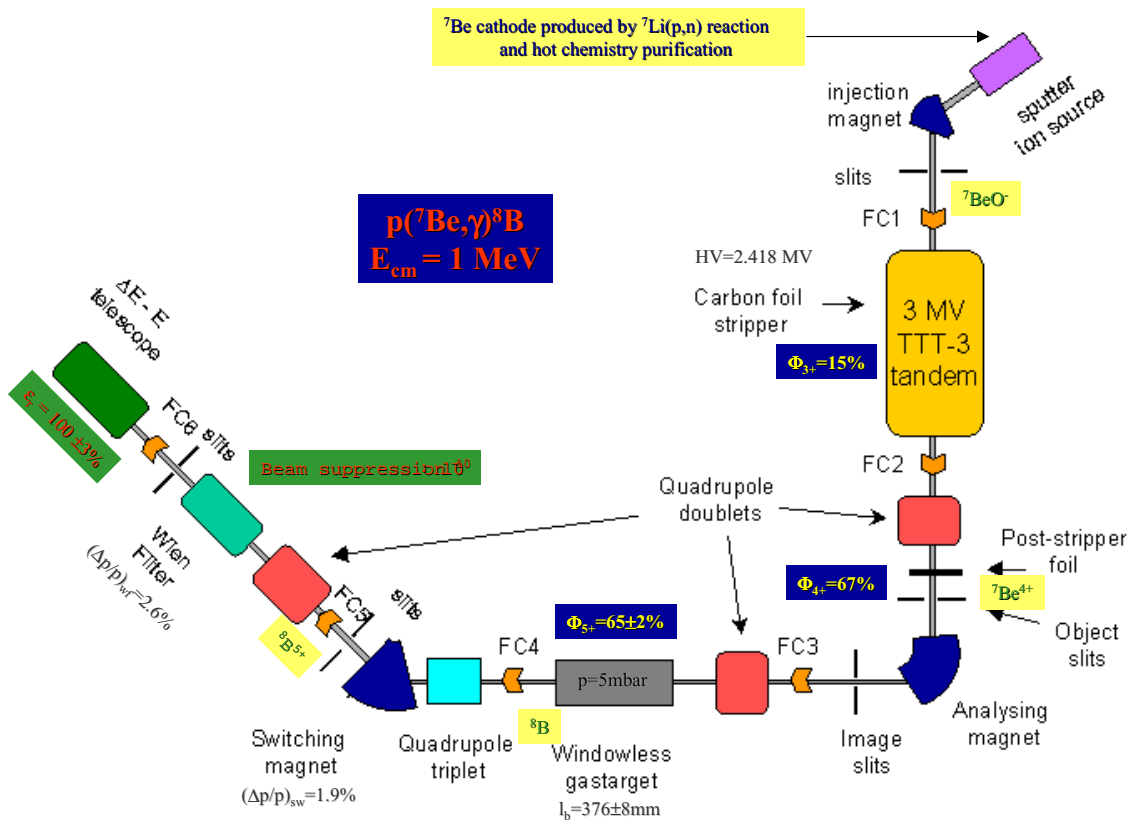
Figure 3.11: **Schematic diagram of the** $3\ MV$ **TTT-3 tandem accelerator at Naples with the relevant informations for the** $^7\mathbf{Be(p,}\gamma\mathbf{)^8B}$ **measurement using the Recoil Separator technique.**

3.2.1 Equipment set-up and experimental procedure

A schematic diagram of the 3 MV TTT-3 tandem accelerator at Naples, the beam transport system, the windowless gas target and the recoil separator is shown in figure 3.11. The set-up has been commonly used for accelerator-mass-spectrometry (AMS) of ^{14}C [20, 101]. Starting from the ion source, we now recall the relevant features of the set-up.

The cesium sputter ion source is a Kingston Scientific model 300 which operates at 25 KV potential, the conically shaped ionizer allows to sputter the elemental

materials nearly homogeneously over an area of up to 5 mm diameter. The negative ion beam of interest is selected by a 35° injection magnet, focused by a gridded lens, and accelerated to the terminal voltage of the tandem. A 5 μgcm^{-2} thick carbon foil inside the TTT-3 machine provides the electron stripping, therefore a positive ion of selected charge emerges from the accelerator. A quadrupole doublet magnet focuses the beam on the object slits of a 90° double focusing analysing magnet which transports the beam on the image slits. A downstream magnetic quadrupole doublet focus the beam in the center of the windowless gas target system. The products of the reaction (recoil ions) together with the beryllium beam (leaky beam) arise from the gas-target and they are focused by a quadrupole triplet on the 30° switching magnet. These are the first two elements of the recoil separator, which as we have seen in chapter 2, allows to separate the boron from the leaky beam. Afterwords the Wien filter makes a velocity selection and the recoil ions are identified in the $\Delta E - E$ telescope, filled with isobutane, placed at the end of the Recoil Mass Separator. A mylar foil is placed in front of the entrance of the chamber. Faraday cups and $X - Y$ steerers are placed along the beam transport system (fig.3.11) to monitor and optimize the beam transmission respectively. A post-stripper carbon foil can be placed in front of the object slits to change the charge state q of the accelerated ion beams.

The ^7Be nuclides were produced using the $^7Li(p,n)^7Be$ reaction, irradiating metallic Li samples with a 11.4 MeV proton beam (20 mA) from the cyclotron in Debrecen, whereby for each sample a ^7Be activity of about 20 GBq was achieved over an irradiation time of about 2 weeks. Using hot chemistry, the activated samples were transformed into nearly pure $^7BeO + Ag$ pills to be used as cathodes in the sputter ion source of the Naples tandem. The procedures applied in the irradiation and hot chemistry are described in [36].

In the sputter source, the ^7Be nuclides were extracted in form of a $^7BeO^-$ molecular ion beam. Setting the 35° injection magnet to mass -23 ions, this beam was accompanied by a $^7LiO^-$ molecular beam. Both beams were focused by a gridded lens and accelerated to the terminal voltage $U = 2.42\ MV$ of the tandem. After stripping

in a $5\mu g/cm^2$ thick C foil, the 8.0 MeV ions of $^7Be^{3+}$ (probability $\Phi_{3+} = 15\%$) and $^7Li^{3+}$ emerged from the accelerator. Inserting a post-stripper C foil ($10\mu g/cm^2$ thick) near the object slits, fully stripped $^7Be^{4+}$ ions were produced with a 67% probability. The $^7Be^{4+}$ ions were selected by the analysing magnet, while the accompanying $^7Li^{3+}$ ions were filtered. A high purity of the resulting $^7Be^{4+}$ beam (25 ppA maximum current) was verified [21].

This $^7Be^{4+}$ beam is focused in the center of the gas target where the elastic scattering and radiative capture processes take place. The protons scattered will be measured by silicon detectors placed around the target chamber and ^8B particles together with incident beryllium arise from the gas target. The differentially pumped gas target has three pumping stages on both sides of the target chamber, which consist of Roots blowers (e.g. WS2000, pumping speed = 2000 m^3/h), turbo pumps (TV360, pumping speed = 360 l/s, and roughing pumps (e.g. D65B, pumping speed = 65 m^3/h). The use of the gas target has several advantages with rispect to hydrogen solid targets: it allows a highly pure composition of the gas target and can withstand deteriorations or build up of impurities. Moreover, the adopted solution of a differentially pumped target avoids the use of pressure-defining windows, which again could be deteriorated by the beam and would be an additional source of background. The beam entered the target chamber through three electrically insulated apertures of high gas-flow impedance (C to A; with diameters $\varnothing$ and distances given in fig. 3.12) and left the chamber through a symmetric set of apertures; these apertures defined the ion beam axis to better than 0.5°. The target chamber was filled with the target gas, via a needle valve, to a pressure p_0. The measurement of the pressure is absolute and independent of the gas used, the accuracy is of 4% with a Baratron capacitance manometer. For the measurement taken into account the gas target is filled with H_2 gas of $p_0 = 5.0$ $mbar$, the three stages pumping system reduced the upstream pressures to $p_1 = 0.19$ $mbar$, $p_2 = 6.2 \cdot 10^{-4}$ $mbar$ and $p_3 = 1.6 \cdot 10^{-5}$ $mbar$ in the regions between the apertures A and B, B and C and outside aperture C, respectively. The disc shaped target chamber has a central ion beam pipe of 12 mm diameter, which
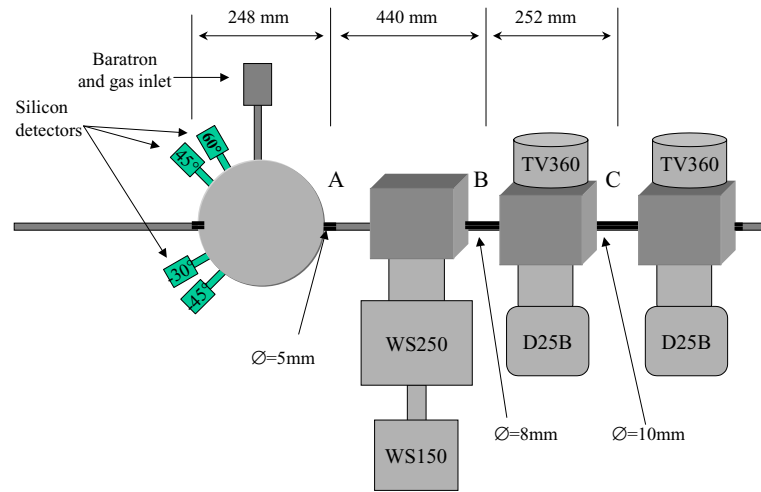
Figure 3.12: **Schematic view of the Naples gas target.**

houses the aperture A. The chamber has several ports radiating from the center of chamber, which is at a distance of $z = 124 \pm 1\ mm$ from the center and they are used as gas inlet, adapter for the Baratron manometer and installation of collimated particle detectors.

The silicon detectors have an active area of 150 mm^2, thickness of 300 μ, energy resolution $\Delta E = 15\ keV$ at $E_\alpha = 5.5\ MeV$. They were collimated by the slit-hole combination in stalled at the ends of a tube of length $113 \pm 1\ mm$ with an horizontal slit of width $s = 2.00 \pm 0.05\ mm$ faced the center of the target chamber and the circular collimator ($r = 5.00 \pm 0.05\ mm$) in front of the detector. The distance from the circular collimator to the center of the target chamber was $d = 173 \pm 2\ mm$. This geometry defined the effective target length seen by the detector along the beam axis [89] as:

$$l^p_{eff} = s \cdot d \cdot \left(f \sin \theta_{lab} \right)^{-1} \tag{3.9}$$

corresponding to a range of scattering angles $\theta_{lab} \pm \Delta\theta_{lab}$. For the angle $\theta_{lab} = 45°$ the solid angle is $\Omega_{lab} = \pi \cdot r^2/d^2 = 2.62\ msr$, considering the reproducibility of single measurement for a given focusing of an ion beam we have $\Delta\theta_{lab} = 0.5°$ and $\Delta\Omega_{lab} = 0.047msr$ [95] and the target length is $\mathbf{l^p_{eff} \cdot \Omega_{lab} = 11.3 \pm 0.4\ mm\ msr}$. The analyzed angles, during the measurement, were $\theta_{lab} = -30°$, $\theta_{lab} = -45°$, $\theta_{lab} = 45°$ and $\theta_{lab} = 60°$.

A quadrupole triplet focuses on the switching magnet (SM) the two beams arising from the gas target (^8B recoils and ^7Be leaky) The switching magnet field selects one charge state: selecting the boron 5^+ state (see section 2.4) provide a first discrimination, since there is no such beryllium state. On the other hand, small angle scattering and charge exchange processes on the beam transport section between the gas target and the magnet can give rise to a residual "leaky" beam of ^7Be particles having an energy charge state combination which matches the rigidity of the recoils ions. In view of the very high intensity ratio at the origin, these leaky beam still overwhelms the recoil one, in spite of the small probability of the above processes. A further purification is then performed by a dispersive velocity analysis, using a crossed field Wien filter, that exploits the velocity difference of particles of equal rigidity and different mass, the combined purification factor is 10^{-10} [45].

The ^8B recoils are finally identified and counted in the $\Delta E - E$ telescope. The identification matrix used for calibration is shown in fig. 3.13. The number of ^8B nuclides from $p(^7Be, \gamma)^8B$, as observed in the $\Delta E - E$ telescope of the recoil separator, I_B, can be related to the $^7Be + p$ elastic scattering yield (i.e. the number of the proton recoils), I_{el}, observed with the particles detectors placed at an angle θ_{lab} in the gas target chamber, by the expression 2.21. To deduce Φ_5 we have studied the charge state distribution as a function of pressure using a ^{11}B beam of $9.625\ MeV$, which has the same velocity as $7\ MeV\ ^8B$. Since the reaction can occur everywhere in the gas target between the entrance and the exit, we have simulated this situation studying the charge state distribution as a function of the pressure. - the results of this analysis is shown in fig. 3.14 -. Indeed, the ^8B particles produced near the entrance
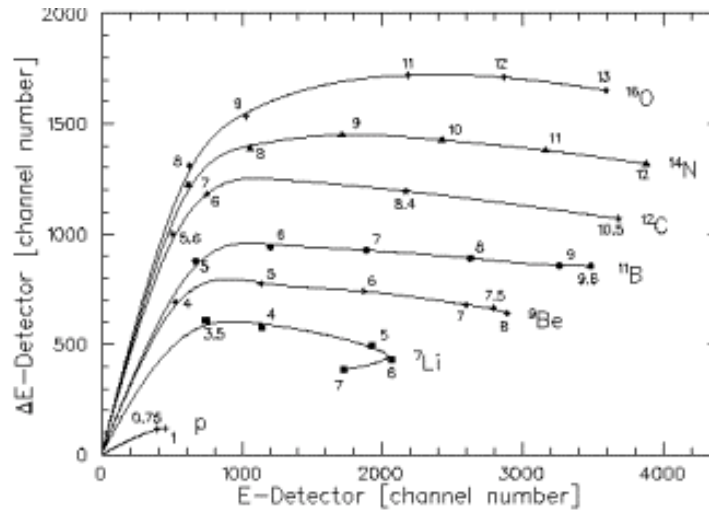
Figure 3.13: **Calibration matrix of the ionization chamber.**

of the gas target see 5 *mbar* of H_2 pressure, but those produced near the exit see an equivalent pressure lower than 5 *mbar*. Folding the probability that the reaction takes place in a certain point of the gas target with the one that the recoil assumes the selected charge state in the path up to the exit of the gas target, one can obtain the average charge state of the emerging particles from the gas target: $\phi_{5+} = 65$ %. The recoil beam transmission in the separator has been measured concurrently with the momentum acceptance of the system, using as test the $^{12}C(p, \gamma)^{13}N$ reaction, for which the cross section is known precisely from direct kinematics measurements [45]. For the switching magnet a value of $(\Delta p/p)_{sm} = 1.9\%$, and for the Wien filter $(\Delta p/p)_{sm} = 2.6\%$ were found. The maximum angular dispersion at 8 *MeV* laboratory energy of $^7Be(p, \gamma)^8B$ reaction is 0.2°, while the momentum spread is $(\Delta p/p)_{sm} = 0.7\%$, largely in the range of the recoil separator. The measured cross section for $^{12}C(p, \gamma)^{13}N$ at $E_{cm} = 0.841$ *MeV* is in very good agreement with the literature value [45]: this confirms the feasibility of the method and gives an indirect confirmation that the transmission through the separator, determined by beam current measurements
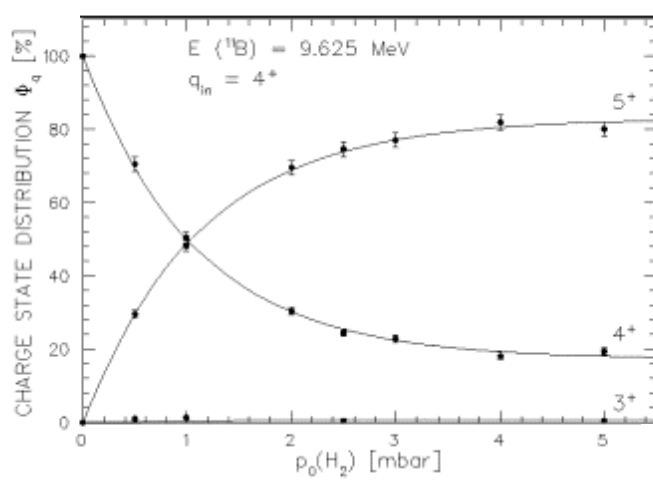
Figure 3.14: **Charge state probability of ^{11}B as a function of the pressure of the gas target.**

as $\varepsilon = (100 \pm 3)\%$, is correctly evaluated. Finally, as already mentioned in section 2.4 to deduce the cross section of $^7Be(p, \gamma)^8B$, we need an absolute measurement of $^7Be + p$ elastic scattering cross section. Next section is devoted to such measurement.

3.2.2 Measurement of $^7Be + p$ elastic scattering cross section

The elastic scattering cross section $\sigma_{cm}(45°, E_{cm})$ was measured using the so called gas mixture method, which relates the unknown cross section to other known cross sections. In particular, to measure the $^7Be(p, p)^7Be$ cross section at 8 Mev laboratory energy, first we have measured that of $^7Li(p, p)^7Li$ at similar energy. We have used a target filled with a fixed mixture of H_2 and ^{40}Ar and we have counted the protons scattered by the incident beam (lithium or beryllium) and the incident particles scattered by the argon target at different angles and considering different energies. First we have guided in the gas target a 2 MeV (or 3 MeV) laboratory energy beam of ^7Li, counting proton and argon elestic particles; afterwards we have guided an 8 MeV laboratory energy beam of ^7Li. By the comparison of the yields (see below) we have obtained the $^7Li + p$ elastic scattering cross section at 8 MeV laboratory energy. Indeed, since the processes $^7Li + p$ at 2 MeV (or 3 MeV) laboratory energy and $^7Li +^{40}Ar$ at 2 MeV (or 3 MeV) and 8 MeV laboratory energy follow the Rutherford law (see, again, below), the only unknown cross section is that of $^7Li + p$ at 8 MeV laboratory energy. The same technique is used considering the processes: $^7Li + p$, $^7Li +^{40}Ar$, $^7Be + p$ and $^7Be +^{40}Ar$ at 8 MeV laboratory energy. Note that again there is just one unknwon process: the $^7Be + p$ elastic scattering, so the gas mixture method can be applied.

Generally speaking, if we consider two gases in the gas target and two interacting ion beams, we can obtain the absolute elastic cross section of one of the four involved reactions knowing the other ones. We remind that the number N_s of particles scattered at an angle θ and at an incident energy E is:

$$N_s(\theta, E) = \sigma_{lab}(\theta, E)l_{eff}\Omega_{lab}N_tN_p = \sigma_{cm}(\theta, E)\frac{\Omega_{cm}}{\Omega_{lab}}l_{eff}\Omega_{lab}N_tN_p \qquad (3.10)$$

where N_t and N_p are the number of projectile and target particles respectively and $\sigma_{cm}(\theta, E)$ is the elastic cross section. From this equation obviously follows that:

$$\sigma_{cm}(\theta, E) = \frac{N_s(\theta, E)}{l_{eff}\Omega_{lab}N_tN_p}\frac{\Omega_{cm}}{\Omega_{lab}} \tag{3.11}$$

We can call A and B the elastic scattering processes, which involve the first beam with the two components of the gas mixture, and C and D the ones related with the second beam. We can write the relation:

$$\frac{[\sigma_{cm}(\theta, E)]_A}{[\sigma_{cm}(\theta, E)]_B} = \frac{N_s^A(\theta, E)[\frac{\Omega_{cm}}{\Omega_{lab}}]_A}{N_s^B(\theta, E)[\frac{\Omega_{cm}}{\Omega_{lab}}]_B}\frac{N^I}{N^{II}} \tag{3.12}$$

where I and II refer to the two target isotopes. A similar relation can be written for C and D. Since from kinematics arguments we know that:

$$\frac{[\frac{\Omega_{cm}}{\Omega_{lab}}]_A}{[\frac{\Omega_{cm}}{\Omega_{lab}}]_B} = \frac{[\frac{\Omega_{cm}}{\Omega_{lab}}]_C}{[\frac{\Omega_{cm}}{\Omega_{lab}}]_D} \tag{3.13}$$

it is possible to write:

$$\frac{[\sigma_{cm}(\theta, E)]_A}{[\sigma_{cm}(\theta, E)]_B}\frac{[\sigma_{cm}(\theta, E)]_D}{[\sigma_{cm}(\theta, E)]_C} = \frac{N_s^A(\theta, E)}{N_s^B(\theta, E)}\frac{N_s^D(\theta, E)}{N_s^C(\theta, E)} \tag{3.14}$$

Coming back to the measurement, first, we have guided ^7Li beams of 2, 3 and 8 MeV in the gas target filled with an $Ar-H$ mixture. Since the Coulomb barrier of argon has energy of about 18 MeV, the lithium elastic scattering at all the energies considered follows Rutherford law. Therefore the elastic scattering cross section is:

$$\sigma_{cm}(\theta, E)]_s^R = 1.296\left(\frac{Z_{Li}Z_{Ar}}{E}\right)^2\left(\frac{M_{Li} + M_{Ar}}{M_{Ar}}\right)^2\frac{1}{\sin(1/2\theta)^4}\frac{mb}{sr} \tag{3.15}$$

Also the elastic scattering $^7Li + H$ at 2 and 3 MeV follows the Rutherford law, as confirmed by the ratio between the number of protons scattered by lithium beam and the lithium particles scattered on argon target being constant as a function of energy between 2 and 3 MeV (see figure 3.15 and table 3.2.2), Therefore, from the measured yields of ^7Li ions scattered by Ar and of H recoils from $^7Li + H$ elastic scattering at 2 and 3 MeV the relative $l_H\Omega_{lab}(\theta)$ for the 30°, −45° and 60° detectors
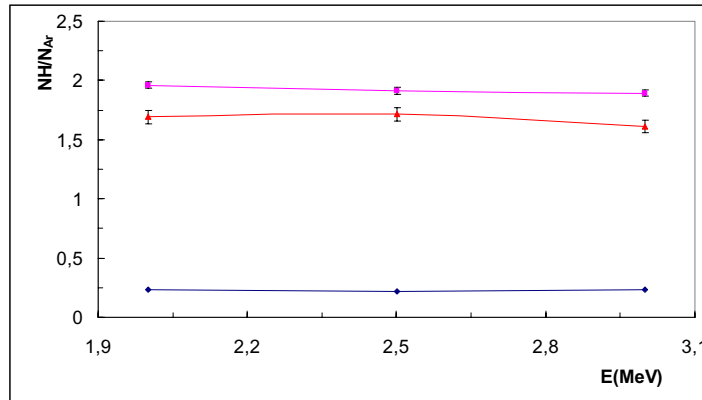
Figure 3.15: **Ratio between the number of protons scattered by lithium beam and the lithium particles scattered on argon target as afunction of the energy.**

were deduced, as well as the ratio of H to Ar number densities, N_H/N_{Ar}. Note that we have a value for 45° angle of $l_H\Omega_{lab}(\theta)$ see equation 3.9. From the yields measured at 8 MeV incident energy, the absolute values of $\sigma_{cm}^{Li}(\theta, E_{cm}^{Li})$ at 30°, 45° and 60° were deduced, with $E_{cm}^{Li} = 975\ keV$, as calculated taking into account the energy loss in the target.

Typical spectra for each angle are shown in figure 3.16, where it is possible to recognize the recoil protons from ^7Li scattering and the scattered ^7Li on Ar peaks. Moreover there is another peak on the left of proton peak, which corresponds to the energy of Ar scattered particles. This peak is larger proportionally to the energy of the incident beam. To subtract the Ar scattering counts we have fitted the peaks with the non symmetrical exponential function:

$$f(E) = \frac{H}{1 + e^{\frac{|E-E_0|-\sigma}{D}}} \tag{3.16}$$

The results of the fit is plotted in fig. 3.17. The results of the analysis give as a ratio between absolute cross section of $Li + p$ elastic scattering reaction and Rutherford

Table 3.3: **In table the results of the measurements of the scattering cross sections for $Li + p$ and $Li + Ar$ processes at 2, 3 and 8 MeV energies. Starting from the first column for each energy we report: the laboratory silicon detector angles, the value of $l_{eff}\Omega_{lab}^{rel}$, the scattering angles for lithium particles scattered by argon in center of mass system corresponding to the detector angles, the number of lithium particles counted during the measurement, the scattering angles for proton particles in center of mass system corresponding to the detector angles, the number of proton particles counted during the measurement and the ration between the proton and lithium particles.**

| 2 MeV		$Li + Ar_{eje}$		$Li + H_{res}$		
θ_{lab}	$l_{eff}\Omega_{lab}^{rel}$	θ_{cm}	N_{Ar}	θ_{cm}	N_H	N_H/N_{Ar}
$-30°$	1.48	$-35°$	53792 ± 232	$-60°$	9110 ± 103	0.17 ± 0.01
$-45°$	1	$-52°$	7831 ± 88	$-90°$	11299 ± 113	1.44 ± 0.02
$45°$	0.99	$52°$	7636 ± 87	$90°$	11382 ± 111	1.49 ± 0.02
$60°$	0.80	$69°$	2072 ± 46	$120°$	28067 ± 175	12.25 ± 0.02
3 MeV		$Li + Ar_{eje}$		$Li + H_{res}$		
θ_{lab}	$l_{eff}\Omega_{lab}^{rel}$	θ_{cm}	N_{Ar}	θ_{cm}	N_H	N_H/N_{Ar}
$-30°$	1.48	$-35°$	105767 ± 325	$-60°$	18223 ± 176	0.17 ± 0.01
$-45°$	1	$-52°$	14902 ± 122	$-90°$	21776 ± 158	1.46 ± 0.01
$45°$	0.99	$52°$	14728 ± 121	$90°$	21815 ± 157	1.48 ± 0.01
$60°$	0.80	$69°$	4110 ± 64	$120°$	50091 ± 237	12.19 ± 0.02
8 MeV		$Li + Ar_{eje}$		$Li + H_{res}$		
θ_{lab}	$l_{eff}\Omega_{lab}^{rel}$	θ_{cm}	N_{Ar}	θ_{cm}	N_H	$\sigma_{cm}/\sigma_{cm}^R$
$-30°$	1.48	$-35°$	40603 ± 202	$-60°$	16844 ± 135	2.45 ± 0.02
$-45°$	1	$-52°$	5896 ± 77	$-90°$	11169 ± 113	1.31 ± 0.01
$45°$	0.99	$52°$	5704 ± 76	$90°$	11209 ± 112	1.32 ± 0.01
$60°$	0.80	$69°$	1619 ± 40	$120°$	19660 ± 163	1.01 ± 0.02
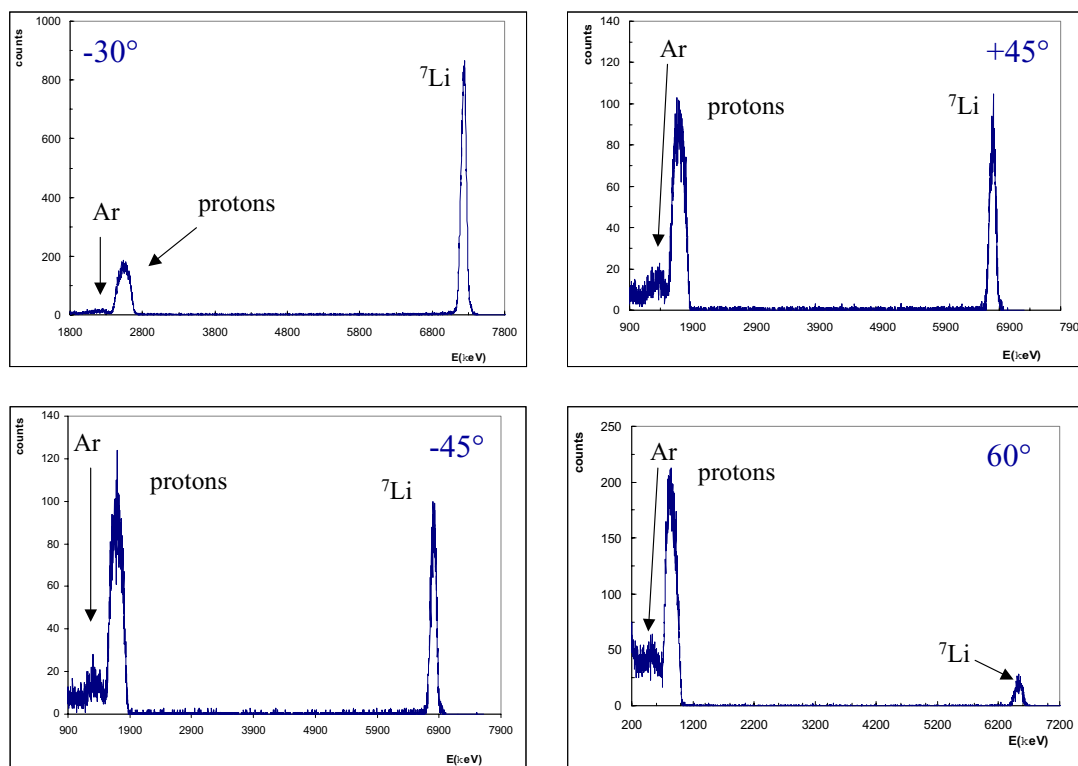
Figure 3.16: **Typical silicon spectra. In particular in figure the spectra of the four angles considered are shown. It is possible recognize the peaks corresponding to argon, proton and lithium particles.**
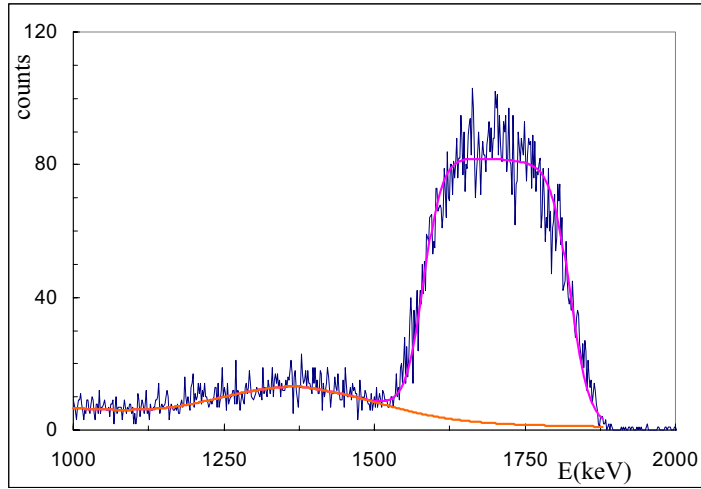
Figure 3.17: **Subtraction of background from the proton peak due to argon particles scattered by the lithium beam.**

one at $975\ keV$ center of mass energy the values:

$$
\begin{aligned}
\frac{\sigma_{cm}}{\sigma_{cm}^{R}}(30°, 975\ keV) &= 2.45\ \pm\ 0.02 \\
\frac{\sigma_{cm}}{\sigma_{cm}^{R}}(45°, 975\ keV) &= 1.31\ \pm\ 0.01 \\
\frac{\sigma_{cm}}{\sigma_{cm}^{R}}(60°, 975\ keV) &= 1.01\ \pm\ 0.01 \quad\quad (3.17)
\end{aligned}
$$

Then two runs were performed bombarding, again, the $Ar - H$ mixture with an $8\ MeV\ ^{7}Li$ beam and an $8\ MeV\ ^{7}Be$ beam. The ratios of elastic scattering yields in the two runs provided the absolute elastic scattering cross section $\sigma_{cm}^{Be}(\theta, E_{cm}^{Be})$ at $E_{cm}^{Be} = 954\ keV$, by means of the knowledge of the elastic scattering of the other three processes (see table 3.2.2). The absolute cross section of $Be + p$ elastic scattering

Table 3.4: **In table the results of the measurements of the scattering cross sections for $^7Li + p$, $^7Li + Ar$, $^7Be + p$ and $^7Be + Ar$ processes at 8 MeV energy. Starting from the first column for each energy we report: the laboratory silicon detector angles, the value of $l_{eff}\Omega_{lab}^{rel}$, the scattering angles for lithium or beryllium particles scattered by argon in center of mass system corresponding to the detector angles, the number of lithium or beryllium particles counted during the measurement, the scattering angles for proton particles in center of mass system corresponding to the detector angles, the number of proton particles counted during the measurement and the ration between the proton and lithium or beryllium particles.**

8 MeV		$Li + Ar_{eje}$		$Li + H_{res}$		
θ_{lab}	$l_{eff}\Omega_{lab}^{rel}$	θ_{cm}	N_{Ar}	θ_{cm}	N_H	
$-30°$	1.48	$-35°$	15893 ± 126	$-60°$	4228 ± 66	
$-45°$	1	$-52°$	2275 ± 48	$-90°$	2713 ± 56	
$45°$	0.99	$52°$	2263 ± 48	$90°$	2743 ± 55	
$60°$	0.80	$69°$	624 ± 25	$120°$	5012 ± 77	
8 MeV		$Be + Ar_{eje}$		$Be + H_{res}$		
θ_{lab}	$l_{eff}\Omega_{lab}^{rel}$	θ_{cm}	N_{Ar}	θ_{cm}	N_H	$\sigma_{cm}/\sigma_{cm}^R$
$-30°$	1.48	$-35°$	546 ± 23	$-60°$	48 ± 7	0.81 ± 0.12
$-45°$	1	$-52°$	87 ± 9	$-90°$	70 ± 10	0.95 ± 0.13
$45°$	0.99	$52°$	77 ± 9	$90°$	78 ± 9	1.07 ± 0.13
$60°$	0.80	$69°$	21 ± 5	$120°$	239 ± 18	1.42 ± 0.11

reaction at 954 keV center of mass energy is:

$$\frac{\sigma_{cm}}{\sigma_{cm}^R}(30°, 954 \ keV) = 0.81 \pm 0.12$$

$$\frac{\sigma_{cm}}{\sigma_{cm}^R}(45°, 954 \ keV) = 1.01 \pm 0.09$$

$$\frac{\sigma_{cm}}{\sigma_{cm}^R}(60°, 954 \ keV) = 1.42 \pm 0.11 \qquad (3.18)$$

Note that the deduced values are not affected by the fact that $E_{cm}^{Be} \neq E_{cm}^{Li}$, but they refer to a c.m. energy which is slightly different from that of the reaction cross section measurement. The measurement of boron recoil fragments the gas target was filled only with H_2. This reduces the energy lost by the incident beam, so that the extracted values 3.18 cannot beused directly in eq. 2.21, as they refer to a slightly different energy. The variation of σ/σ_R for $^7Be + p$ elastic scattering values between
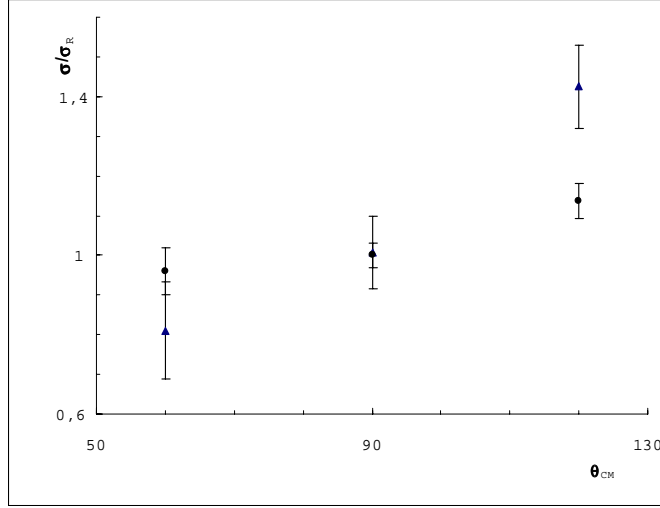
Figure 3.18: **Absolute elastic scattering cross sections for ^7Be+p at $E_{cm} = 954\ keV$ (triangles) and relative cross section for ^7Be+p at $E_{cm} = 990\ keV$ (dots).**

two energies can be attributed to the different importance of the interference with the 39 keV broad resonance at $E_R = 632\ keV$. This effect is expected to decrease with increasing energy above the resonance and to be absent at $\theta_{cm} = 90°$ $(\theta_{lab} = 45°)$, due to the p-wave character of the resonant term and the predominance of s-waves in the non resonant scattering channel . Indeed, this is confirmed by the comparison of the absolute σ/σ_R values measured at $E_{cm}^{Be} = 954\ keV$ with the relative ones deduced from the data at $E_{cm}^{Be} = 990\ keV$, also shown in fig. 3.18 after normalization to $\sigma/\sigma_R = 1$ at $\theta_{cm} = 90°$. For our purpose we can then neglect the difference between the elastic scattering cross section at $45°$ angle for the two incident energies:

$$\frac{\sigma_{cm}}{\sigma_{cm}^R}(45°, 990\ keV) = \frac{\sigma_{cm}}{\sigma_{cm}^R}(45°, 954\ keV) = 1.01 \pm 0.09 \qquad (3.19)$$

Figure 3.19: **Final matrix with the 13 counts of ^8B.**

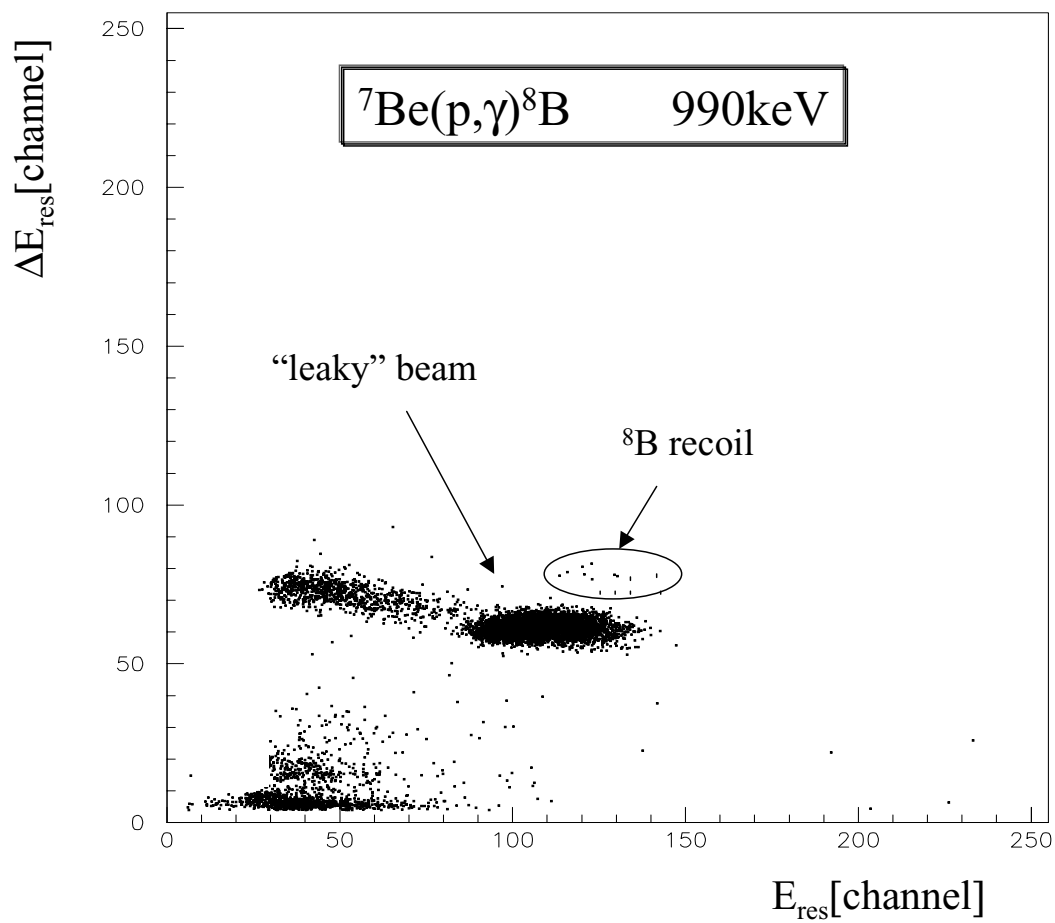Table 3.5: **Final results of p(^{7}Be, γ)^{8}B measurement starting from the first column we report the laboratory silicon detector angles, the value of $l_{eff}\Omega_{lab}^{rel}$ and Ω_{cm}/Ω_{lab}, the scattering angles for proton particles in center of mass system corresponding to the detector angles, the number of proton particles counted during the measurement of boron particles and the number of ^{8}B recoils.**

8 MeV			Be + H$_{el}$		^{8}B$_{rec}$
θ_{lab}	$l_{eff}\Omega_{lab}^{rel}$	Ω_{cm}/Ω_{lab}	θ_{cm}	N_H	
30°	1.48	3.46	60°	282 ± 17	$N_{^8B}$
45°	1	2.83	90°	$\mathbf{365 \pm 11}$	$\mathbf{13.0 \pm 3.6}$
60°	0.80	2.00	120°	944 ± 37	

3.2.3 The cross section and the astrophysical factor at $990\ keV$ center of mass energy

The above value in the equation 3.19 has to be used to extract the reaction cross section:

$$\sigma_r(E_{cm}) = \frac{N_B}{N_H}\frac{l_H\Omega_{lab}(\Omega_{cm}/\Omega_{lab})}{(\Phi_{5^+}\ \varepsilon_B)}\ \sigma_{cm}(45°, E_{cm}) \tag{3.20}$$

In figure 3.19 we show the final matrix with the 13 ^8B counts obtained during the runs. In table 3.2.3 we resume the data taken during the RMS measurement.

The resulting value is $\sigma_r(990\ keV) = (0.40 \pm 0.12)\mu b$, which corresponds to an astrophysical S factor $S(990\ keV) = (16.5 \pm 4.8)\ eV\ b$. Scaling this value with the energy dependence of [33], we obtain $S(0) = (15.3 \pm 4.5)\ eV\ b$. The experiment described above demonstrates the feasibility of the techniques used in the study of this reaction so critical for the solar neutrino problem. An improvement of the statistical uncertainty attainable with the present technique could be achieved - besides the possibility of using a prohibitive amount of activity of the order of 1 TBq - by increasing the accelerator transmission and/or by using a more probable charge state for the accelerated 7 Be ions (i.e. $q = 2^+$ with $\Phi2^+ = 70\%$), which would require a terminal voltage not accessible to our accelerator. Within the present statistical uncertainty this result is consistent with the values recommended recently [62] [33]. However,
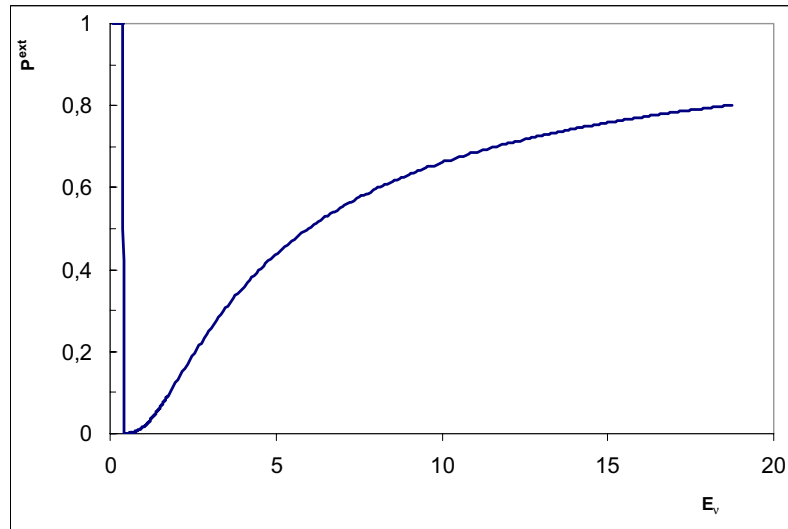
Figure 3.20: **Survival probability for the small angle solution in the MSW framework using the** $15\ eVb$ **for** $\mathbf{S_{17}(0)}$**.**

a closer comparison with individual data sets considered in the above compilations shows an agreement at the level of 1σ just with the lowest $S(0)$ values obtained in the most recent delayed activity measurements [65] [108] [40] [50]. In spite of this large statistical uncertainty, the present result indicates a possible overestimation of $S_{17}(0)$ from previous measurements, due to the systematic effects discussed above. We want now to show how a reduction of $S_{17}(0)$ would influence the conclusion drawn with the application of the MSW theory to the analysis of the solar neutrino measurements (section 3.1).

Using, as value of the $^7Be(p,\gamma)^8B$ reaction rate for solar model calculation, that resulting by $S(0) = 15.3$, we find an unique solution for solar neutrino problem in the framework of MSW theory. Indeed, the χ^2 minimum for the large mixing angle is suppressed and that for the small mixing angle (see figs. 3.20 and 3.21)yields the following values of the free parameters:

84
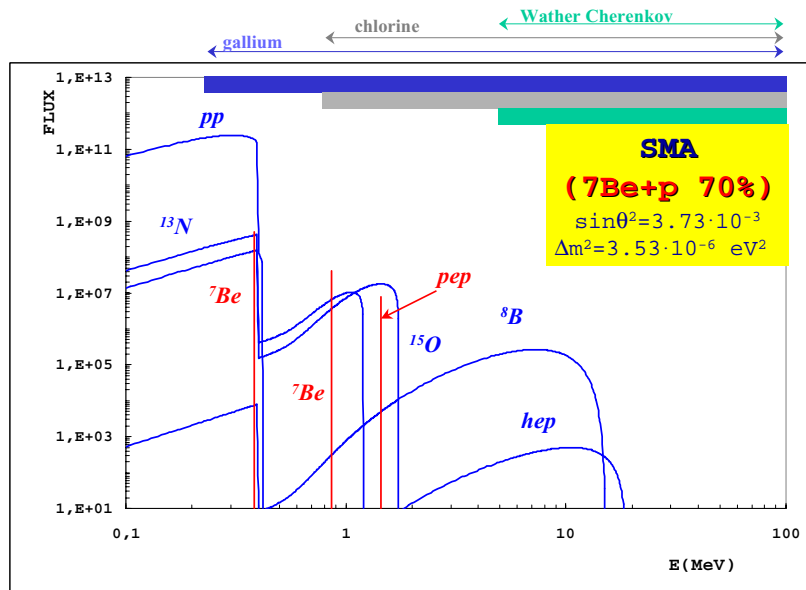
Figure 3.21: **Solar Energy Spectrum considering the small angle solution in the MSW framework using the** 15 eVb **for** $\mathbf{S_{17}(0)}$**.**

$\mathbf{sin^2 2\theta} = (\mathbf{3.73^{+0.32}_{-0.33}}) \cdot \mathbf{10^{-3}}$, which means $\theta \sim 4°$ and $\delta\mathbf{m^2} = (\mathbf{3.53 \pm 0.12}) \cdot \mathbf{10^{-6}\ eV^2}$ with a $\chi^2 = \mathbf{0.98}$. It can be seen, by comparison with the values reported in section 3.1, that the squared-mass difference is not effected by the $S_{17}(0)$ value, while the mixing angle parameter is reduced from $\mathbf{sin^2 2\theta} = (\mathbf{6.69^{+0.36}_{-0.34}}) \cdot \mathbf{10^{-3}}$ to $\mathbf{sin^2 2\theta} = (\mathbf{3.73^{+0.32}_{-0.33}}) \cdot \mathbf{10^{-3}}$. However, it has to be noted that in the above fit procedure the statistical uncertainty in $S_{17}(0)$ is not included, so that the quoted reduction in $\sin^2 2\theta$ awaits for a confirmation from a more precise determination of the S-factor of the $^7Be(p,\gamma)^8B$ reaction.

Chapter 4

The ^{12}C$(\alpha, \gamma)^{16}$O reaction

"*The rate of the $^{12}C(\alpha, \gamma)^{16}O$ during hydrostatic helium burning is of vital interest for explosive nucleosynthesis. It is this process that determines the abundances of ^{12}C and ^{16}O in the star, and thereby sets the stage for explosive burning...The rate is determined by the 7.115 MeV level in the ^{16}O compound nucleus. At present the reduced width θ_α^2 of this resonance for α captures is* **not known**." These were the words used by Arnett in his review included in the 1973 issue of the Ann.Rev.A.A to point out the importance of this reaction in determining the final yields coming from the explosion of a supernova event and the frustrating situation that this rate was not known. The following 30 years did not change much the situation, even if we now understand that it is not only the reduced width of the 7.115 MeV level in ^{16}O which determines the rate (see 4.4).

Since this process directly operates in the He burning phase, determining all the further evolution of a star - because it controls the chemical composition of the matter left by the He burning -, all model calculation for stars which burns helium ($M_{star} > 0.55 M_\odot$) will be affected by the adopted rate. Reasercher's efforts devoted to obtain information about the effective rate of this reaction using astrophysical arguments are vanished by the fact that the $^{12}C(\alpha, \gamma)^{16}O$ reaction occurs in a convective environment. Indeed, differences in the reaction rate value can be simulated by changes in convection treatment, since the final abundance of carbon and oxygen

critically depends on the convection choices. For these reasons, the cross section $\sigma(E)$ should be known with a precision of at least 10%. In spite of tremendous experimental efforts over nearly 30 years, one is still far from this goal (a recent compilation, NACRE [3], quotes an uncertainty larger than 100%).

In the next sections we will underline the role of some convection mechanisms (overshooting and semiconvection) which take place at the border of the convective core (section 4.1); we will present a set of model calculation for stars with mass in the range of $0.8 \geq M/M_\odot \geq 25$ up to the end of the helium burning, using two different values of the $^{12}C(\alpha,\gamma)^{16}O$ reaction rate and we will perform some tests changing the convection assumptions (section 4.2); moreover, we will discuss the results of the evolution of $25 M_\odot$ star up to explosion as a type II supernova (section 4.3). Then we will show the experimental situation of the measurement of the $^{12}C(\alpha,\gamma)^{16}O$ and the status the Recoil Mass Separator project in Bochum, which aims to the study of the reaction in inverse kinematics (4.4).

4.1   Overshooting and semiconvection

In the first chapter we have described the "standard" treatment of the convection (section 1.2.2), while now we want to discuss some particular convective instabilities, which may occur at the border of the convective core. Indeed the transformation of some elements in others, which have different opacity, can change the thermal gradient.

In the low mass stars during the central He burning, helium is converted in carbon first and in oxygen later. The increase of the ^{12}C and ^{16}O abundances in the convective core raises the opacity so that a jump in the radiative gradient forms at the border of the convective core. This is a condition of unstable equilibrium in the sense that the possible mixing (by whichever phenomenon) of the radiative zone at the border of the convective region within the core itself would switch these layers from a stable to an unstable condition. The reason is that the C brought in the (previously) radiative
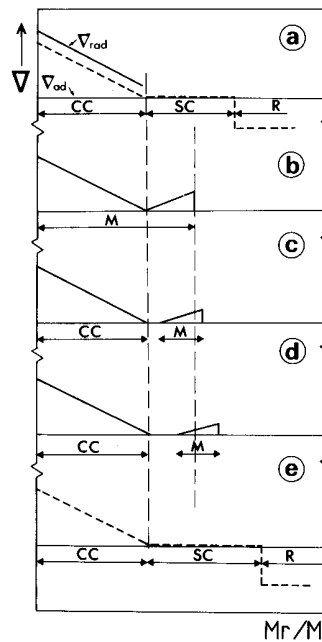
Figure 4.1: **The figure shows how the profile of the radiative gradient is modified by the Semi-Convective region. Indeed, in the five pictures it is shown the formation of a region in which the matter is only partially mixed. Dashed lines represent the initial and final profile of the radiative gradient. The Convective Core, the Semi-Convective and the radiative layers are indicated. The extent of convective mixing during the intermediate phases is indicated by the label M.**

layer raises the radiative gradient (through the opacity) so that it becomes intrinsically convectively unstable. This phenomenon, usually called "induced" overshooting, does not contain any free parameter which may be adjusted by hand since the process of "growth" of the border of the convective core is fully controlled by the requirement that the jump in the radiative gradient is canceled out. The word "induced" refers to the fact that this phenomenon is induced by the conversion of He in C and O.

When the central He abundance drops below, ~ 0.6 by mass fraction the radiative gradient does not decrease any more monotonically moving from the center towards the border of the convective core but it forms a minimum before reaching the outer border of the core. This occurrence triggers the formation of a region in which the

matter is only partially mixed: the condition which controls the degree of mixing occurring in this region is that the radiative gradient equates the adiabatic one (this equality is controlled, once again, by the opacity which, in turn, depends on the local abundances of C and O in these layers). This is the so called "semiconvective" region which forms in low mass stars [23] (see figure 4.1).

Since the "induced" overshooting and semiconvection completely depend on the fact that the opacity is a strong function of the chemical composition, it is clear that they become progressively less important, and eventually disappear, as the initial mass of a star increases because the electron scattering (which does not depend on the chemical composition in an environment deprived of H) becomes the main source of the opacity. In practice the semiconvective layer disappears for masses above $\sim 5\ M_\odot$ while the "induced" overshooting remains at least partially efficient up to $\sim 20\ M_\odot$.

The confirmation that these phenomena probably occur in low mass stars is mainly supported by the star counts in the galactic globular clusters. Note that these clusters are populated by coeval stars with different initial masses and so more massive stars burn faster a given element because of the larger energy lost by the surface ($L \propto M^3$). The ratio between the He burning stars (Horizontal Branch stars) and those ascending along the Giant Branch (see figure 4.2) can be explained only if the central He burning timescale is the one obtained by including these two phenomena (see again [23]). During the latest part of the central He burning (i.e. when the He drops below 0.1 by mass fraction), it has long been found that a runaway of the outer border of the convective core occurs (usually called **Breathing Pulse** [22]): its main effect is that of engulfing fresh He towards the center and hence that of prolonging the central He burning lifetime. Though a discussion on the real existence of these instabilities goes well beyond the purposes of this thesis, here we want simply remark that their inclusion or suppression significantly alters also the abundances of C and O at the end of the He burning.
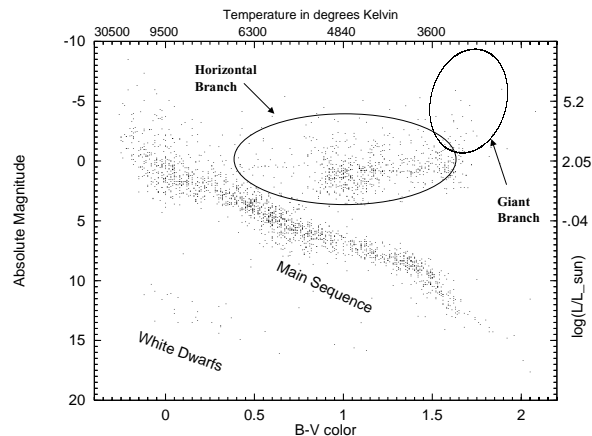
Figure 4.2: **Typical HR diagram.**

In the field of massive stars the word overshooting is used to mention the possibility that convective bubbles may escape the classical border of a convective region and, hence, induce the mixing of a region larger than classically allowed by the strict adoption the Schwartzschild criterion. This is a mechanical phenomenon which is not confined to a specific evolutionary phase but which may be present at the border of any convective region. The extension (having accepted that it exists) of this overshooted region is, in principle, totally arbitrary and usually parameterized by imposing that the convective bubbles may reach a maximum extension x times the pressure scale height (H_p). The existence of a convective core larger than permitted by the Schwarzchild criterion was invoked in the past in order to explain some observational data [44, 69, 102]. Though we do not intend to discuss here the possible existence or not of a mechanical overshooting, it must be said, for sake of completeness, that during the years the size of this phenomenon in the central H burning phase progressively reduced from $\simeq 1\ H_p$ down to less than $0.2\ H_p$.

The word semiconvection is used, in this frame, to indicate the partial mixing which (would) occur at the end of central H burning in the region of variable chemical composition left by the receding H-convective core. Just to be clearer: the convective
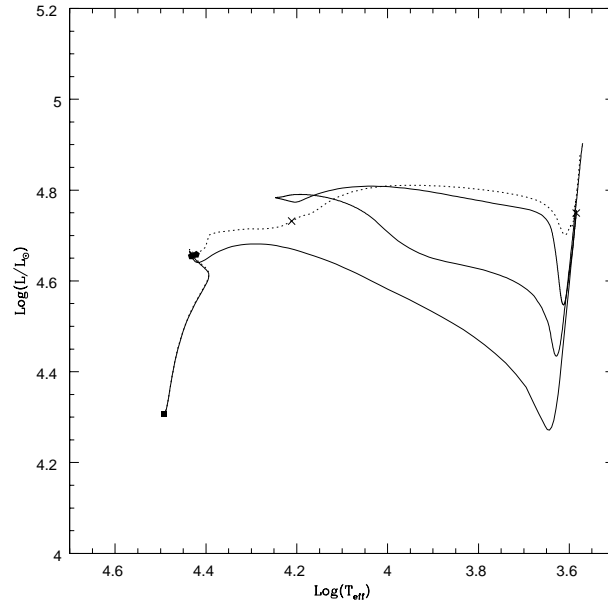
Figure 4.3: **Comparison between the run with the mixing of the H semi-convective shell (dashed line) and that without mixing (solid line). The cross represents the starting of the helium burning.**

core which forms during the central H burning phase of massive stars progressively shrinks (in mass) as the H is converted in He leaving behind a gradient of molecular weight. The responsible of such a shrinking is mainly the opacity which is dominated in this case by the electron scattering and hence lowers together with the H abundance. When the star exhausts the H in the center and readjusts on a structure supported by a shell burning, the radiative gradient overcomes the adiabatic one within these layers showing a gradient of chemical composition. Quite unfortunately, while these layers would be definitely convectively unstable if the Schwarzchild criterion were adopted to asses their stability, the adoption of the Ledoux (eq. 1.30) criterion would maintain these layers stable. Observational constraints [44] mainly related to the observed number ratio between red and blue supergiants seem to favor a partial (or even negligible) amount of mixing in the H (semi)-convective shell of massive stars leaving the MS. Note that the choice about the semiconvective shell is related to the

number of Red and Blue supergiants, since the mixing implies that the stars start the helium burning as a Blue stars, will not mixing the star firstly becomes a Red giant and after will burn the helium (see fig. 4.3).

Also in this case we do not want to discuss the validity of the Ledoux criterion or the efficiency of mixing when a gradient of chemical composition is present, but it is worth noting that the adoption of this criterion and, what it is more important, the specific algorithm adopted to partially mix the matter can significantly alter the possible ingestion of fresh He during the final part of the central He burning phase and hence both the He burning itself and the final C and O abundances. We will present at the end of the next section a numerical test which simulates the ingestion of a little amount of fresh helium when the central helium abundance is lower than $Y < 0.075$. This fresh helium will serve only to produce oxygen via $^{12}C(\alpha, \gamma)^{16}O$ reaction changing **drastically** the final C and O abundance.

Before closing this section let us clearly state that our **standard** computations are obtained by adopting always the Schwarzchild criterion, but in the central He burning phase where both the "induced" overshooting and semiconvection (i.e. the typical phenomena present in low mass He burning stars) are properly taken into account if present; while the Breathing Pulses are quenched by forcing the central He abundance to be a monotonic not increasing function of time.

4.2   Influence of the $^{12}\mathbf{C}(\alpha, \gamma)^{16}\mathbf{O}$ reaction rate on the central Helium Burning phase

Theoretical efforts devoted to constrain the rate of $^{12}C(\alpha, \gamma)^{16}O$ process on the basis of some "observables" have been initiated by Arnett, first, and by Weaver and Woosley, later. Arnett [4, 5] was the first to point out that the observed solar abundances of the carbon and oxygen could be used to constrain the efficiency of the $^{12}C(\alpha, \gamma)^{16}O$ cross section. On the same guideline, Weaver and Woosley [109] also tried to fix this rate by comparing yields obtained by adopting different rates for this process with
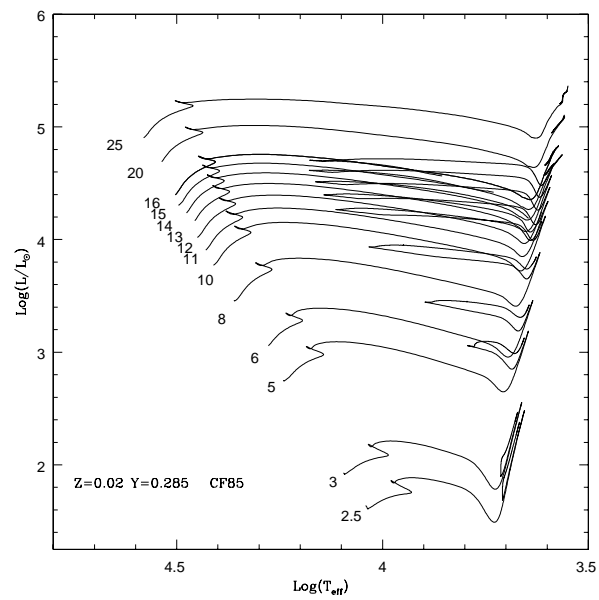
Figure 4.4: **Complete track set in HR theoretical diagram for the computed models using for the value of the ^{12}C$(\alpha,\gamma)^{16}$O reaction rate the CF85.**
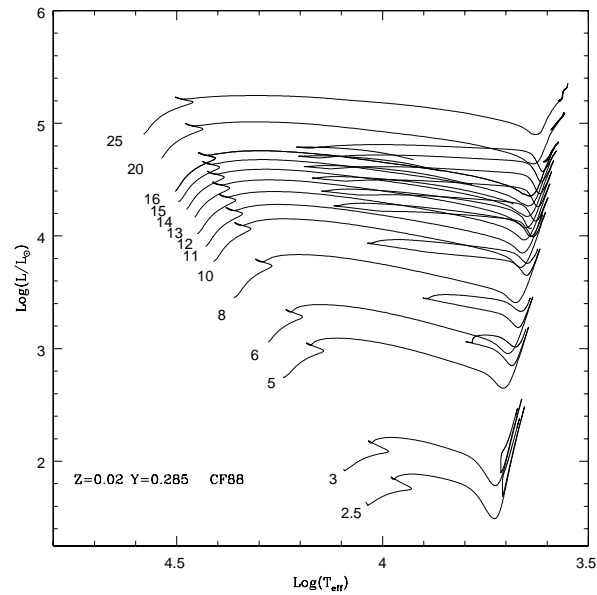
Figure 4.5: **Complete track set in HR theoretical diagram for the computed models using for the value of the ^{12}C$(\alpha,\gamma)^{16}$O reaction rate the CF88.**

the solar chemical composition.

In addition to these efforts made to constrain "observationally", this rate, there are also a number of papers devoted to the analysis of the dependence of the evolutionary properties of the stars on this rate. In particular there are some in which it has been tested directly the influence of this rate on the central He burning phase: in order to understand how different choices for this rate could alter the predicted properties of cepheids stars, [55, 54, 16] found that the extension of the blue loop in the HR diagram was a function of this rate and hence that it could influence the expected

96

Figure 4.6: **Complete track set in** $Log(t_c) \div Log(\rho_c)$ **plane for the computed models using for the value of the** $^{12}\mathrm{C}(\alpha,\gamma)^{16}\mathrm{O}$ **reaction rate the CF85.**

range of masses capable of entering the instability strip. At variance with these findings [76] and [110] noticed that the $^{12}C(\alpha,\gamma)^{16}O$ does not affect the the path of a star in the HR diagram. For sake of completeness we want to remind that it has also been studied the properties of the cooling sequences of the WDs as a function of this rate.

The main motivation for this work borns from the simple consideration that the $^{12}C(\alpha,\gamma)^{16}O$ reaction occurs in a convective environment and, hence, an analysis of its influence on the evolution of a star cannot be disentangled by the behavior of

the convective core. Indeed, the final carbon and oxygen abundances left by the He burning largely depends on a delicate balance between the efficiency of this rate and the treatment of the convective instabilities. This means that, in general, there is no hope to confine the efficiency of this rate on "observable" data. The only thing which may be constrained is the C (O) abundance left by the He burning and not the rate. The, unfortunately, largely radicated idea that paper [109] strongly favors a rate 1.7 times the value of Caughlan & Fowler compilation of 1988 [26] (CF88) is unsubstantiated.

The famous figure in the cited paper [109], so as the whole paper, must be interpreted as a support for a C abundance left by the He burning of the order of $X_{12_C} \geq 0.2$, i.e. the value obtained by Woosley and Weaver by adopting their scheme of mixing and the CF88 rate times 1.7.

A further occurrence which enhances the influence of this process on the evolution of a star is that it is not the dominant one in the central He burning but a sort of "side" process. In fact, it must be reminded that in all phases in which the nuclear energy production is mainly controlled by the mass of the star (i.e. the central H and He burnings phases) even large changes in the cross section of a dominant process are easily managed by the star which counterbalances this changing by an opposite and small change in the temperature: for example, an increase of the cross section of the $^{14}N(p, \gamma)^{15}O$ reaction by an order of magnitude does not change AT ALL the MS lifetime of a star fully supported by the CNO cycle. On the contrary, if the efficiency of a process is not controlled by the star itself (which occurs if it is a "side" process or, alternatively, if the star is not in the central H or He burning phase) any changing of its cross section fully reflects on the evolution of the star.

4.2.1 The models

We followed the evolution of stellar model having Z=0.02 (Y=0.285 and $2.5 \leq M/M_\odot \leq 25$) from the MS up to the central He exhaustion. We also followed the central He burning phase of a "typical" HB star, i.e. a star having an He core mass
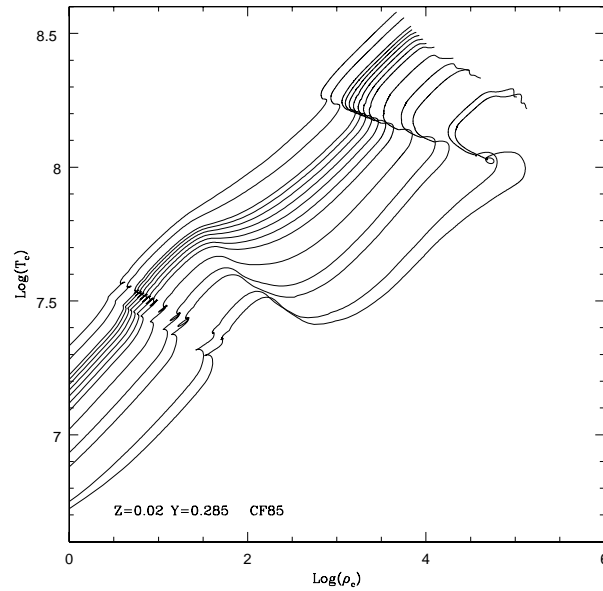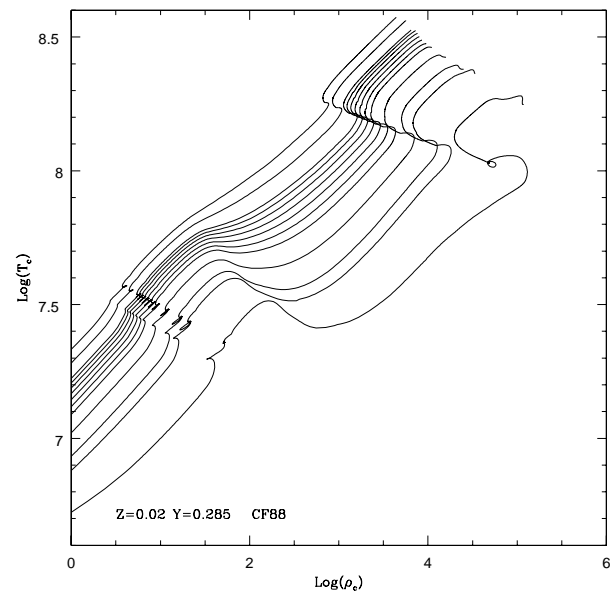
Figure 4.7: **Complete track set in** $Log(t_c) \div Log(\rho_c)$ **plane for the computed models using for the value of the** ^{12}**C**$(\alpha, \gamma)^{16}$**O reaction rate the CF88.**

of 0.485 $M_\odot$, a total mass of 0.6 $M_\odot$, an initial He abundance Y=0.23 and metallicity Z=0.001. All these evolutions have been computed twice, once by adopting the CF88 [26] rate and once the CF85 [25] one for the $^{12}C(\alpha,\gamma)^{16}O$ reaction rate.

Table 4.1 summarizes for each mass the main evolutionary properties (each couple of columns refers to values obtained with the CF88 and the CF85 rates, respectively). In order, left to right we report: the central He burning lifetime, the Carbon and Oxygen abundances left by the He burning, the time spent by each model in the blue loop (i.e. at $Log(T_{eff} \geq 3.80)$, the fraction of the He burning lifetime spent in the blue loop, the He core mass at the He ignition, the maximum size of the convective core and the final He core mass at the He exhaustion.

Figs. 4.4 to 4.13 summarize graphically the net effect of a changing of the $^{12}C(\alpha,\gamma)^{16}O$ reaction rate from the CF88 to the CF85 one on the central He burning phase. In particular: fig. 4.4, 4.5, 4.6, 4.7 show the complete set of models calculated in the HR diagram and $Log(t_c) \div Log(\rho_c)$ plane respectively; fig. 4.8, 4.9 and 4.10 show the path followed by intermediate masses, massive and HB calculated models in the HR diagram (the solid and dashed lines refer, respectively, to models computed with the CF85 and CF88 rate), fig. 4.11 shows, as filled dots, the difference in the He burning lifetimes (in percent) obtained for the two rates as a function of the initial mass while 4.12 shows the fractional time of helium burning (in percent) spent in the blue loop (the filled and open dots refer, respectively, to models computed with the CF88 and CF85 rate).

All these figures show that an uncertainty of the $^{12}C(\alpha,\gamma)^{16}O$ within the quoted range does not alter dramatically the "observable" properties of a star in the central He burning phase. In particular, the path followed by these stars in the HR diagram is practically unaffected while the He burning lifetime is altered by 10% at most so as the percentage of time spent by a star in the blue loop. Note that the largest mass experiencing a blue loop depends (even if mildly) on the $^{12}C(\alpha,\gamma)^{16}O$ since it shifts from the 14 to 15 $M/M_\odot$.

Table 4.1: Table summarizes for each mass the main evolutionary properties. Each couple of columns refers to values obtained with the CF88 and the CF85 rates, respectively; in order, left to right we report: the central He burning lifetime, the Carbon and Oxygen abundances left by the He burning, the time spent by each model in the blue loop (i.e. at $Log(T_{eff}) \geq 3.80$), the fraction of the He burning lifetime spent in the blue loop, the He core mass at the He ignition, the maximum size of the convective core and the final He core mass at the He exhaustion.

M (M☉)	t_{He} (Myr)		X_{12C}		X_{16O}		t_B (Myr)		$\%t_B/t_{He}$		M^{in}_{CHe} (M☉)	M_{CC} (M☉)		M^2_{CHe} (M☉)	
	88	85	88	85	88	85	88	85	88	85		88	85	88	85
0.8	100	110	0.495	0.294	0.505	0.786	0.00	0.00	0	0	0.48	0.200	0.220	0.50	0.50
2.5	219	231	0.451	0.195	0.530	0.761	0.00	0.00	0	0	0.33	0.200	0.210	0.50	0.51
3	124	134	0.493	0.221	0.489	0.691	0.00	0.00	0	0	0.38	0.223	0.224	0.55	0.56
5	18.9	20.7	0.556	0.290	0.425	0.688	0.00	5.76	0	0	0.64	0.433	0.452	1.03	1.05
6	10.9	11.7	0.541	0.294	0.440	0.711	4.88	2.99	45	49	0.80	0.552	0.571	1.31	1.34
8	4.98	5.45	0.524	0.270	0.457	0.736	2.50	1.66	50	55	1.16	0.818	0.878	1.90	1.94
10	2.87	3.15	0.501	0.245	0.480	0.744	1.37	0.97	47	53	1.58	1.152	1.231	2.52	2.58
12	1.88	2.07	0.490	0.237	0.492	0.752	0.76	0.57	40	47	2.08	1.555	1.576	3.19	3.25
14	1.36	1.50	0.482	0.229	0.499	0.751	0.33	0.37	24	38	2.65	2.006	2.126	3.89	3.97
15	1.20	1.31	0.480	0.230	0.501	0.765	0.00	0.00	0	29	2.96	2.271	2.362	4.17	4.33
20	0.76	0.83	0.453	0.216	0.527	0.794	0.00	0.00	0	0	4.66	3.890	4.041	6.33	6.33
25	0.58	0.64	0.417	0.184	0.562	0.562	0.00	0.00	0	0	6.63	5.862	6.000	8.68	8.68

Figure 4.8: **Path followed by the 0.8M$_\odot$ model in the HR diagram: the solid and dotted lines represent the evolutions obtained by adopting, respectively, the CF85 and CF88 rates of the ^{12}C$(\alpha,\gamma)^{16}$O.**

Figure 4.9: **Path followed by the 2.5M$_\odot$, 5M$_\odot$ and 8M$_\odot$ models in the HR diagram: the solid and dotted lines represent the evolutions obtained by adopting, respectively, the CF85 and CF88 rates of the ^{12}C$(\alpha,\gamma)^{16}$O.**

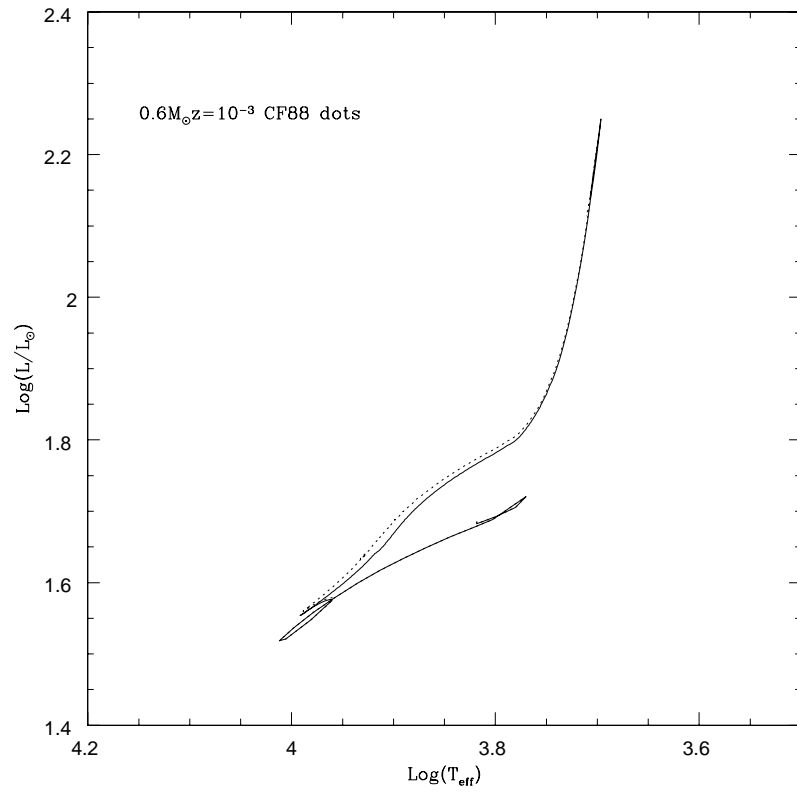Figure 4.10: **Path followed by the $10M_\odot$, $15M_\odot$ and $25M_\odot$ models in the HR diagram: the solid and dotted lines represent the evolutions obtained by adopting, respectively, the CF85 and CF88 rates of the $^{12}C(\alpha,\gamma)^{16}O$.**
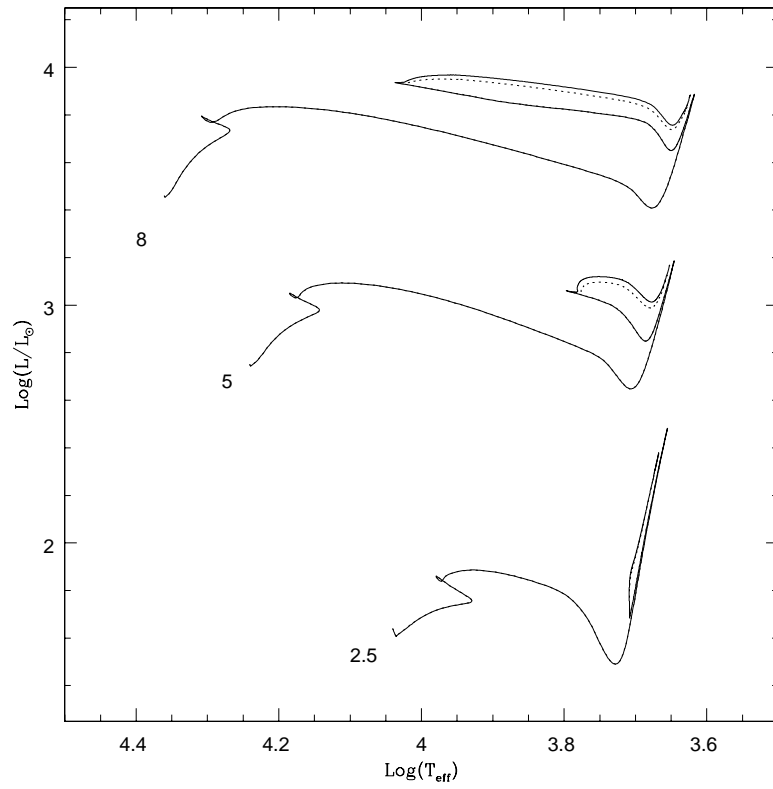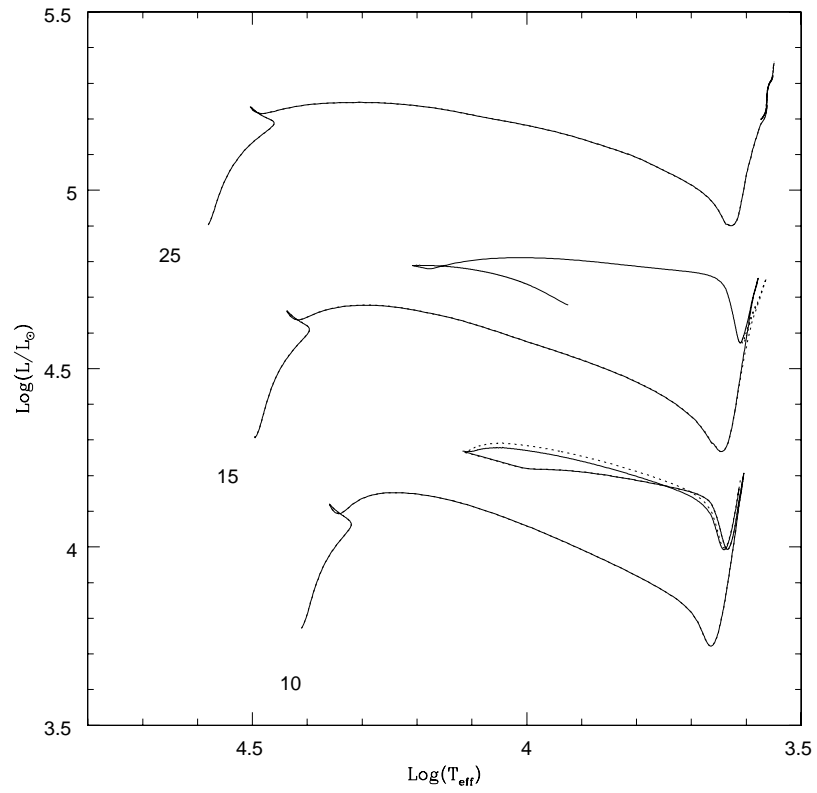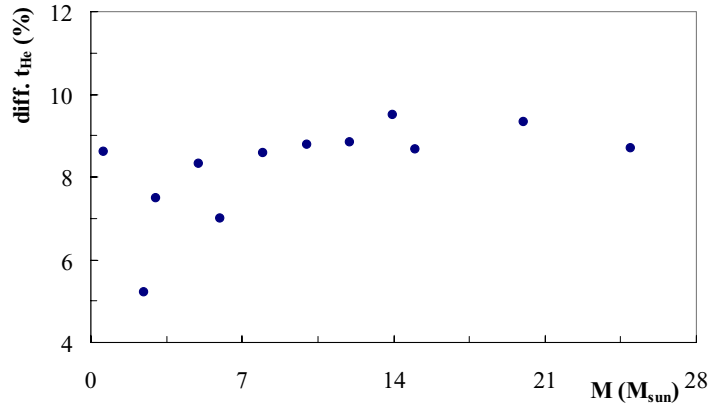
Figure 4.11: **The figure shows the difference in the He burning lifetimes (in percent) obtained for the two rates as a function of the initial mass.**

In addition to the direct influence of the $^{12}C(\alpha,\gamma)^{16}O$ on the "observable" properties of a star, it is of crucial importance to investigate the dependence of the chemical composition left by the He burning as a function of the $^{12}C(\alpha,\gamma)^{16}O$, i.e. the C and O abundances since it will influence all the further evolution of a star. Fig. 4.13 shows the amount of carbon left by the He burning as a function of the initial mass.

The filled symbols refer always to computations performed by adopting the CF88 value while the open symbols always refer to models computed by adopting the CF85 value; the dots refer to our "standard" models. The first thing worth noting is that the two sets of models show essentially the same dependence of the final C abundance on the initial mass and hence that they are more or less systematically shifted one respect to the other by 0.20:0.25 dex.

The general trend is that the C abundance left by the He burning increases moving from the largest He core masses towards the smaller ones, then a maximum is reached for a mass of the order of 5 $M_\odot$ and then a drop occurs for smaller values of the
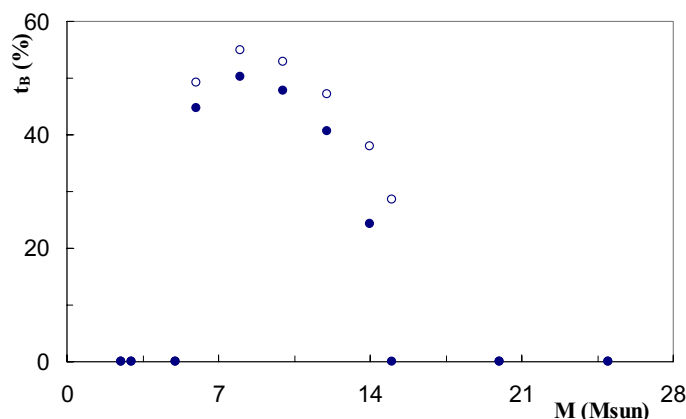
Figure 4.12: **The figure shows the fractional time of helium burning (in percent) spent in the blue loop. The filled and open dots refer, respectively, to models computed with the CF88 and CF85 rate for the ^{12}C$(\alpha, \gamma)^{16}$O reaction.**

mass; the HB star (shown as a triangle) closely behaves like the 3 $M_\odot$. However the maximum excursion of the C abundance is confined within 0.15 dex over the full mass range here analyzed, and this excursion even reduces to 0.1 dex for the masses larger than, say, 8 $M_\odot$. The existence of this trend with the initial mass may be understood by reminding that, for any given temperature, the lower the mass the larger the density (see figs. 4.6 and 4.6): since the rate of the 3α depends on the square of the density while the rate of the $^{12}C(\alpha, \gamma)^{16}O$ depends only linearly on the density, a smaller mass favors the carbon production with respect to its destruction. It is important to underline here that this trend holds only because all these stars share the **same** behavior of the convective cores (see below). In fact the onset of a turnover in the final C abundance when the initial mass drops below 5 solar masses is due to the appearance of a semiconvective region at the border of the convective core, phenomenon which enhances the conversion of C in O.

Since the process we are dealing with occurs in a convective environment it is now

Figure 4.13: **The figure shows the amount of carbon left by the He burning as a function of the initial mass. The filled symbols refer to computations performed by adopting the CF88 value while the open ones refer to models computed by adopting the CF85 value.**
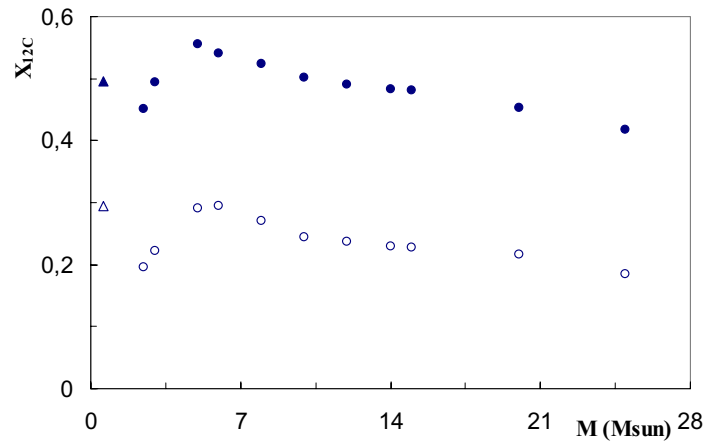
important to verify if, and at what extent, the present results depend on the adopted convective scenario: in particular we recomputed the central He burning of a selected subset of the tracks by including, this time, an amount of mechanical overshooting equal to 1 H_p. In spite of a much larger (mass) size of the convective core the final C abundance (shown as triangles in fig. 4.14) closely resemble the one obtained in the standard case all over the mass range explored here. This is **not** a surprising result because a simple changing of the size of the convective core does not alter appreciably the run of neither the central temperature nor the density versus the He abundance (see fig. 4.15), and hence the rate at which He in converted in C, and the C in O, is not significantly modified. The only thing which changes in these tests is the total burning time because the available "reservoir" grows with the size of the convective core.

The "mechanical" overshooting, however, is not the only phenomenon which may affect the central He burning. How we have already stated before, all the present "standard" models have been obtained by inhibiting the possible occurrence of the Breathing Pulses. If we release such a condition and allow the convective core to behave freely we obtain the results shown in fig.x as squares: in this case all the masses in which the BP phenomenon occurs show a central C abundance much smaller than in the standard case. The reason is that this kind of mixing deeply alters the behavior of the He burning since, instead of a simple rescaling, we face now a situation in which fresh He is brought in the center of these stars when there is already a large abundance of C and a low abundance of He: this situation speeds up and increases the conversion of C in O. How it is evident from fig. 4.14, since the occurrence of the BP depends on the initial mass, the changing of the final C abundance with respect to the standard case depends on the initial mass. Above the 15 $M_\odot$ the BP phenomenon does not occur and hence the final C abundance remains unaffected above this threshold value. As a final comment on this scenario let us underline that the inclusion of the BP phenomenon tends to flatten out the dependence of the C abundance on the initial mass. Of course a similar result would be obtained by

108
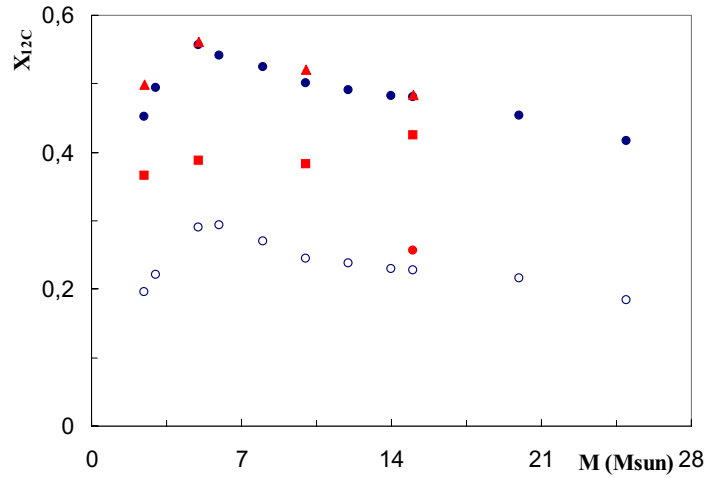
Figure 4.14: **The figure shows, overposed to our "standard" models, the amount of carbon left by the He burning as a function of the initial mass for computed models adopting a mechanical overshooting equal to 1 H_p (red triangle) and models without inhibiting the possible occurrence of the Breathing Pulses (red squares), always considering the CF88 reaction rate. Moreover, the red dot is refered to a numerical teststand for a 15 solar masses in which just 0.1 hp of mechanical overshooting is allowed when the central He burning drops below 0.075 by mass fraction, again it used the CF88 rate.**
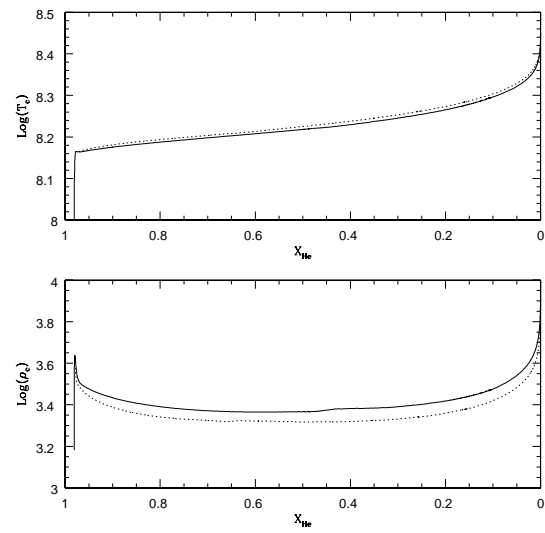
Figure 4.15: **Central temperature (upper panel) and density (lower panel) as a function of central abundance of helium. The filled line refers to CF88 standard model, while the dotted one to the model of 1 Hp overshooting.**

adopting the CF85 rate.

Once again, these are not the only two possible "convective" scenarios. Another possibility could come from the adoption of the Ledoux criterion coupled to a specific (and arbitrary) treatment of the region in which the radiative stability is granted only by the existence of a gradient of molecular weight. Just as a last "numerical" example we show, as a red dot in fig. 4.14, the C abundance left by the He burning of a 15 solar masses in which just 0.1 hp of mechanical overshooting is allowed when the central He burning drops below 0.075 by mass fraction: in this case the final C abundance closely resembles the value obtained by adopting the CF85 rate.

We conclude that the details of the mixing technique adopted to treat the mixing in the last part of the central He burning may affect (also drastically) the final Carbon and Oxygen abundances. Hence a better experimental knowledge of $^{12}C(\alpha, \gamma)^{16}O$ cross section will also help to shed light on the efficiency of the convective instabilities which may or may not occur during the latest phases of the He burning. It is worth stressing again that trying to gain information about this nuclear cross section using astrophysical constrains is vanished by the uncertainty in the convection treatment and the only thing which may be constrained is the C (O) abundance left by the He burning and not the rate.

4.3   The advanced evolutionary phases of a 25M$_\odot$

In the previous section we showed the direct influence of the $^{12}C(\alpha, \gamma)^{16}O$ process on the central He burning of stars in a wide mass interval together with its interplay with the treatment of the convective core. The next logical step would be to follow the further evolution of all these stars in order to determine the final impact of this process on stars of different masses. Such a big project goes beyond the purposes of the present work: in this section we will concentrate on the further evolution of the 25 $M_\odot$ (taken as representative of the massive stars) up to the final collapse and explosion. The carbon abundance left by the He burning is $X_C^{cent} = 0.4$ for the

CF88 rate and $X_C^{cent} = 0.2$ for the CF85 one. Let us stress once again that all the evolutionary properties we will discuss below depend directly on the C abundance left by the He burning and not on the $^{12}C(\alpha, \gamma)^{16}O$ reaction rate adopted. This is an important point to underline because, how we have already discussed above, the same C abundance (and hence the same evolutionary properties) may be obtained by different choices of this rate and of the treatment of convection. For this reason we will refer to these test tracks as **C4** (CF88 rate) and **C2** (CF85 rate).

The main evolutionary properties of these two evolutions are summarized in table 4.2 and in figs. 4.16 and 4.22. Table 4.2 reports, for each central burning, its lifetime, the size of the convective core, the abundance of the most abundant elements produced in the burning so as the data relative to the convective shell episodes, if present. In particular we report: for the hydrogen burning we report the time (τ_H) and maximum mass of hydrogen convective core (M_{CC}); for the helium burning the time between the end of hydrogen burning and the beginning of helium burning(Δ t(H-exh.He-ign.)), the time of helium burning (τ_{He}), maximum mass of helium convective core (M_{CC}), the life time of the helium convective shell ($\Delta t_{He\ conv\ shell}$), the maximum mass size of the helium shell ($\Delta M_{He\ conv\ shell}$) and the abundance of ^{12}C and ^{16}O at the end of the burning; for the carbon burning the time between the end of helium burning and the beginning of carbon burning(Δt(He-exh.C-ign.)), the time of carbon burning (τ_C), maximum mass of carbon convective core (M_{CC}), the life time of the carbon convective shells ($\Delta t_{1-2C\ conv\ shell}$), the maximum mass size of the helium shells ($\Delta M_{1-2He\ conv\ shell}$) and the abundance of ^{16}O, ^{20}Ne and ^{24}Mg at the end of the burning; for the neon burning the time of the burning (τ_{Ne}), maximum mass of neon convective core (M_{CC}) and the abundance of ^{16}O, ^{24}Mg and ^{28}Si at the end of the burning; for the oxygen burning the time of the burning (τ_O), maximum mass of neon convective core (M_{CC}) and the abundance of ^{28}Si, ^{32}S and ^{34}S at the end of the burning; for the silicon burning the time of the burning (τ_{Si}), maximum mass of neon convective core (M_{CC}) and the abundance of ^{56}Fe and ^{60}Ni at the end of the burning.

Table 4.2: **Final stages of** $25 M_\odot$ **star.**

	CF88	CF85
H Burning		
$\tau_H(yr)$	5.81(6)	5.81(6)
$M_{CC}(M_\odot)$	12.7	12.7
He Burning		
Δt(H-exh.He-ign.)	2.70(4)	2.70(4)
$\tau_H e(yr)$	5.8(5)	6.37(5)
$M_{CC}(M_\odot)$	5.6	5.8
$\Delta t_{He\ conv\ shell}$(yr)	1.6(4)	1.5(4)
$\Delta M_{He\ conv\ shell}(M_\odot)$	2.1	2.2
^{12}C	0.424	0.200
^{16}O	0.546	0.769
C Burning		
Δt(He-exh.C-ign.)	1.17(4)	1.03(4)
$\tau_C(yr)$	5.76(3)	4.56(3)
$M_{CC}(M_\odot)$	0.5	
$\Delta t_{1C\ conv\ shell}$(yr)	91	1
$\Delta M_{1C\ conv\ shell}(M_\odot)$	1	1.2
$\Delta t_{2C\ conv\ shell}$(yr)	40	0.2
$\Delta M_{2C\ conv\ shell}(M_\odot)$	3	2.4
^{16}O	0.378	0.674
^{20}Ne	0.478	0.260
^{24}Mg	0.014	0.076
Ne Burning		
$\tau_N e(yr)$	37.9	6.01
$M_{CC}(M_\odot)$	0.56	0.77
^{16}O	0.632	0.810
^{24}Mg	0.139	0.072
^{28}Si	0.143	0.071
O Burning		
$\tau_O(yr)$	1.62	0.274
$M_{CC}(M_\odot)$	1.26	0.98
^{28}Si	0.561	0.604
^{32}S	0.014	0.008
^{34}S	0.336	0.150
Si Burning		
$\tau_S i(yr)$	0.21	0.0167
$M_{CC}(M_\odot)$	0.95	1.28
^{56}Fe	0.507	0.674
^{60}Ni	0.007	0.023
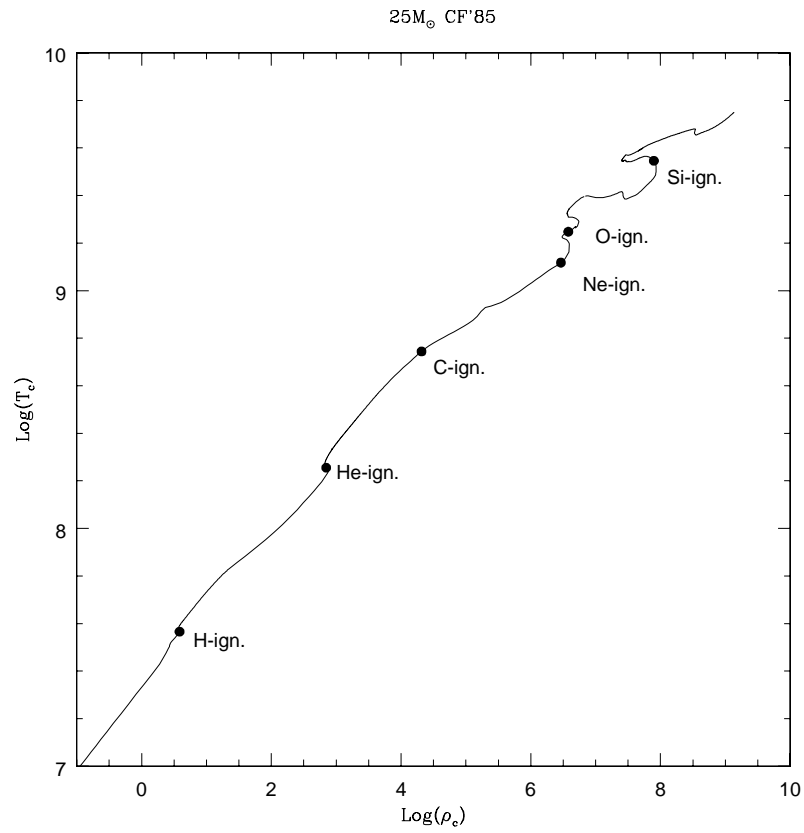
Figure 4.16: **Path followed by the 25M$_\odot$ model in the** $Log(t_c) \div Log(\rho_c)$ **plane adopting the CF85 rates of the** ^{12}**C**$(\alpha, \gamma)^{16}$**O.**
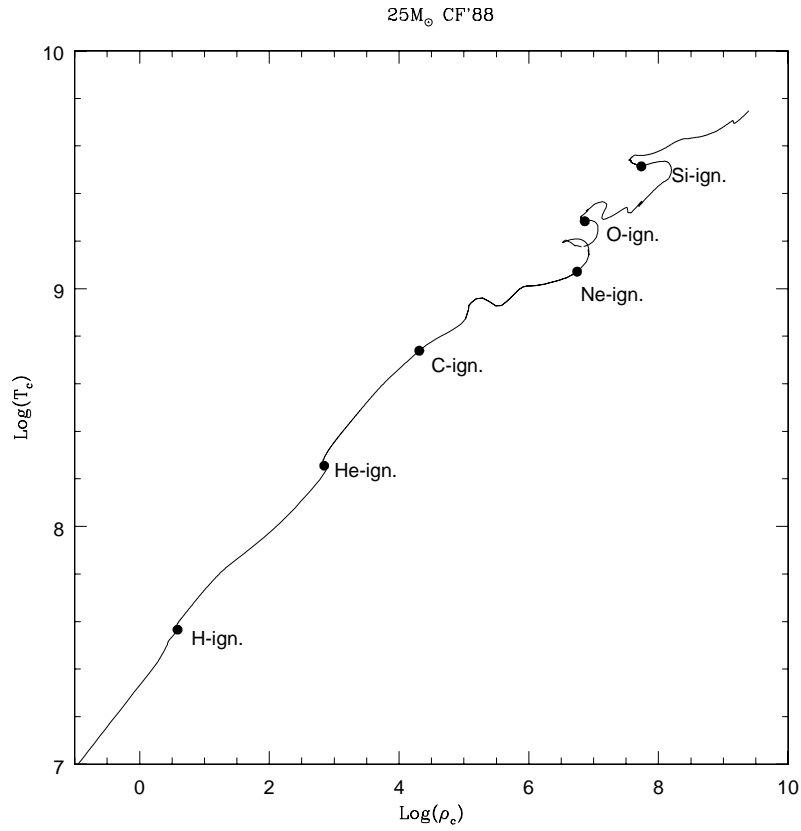
Figure 4.17: **Path followed by the 25M$_\odot$ model in the** $Log(t_c) \div Log(\rho_c)$ **plane adopting the CF88 rates of the** ^{12}**C**$(\alpha, \gamma)^{16}$**O.**
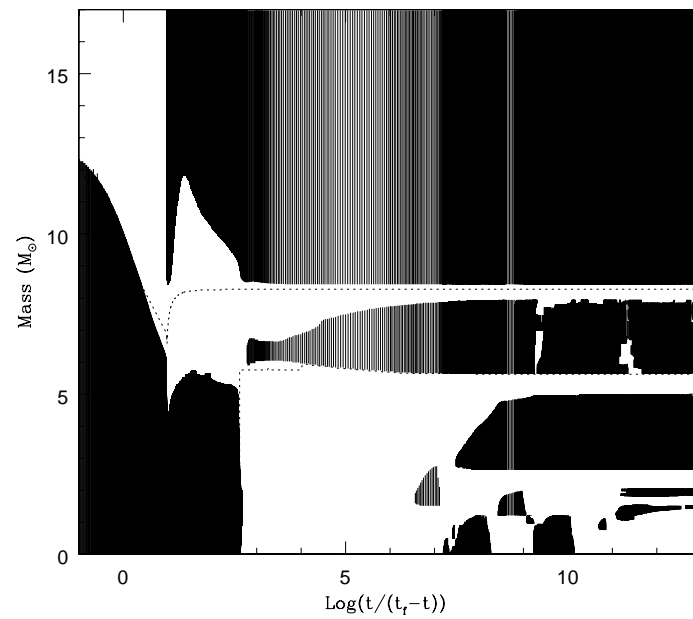
Figure 4.18: **Temporal evolution of the convective regions (*solid lines*) and of the nuclear burning shells (*dotted lines*) for the C2 model.**
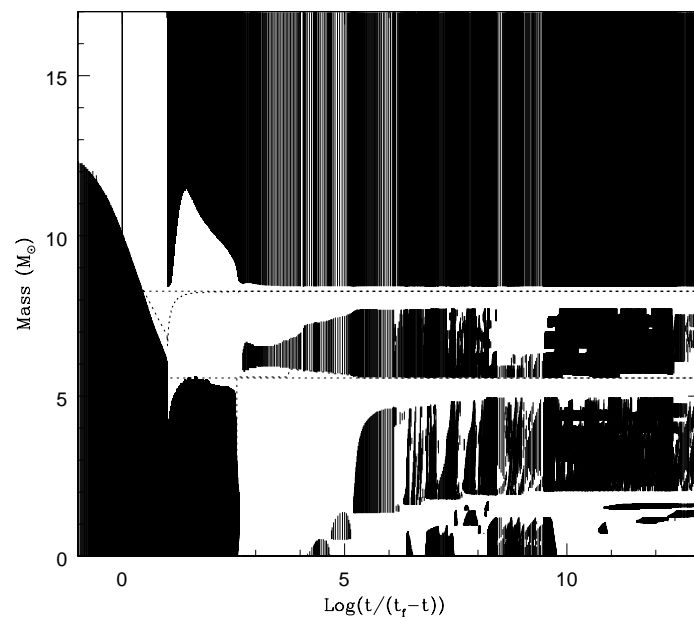
Figure 4.19: **Temporal evolution of the convective regions (*solid lines*) and of the nuclear burning shells (*dotted lines*) for the C4 model.**

Figs. 4.16 and 4.17 shows the path followed by the two stars in the $Log(t_c) \div$ $Log(\rho_c)$ plane while figs. 4.18 and 4.19 shows the behavior of the convective regions as a function of time. These two figures summarize the temporal evolution of the two stellar models up to the moment of the core collapse while a snapshot of the final structure at the moment of the explosion is shown in figs. 4.20 and 4.22: the first of the two shows the internal run of the most abundant elements while fig. 4.22 shows the final mass-radius relation together to the final Ye distribution. We will not discuss in details the properties of the various burnings and we refer the reader to [27, 70] for a detailed analysis of the advanced burnings; here we want to underline the key changings in the evolutionary properties due to a changing of the C abundance present in the He exhausted core.

The first thing we want to note is that the region outside the Carbon Oxygen core, i.e. the He and H rich layers, is not influenced by the Carbon abundance left by the He burning: the reason is obviously that the typical timescale on which this outer region may evolve is much longer than the lifetime of all the advanced burning phases put together. The carbon burning, on the contrary, differs deeply in the two runs. Since, how it is well known, the neutrino losses begin to become a very efficient energy sink then the formation of a convective core requires the nuclear energy to overcome the neutrino losses. The main process in the carbon burning is $^{12}C(^{12}C,\alpha)^{20}Ne$, therefore the energy rate depends quadratically on the C abundance. Thus, it is clear that a convective core may form only if the carbon abundance is sufficiently large. In our case it happens that the **C4** run can form a convective core while the **C2** run burns carbon in a radiative environment. Once the ^{12}C is exhausted in the center, however, in both cases the further evolution of the carbon shell is characterized by the formation of successive convective episodes. In spite of the very different amount of fuel available, the final C convective shell shows some conspicuous similarities: in particular the outer border of the convective shell is essentially insensible to C_{ini} since because it is fixed by the location of the He shell (which is the same in the two cases) while the inner one is mildly dependent on C_{ini} because a lower C abundance allows a faster
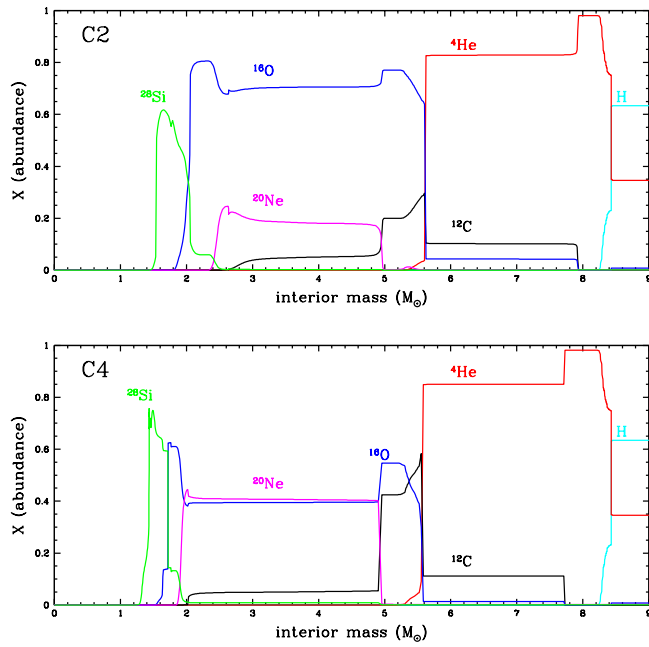
Figure 4.20: **Final structures of the two models: the internal run of the most abundant elements for C2 model (upper panel) and C4 model (lower panel).**

advancing of the burning shell (which marks the base of the convective shell). Roughly speaking, the size of the convective shell reduces by almost the 20% by mass fraction by changing the C abundance from 0.4 down to 0.2 dex. Moreover, in both cases the C present in this last convective shell episode is almost completely burned out. These similarities imply that the final chemical composition (both relative and absolute) present in this shell largely depends on C_{ini}. The reason is obviously that, since the C is almost completely destroyed in both cases, the abundances of the elements coming directly from this burning will totally depend on the initial abundance of C. These elements are: Ne, Na, Mg, Al, P and Cl. In particular Ne and Mg are the ones which are more directly linked to the C abundance (see section 4.3). The further evolution of these two models reflects the fact that the presence of a very efficient convective shell in the **C4** run slows down the contraction of the part of the CO-core which lies outside the base of the C-burning shell. To clarify this situation fig. 4.21 lower panel shows, for the **C4** case, the mass-radius relation at various stages starting from the end of central Carbon burning (black line) up to the moment of the collapse (green line). It is rather evident that the changing in the shape which forms at a mass coordinate of 1.2 $M_\odot$ is due to the formation of an extended and very efficient convective shell: this occurrence creates a decoupling in the behavior of the star in the sense that it slows down the contraction of the outer part of the CO core. Upper panel of fig. 4.21 shows the same data but for the **C2** run. In this case the carbon abundance is low enough that the Carbon shell is not able anyway to slow down the contraction of the outer regions and the relation M-R remains essentially linear until the latest phases of contraction.

The final M-R relation (fig. 4.22) shows that the **C4** run produces a less compact structure with respect to the **C2** run. This means that the global amount of matter which will be subject to the explosive burnings will be smaller in the **C4** case with respect to the **C2**. Anyway by allowing the formation of a shock wave corresponding to an initial energy of $1.2 \cdot 10^{51}$ erg in the mantle of the two stellar models one can compute the final chemical composition which will be returned to the interstellar

Table 4.3: **Total amount of each element spread in the interstellar medium and the percent difference, for each element, between the two cases: the total mass ejected is** 23.08 $M_\odot$ **for C4 and** 22.57 $M_\odot$ **for C2.**

	CF88	CF85	%
	$M_\odot$	$M_\odot$	
H	$1.04 \cdot 10^{+01}$	$1.04 \cdot 10^{+01}$	0.0
He	$8.14 \cdot 10^{+00}$	$8.02 \cdot 10^{+00}$	1.4
C	$6.85 \cdot 10^{-01}$	$5.06 \cdot 10^{-01}$	35.4
N	$8.11 \cdot 10^{-02}$	$7.88 \cdot 10^{-02}$	3.0
O	$1.71 \cdot 10^{+00}$	$2.39 \cdot 10^{+00}$	-28.3
F	$1.09 \cdot 10^{-05}$	$1.27 \cdot 10^{-05}$	-14.1
Ne	$1.08 \cdot 10^{+00}$	$4.14 \cdot 10^{+01}$	159.6
Na	$3.23 \cdot 10^{-02}$	$1.60 \cdot 10^{-02}$	102.3
Mg	$3.60 \cdot 10^{-01}$	$1.25 \cdot 10^{-01}$	188.3
Al	$3.20 \cdot 10^{-02}$	$1.26 \cdot 10^{-02}$	154.5
Si	$2.02 \cdot 10^{-01}$	$2.22 \cdot 10^{-01}$	-8.9
P	$2.20 \cdot 10^{-03}$	$1.78 \cdot 10^{-03}$	23.6
S	$7.77 \cdot 10^{-02}$	$1.13 \cdot 10^{-01}$	-31.4
Cl	$4.53 \cdot 10^{-04}$	$4.36 \cdot 10^{-04}$	3.8
Ar	$1.17 \cdot 10^{-02}$	$1.94 \cdot 10^{-02}$	-40.0
K	$1.80 \cdot 10^{-04}$	$2.32 \cdot 10^{-04}$	-22.4
Ca	$6.94 \cdot 10^{-03}$	$1.31 \cdot 10^{-02}$	-47.0
Sc	$3.31 \cdot 10^{-06}$	$4.51 \cdot 10^{-06}$	-26.8
Ti	$1.75 \cdot 10^{-04}$	$2.33 \cdot 10^{-04}$	-25.0
V	$2.25 \cdot 10^{-05}$	$3.05 \cdot 10^{-05}$	-26.3
Cr	$1.78 \cdot 10^{-03}$	$2.96 \cdot 10^{-03}$	-40.0
Mn	$8.79 \cdot 10^{-04}$	$1.22 \cdot 10^{-03}$	-27.8
Fe	$8.73 \cdot 10^{-02}$	$9.05 \cdot 10^{-02}$	-3.6
Co	$6.48 \cdot 10^{-04}$	$4.49 \cdot 10^{-04}$	44.1
Ni	$5.71 \cdot 10^{-03}$	$4.36 \cdot 10^{-03}$	31.1
Cu	$4.45 \cdot 10^{-04}$	$4.05 \cdot 10^{-04}$	9.9
Zn	$1.13 \cdot 10^{-03}$	$7.54 \cdot 10^{-04}$	50.5
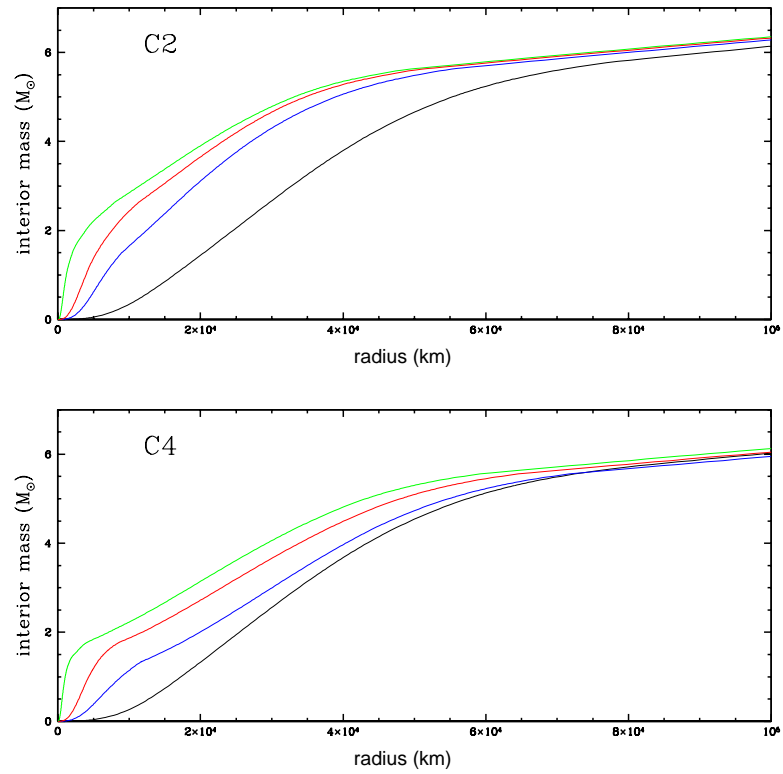
Figure 4.21: **The figure shows the mass-radius relation at various stages starting from the end of central Carbon burning (black line) up to the moment of the collapse (green line).**
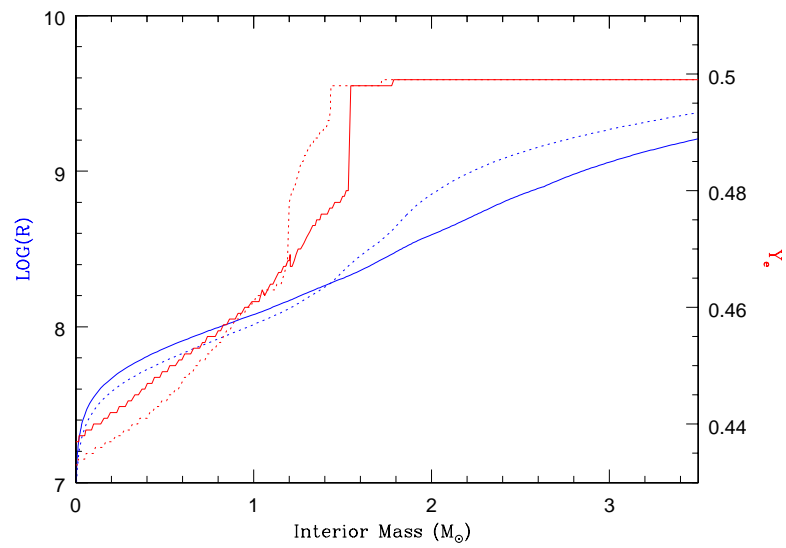
Figure 4.22: **The figure shows the final mass-radius relation (blue-lne) together to the final Ye distribution (red line).**
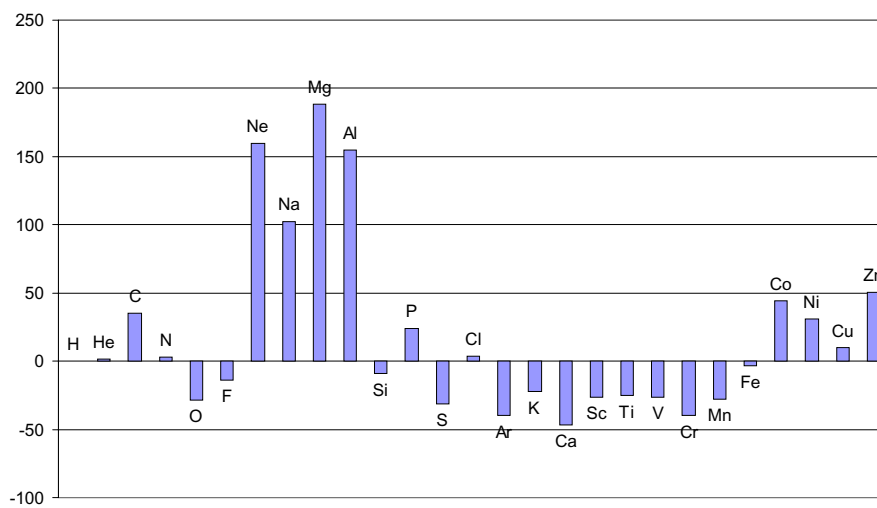
Figure 4.23: **The figure shows the percent difference between C4 and C2 ejected yields.**

medium. Table 4.3 and fig. 4.23 show a comparison between the yields produced in the two cases.

In table 4.3 we report the total amount of each element spread in the interstellar medium and the percent difference, for each element, between the two cases. The total mass ejected is 23.08 $M_\odot$ for **C4** and 22.57 $M_\odot$ for **C2**, this means that the contracting neutron star, resulting after the explosion, will have a larger mass in the **C4** case. Since the **C4** model has a double amount of carbon than the **C2** one, then the ejected matter has a larger (35.4%) amount of carbon so as other nuclei produced in the carbon burning; in particular Neon, Sodium, Magnesium, Alluminium, and less Phosphorous and Chlorine. On the contrary, the **C2** model ejects more Oxygen (28.3%) and so, also, more Silicon, Sulphur, Argon, Potassium, Calcium, Scandium, Titanium, Vanadium, Chromium and Manganese, since they are the main product

of the explosive oxygen burning. Note that the difference in Si amount is lower than the other nuclei, since a more abundant Ne, in the **C4**, produces more silicon in its burning. In figure 4.23 we show the details of the difference in ejected yields.

In conclusion of this section it worth noting that, whatever is the responsible, the $^{12}C(\alpha,\gamma)^{16}O$ reaction rate or the convective treatment, at the moment we have large uncertainty in the C (O) abundance at the end of helium burning. This uncertainty directly reflects on the expected final yields. Again, a better knowledge of the $^{12}C(\alpha,\gamma)^{16}O$ reaction rate could help in the choice between the two scenarios, since it would reduce the degrees of freedom of the problem.

4.4 The measurement of the cross section of the $^{12}\text{C}(\alpha,\gamma)^{16}\text{O}$ reaction

From an experimental point of view, despite the enormous efforts devoted to the measurement of this cross section, the corresponding rate at astrophysical energies is still now far from being well established. In the past twenty-five years many experiments have been performed, most of them based on the detection of γ-rays from α capture in direct or inverse kinematics [37, 83, 84, 79, 66, 77, 78, 90]. All these measurements extend to a minimum energy of about 1 MeV: below this energy, the extremely small value of the cross section ($< 10 \ pb$) hampers direct detection of γ-rays and extrapolation procedures (see section 2.3) have to be used in order to extract the astrophysical S-factor at the relevant energies ($E_0 = 300 \ keV$ for $T_9 = 0.18$). The cross section around the Gamow peak is dominated by four contributions: the E1 amplitudes due to the low-energy tail of the 1^- resonance at $E_{cm} = 2.42 \ MeV$ and to the subthreshold resonance at $-45 \ kev$, and the E2 amplitudes due to the 2^+ subthreshold resonance at $-245 \ keV$ and to the direct capture to the ^{16}O ground state, both with the corresponding interference terms (fig. 4.24).

For the purpose of the extrapolation, based on the fitting of differential cross sections in the investigated region, also the interference between the incoming partial
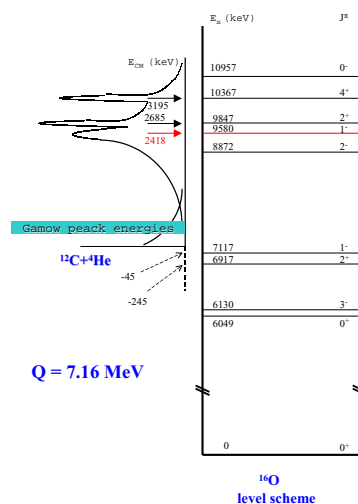
Figure 4.24: **Level scheme for ^{16}O with the corresponding excitation func- tion for $^{12}\mathbf{C}(\alpha, \gamma)^{16}\mathbf{O}$ reaction.**

waves contributing to the two multipoles has to be taken into account. Also, the decay to the first excited state has to be included, while a possible non radiative $0^+ \rightarrow 0^+$ decay should be considered. As far as a consistent description of the E1 interference terms, it should be noted that in order to constrain the phases of different amplitudes, data should be taken at energies well above the 1^- resonance, where the competition with the background arising from the $^{13}C(a, n)$ reaction (or other neutron-producing reactions in inverse kinematics studies) makes cross section measurements very difficult. Note that using all the available experimental points (fig. 4.25) the extrapolation does not foresee an unique picture. Indeed, using the R-matrix method ([46]) the choice between constructive and destructive interference is not unambiguous (fig. 4.26). In order to fix all the direct capture parameters in this extrapolation measurements at energies larger than 3 MeV are also needed.

The above arguments make the extrapolated values of S(300) very uncertain. A global analysis [17] of all available data (surface fit) including γ decay following α
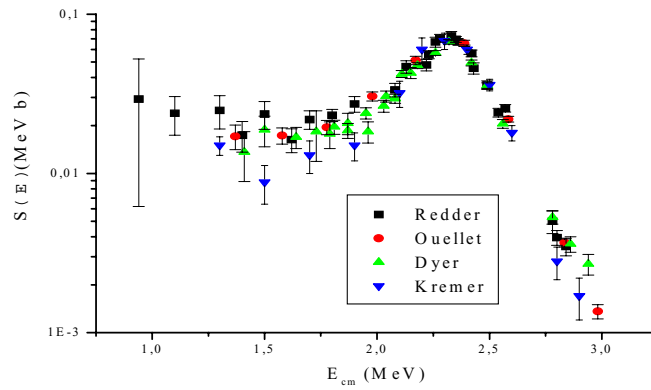
Figure 4.25: **Main experimental points for E1 component.**
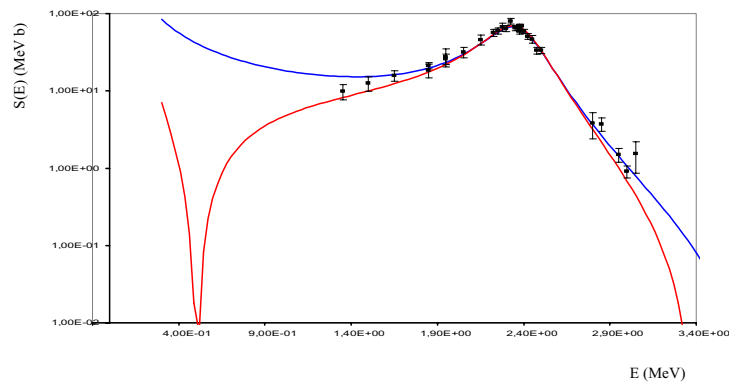
Figure 4.26: **The figure shows the two possible exptrapolation depending on the interefence between the resonances: constructive (blue line) and distructive (red line).**
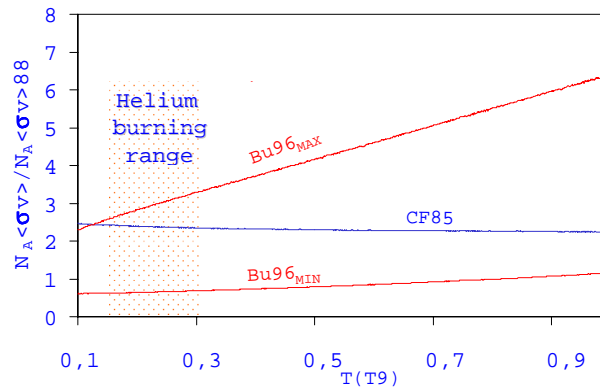
Figure 4.27: **Figure shows the ratio between the compilations of Fowler of 1985 (CF85) and of Buchmann (Bu96$_{max}$ and Bu96$_{min}$) and that of Fowler of 1988 (CF88) as a function of the temperature.**

capture from ^{12}C, elastic scattering of α particles from ^{12}C and α emission following β^- decay of ^{16}N [18, 6] and choosing the constructive picture for interference yielded a wide range (from 62 keV b to 270 keV b) for the extrapolated S-factor. These values, for $T_9 = 0.18$, correspond to a minimum and maximum reaction rates of $0.5 * 10^{-15}$ and $2.2 * 10^{-15} cm^3/(mol \cdot s)$, which can be compared to the data reported in the compilations of CF88 ($N_A\sigma v = 0.8 * 10^{-15} cm^3/(mol \cdot s)$) and CF85 ($N_A\sigma v = 1.9 * 10^{-15} cm^3/(mol \cdot s)$), which have been used in stellar evolution calculations described in previous sections. Finally, a recent compilation [3] yields $N_A\sigma v = 0.9*10^{-15} cm^3/(mol \cdot s)$ and $N_A\sigma v = 2.1 * 10^{-15} cm^3/(mol \cdot s)$ as lower and upper limit for the reaction rate.The adopted value is $N_A\sigma v = 1.5 * 10^{-15} cm^3/(mol \cdot s)$ (fig. 4.27).

4.4.1   The RMS method for ^{12}C$(\alpha, \gamma)^{16}$O reaction

The possibility to avoid systematic errors associated to the detection of γ-rays, is indicated by the use of the RMS method in the study of this reaction. Considerations similar to those used for the $^{7}Be(p, \gamma)^{8}B$, can be invoked to support the idea to measure the $^{12}C(\alpha, \gamma)^{16}O$ cross section in inverted kinematics with the Recoil Mass Separator method. The experimental requirements are, obviously, different, e.g. the kinematics of the reaction is deeply different. We can summarize in five points the peculiarities of the $^{12}C(\alpha, \gamma)^{16}O$ reaction which require an improvement of the apparatus for the measurement using inverted kinematics and RMS method:

1. **Angle acceptance -** at 1 MeV center of mass energy the angular dispersion is $\theta = 1.5°$. In an extended gas target, such as the one used for $^{7}Be(p, \gamma)^{8}B$, this opening angle would be too large to match the acceptance of collimators. Moreover the mechanical constrains of such a design would inhibit the location of the first focussing element close to the reaction region, so that the recoil beam size would require very large polar expansions. In order to minimize the beam dispersion the adopted solution was a **jet gas target**.

2. **Momentum acceptance -** at the same energy the momentum dispersion is $\Delta p/p = 5$ %. As we have seen the acceptance of the Naples Recoil Mass Separator is smaller. A new design of the layout of the separator is then necessary, in order to transport 100 % of ^{16}O recoils up to the telescope.

3. **Charge state choice -** at the energies of interest the ^{16}O recoil charge state distribution is peaked around values of q around 2 to 4, far below the minimum charge state not accessible to the ^{12}C beam. This hampers the use of this feature to help in the suppression of the leaky beam and additional dispersive elements have to be added to achieve the desired suppression factor.

4. **Beam purification -** the ^{12}C beam emerging from the accelerator is accompained by a contamination of ^{16}O ions with a continous energy spectrum (because

of charge exchange processes in the accelerator tubes) which, after the selection at the analysing magnet has the same magnatic rigidity of the beam, and then of the recoiling nuclei. These contaminants would be transported through the separator together with recoils and would then give rise to undistiguishable events in the final detector.

5. **Beam suppression factor -** the very small cross section at low energy implies a N_r/N_{el} ratio (section 2.4) of the order of 10^{-18}. This in turn requires a beam suppression of this order of magnitude.

For the above reasons, and since we need an intense beam - the cross section is of the order of 10^{-12} b -, we can not measure this reaction with the TTT-3 machine in Naples, while the Dynamitron Tandem of the Ruhr University has the necessary characteristics. The design and the implementation of an upgraded RMS at the DTL has then been undertaken three yers ago, and the installation is underway.

Recently the ERNA (European Recoil for Nuclear Astrophysics) collaboration has performed the first beam specification and purification test [86, 87]. Here we will briefly report the results of these test experiments. Fig. 4.28 shows schematically the 4 MV Dynamitron Tandem accelerator in Bochum together with the ERNA recoil separator elements.

In RMS approach, the reaction is initiated in inverted kinematics, $^4He(^{12}C,\gamma)^{16}O$, i.e. a ^{12}C ion beam is guided into a windowless ^4He jet gas target and the kinematically forward-directed ^{16}O recoils are detected downstream on the beam line. The direct observation of the ^{16}O recoils requires an efficient recoil separator to filter out the intense ^{12}C beam particles from the ^{16}O recoils (see the above point five): the number of ^{16}O recoils per incident ^{12}C projectile is $1 \cdot 10^{-18}$ for $\sigma = 1$ pb and a target density $n(^4He) = 1 \cdot 10^{18} atoms/cm^2$. The recoil separator must also filter out beam contaminants, small-angle elastic scattering cross section products, and background events from multiple scattering processes leading to a degraded tail of the projectiles. Reaching a beam suppression factor sufficiently high the ^{16}O recoils can be counted

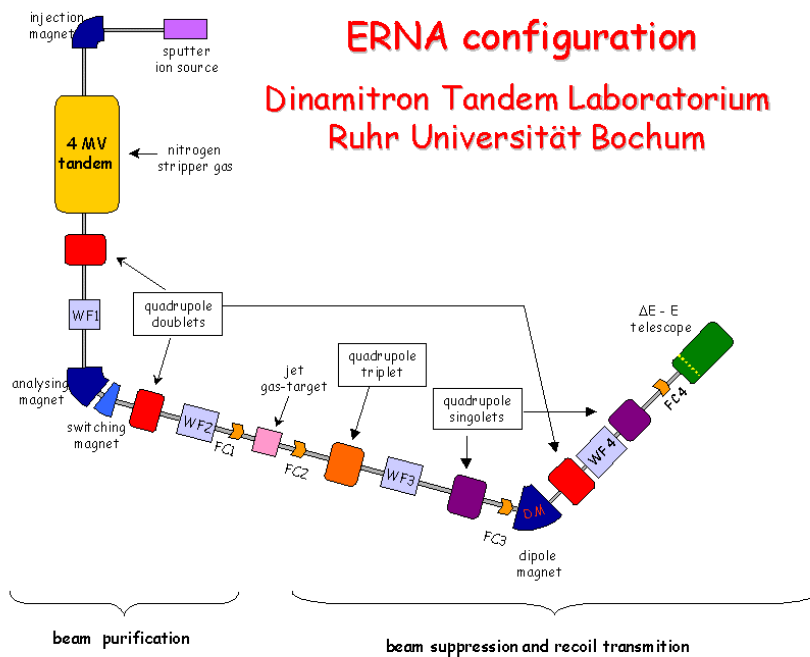Figure 4.28: **Schematic diagram of the 4 MV Dynamitron tandem accelerator with relevant components and of the experimental setup (WF = Wien Filter, FC = Faraday cup, A = aperture) representing to a large extent the ERNA setup.**

directly in a $\Delta E - E$ telescope placed in the beam line at the end of the recoil separator. As already said in the first two points, each elements between accelerator and telescope must have an angle acceptance larger $\theta = 1.5°$ and a momentum acceptance larger than $\Delta p/p = 7\%$. Theoretical calculation has been done [87] in order well placed all the elements satisfying above requirements (fig. 4.29).

Since the ^{12}C projectiles and the ^{16}O recoils have essentially the same momentum and since the ^{12}C ion beam emerging from the accelerator passes a momentum filter (analysing magnet), a nearly complete elimination of any ^{16}O beam contaminant in the ^{12}C ion beam incident on the ^4He gas target is of utmost importance: the ^{16}O beam contaminant and the ^{16}O recoils cannot be distinguished in the recoil separator, because both have the same momentum (see fig. 4.30 panel **a** and **b**). For these reasons two velocity filters have been placed before the jet gas target (**WF1** and **WF2** in fig. 4.4). Using Wien filters **WF3** and **WF4** (fig. 4.28) the ^{16}O recoils are purificated by the leaky ^{12}C beam (see panel **c** of fig. 4.30). The experiments indicate that a free choice of the charge state for the ^{16}O recoils is possible (above it has been used $q_{^{12}C} = q_{^{16}O} = 3^+$). The, only, exception is the charge state combination $q_{^{12}C} = 3^+$ and $q_{^{16}O} = 4^+$, for which the momenta and velocities of ^{12}C and ^{16}O are identical (due to their mass ratio 3/4) and thus no filtering is possible with ERNA.

The total purification factor of the ^{16}O contamination of the ^{12}C incident beam is $\mathbf{P_{WF1}P_{WF1} < 2 \cdot 10^{-18}}$, while that of the $^{12}C^{2+}$ leaky beam contamination of the $^{16}O^{3+}$ recoil is $\mathbf{R_{rec} = 5 \cdot 10^{-18}}$. This equipment should allow us to measure the cross section down to an energy of $E = 0.7 \; MeV$, detecting directly the ^{16}O nuclei, in this way the possible systematic errors are minimized. The experiment will start taking data at high energy side ($E_{cm} \leq 3 \; MeV$) at the beginning of the 2001. Then the experiment will continue with run at lower energies in order to minimize the uncertainty in the unavailable extrapolation down to 300 keV for S factor. To better determine the E1 component and, by subtraction, the E2 one the ERNA collaboration plans to implement a BaF_2 γ detection array around the gas target and then perform a recoil-γ coincidence, that will produce almost background free spectra. Adding
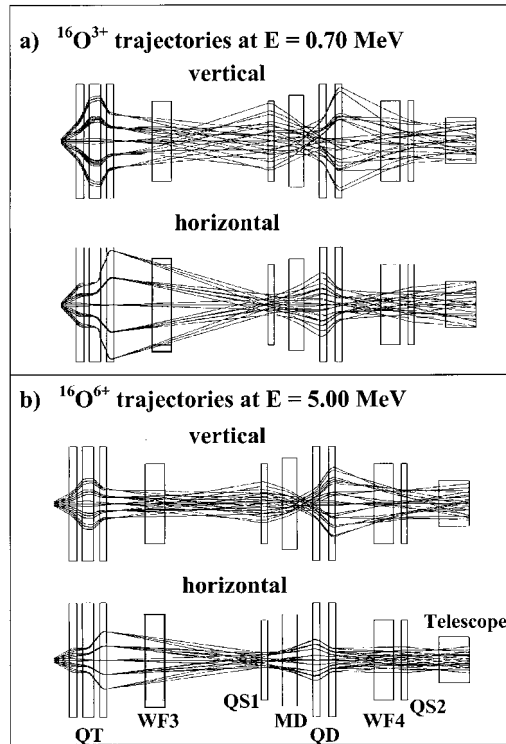
Figure 4.29: **Samples of the resulting $^{16}O^{3+}$ trajectories in the two orthogonal directions perpendicular to the beam axis, are shown for (a)** $E = 0.70$ MeV $(q_0 = 3^+$, $\theta_{max} = 1.9°$, $\Delta E = 0.13$ $MeV)$ **and (b)** $E = 5.0$ MeV $(q_0 = 6^+$, $\theta_{max} = 1.0°$, $\Delta E = 0.44$ $MeV)$. **The trajectories start at the jet gas-target** $(^4He$ **target density** $= 1 \cdot 10^{18} atoms/cm^2)$ **and are followed through the filtering and focusing elements of ERNA (indicated by square boxes) up to the telescope (WF = Wien Filter, QS = quadrupole singlet, QD = quadrupole doublet, QT = quadrupole triplet, MD = magnetic dipole).**
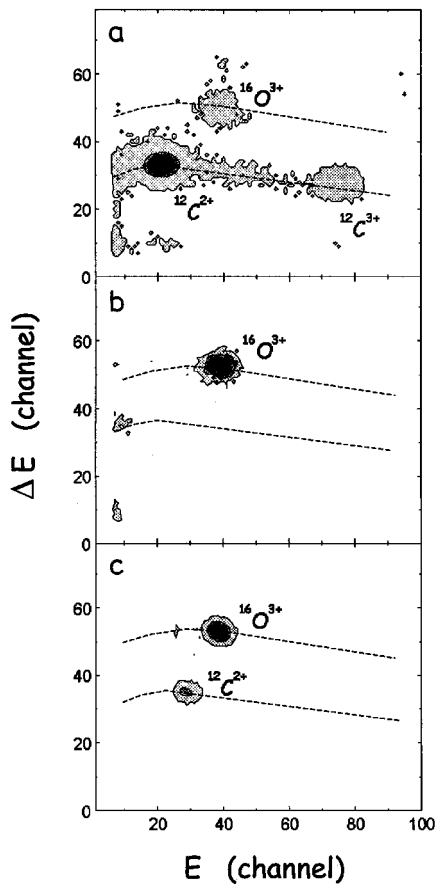
Figure 4.30: **The** $\Delta E - E$ **identification matrix for a** $^{12}C^{3+}$ **ion beam of** 10 MeV **is shown with (a) WF3 tuned to** $v(^{16}O) = 3/4v(^{12}C)$ **and (b) WF2 tuned to** $v(^{12}C)$ **and WF3 tuned to** $v(^{16}O)$. **In the case (a), the injection magnet of the ion source was set at mass 12, and in the case (b) it was set at mass 16: the contaminant** ^{16}O **beam appears at the same point in the matrix. Another identification matrix for the above** ^{12}C **ion beam is shown in (c) with WF1 and WF2 off while WF3, the dipole magnet, and WF4 were tuned to** $v(^{16}O)$. **The dashed curves correspond to the expected locations of** ^{12}C **and** ^{16}O **ions in the matrix.**

134

these informations to that coming from high energy for the direct capture one can better constrain the fit at astrophysical energies.

4.5 Charge states of ^{16}O

Since the knowledge of the equilibrium charge state distribution is crucial to determine the nuclear cross section using the recoil mass separator technique, we have performed at the TTT-3 Naples machine a series of measurements of ^{16}O charge state distributions [1]. Indeed, reminding equation 2.21:

$$\sigma_r(E_{cm}) = \frac{N_r}{N_{el}} \frac{l_{eff}^{el}\Omega_{lab}(\Omega_{cm}/\Omega_{lab})}{(\Phi_q\ \varepsilon_r)}\ \sigma_{cm}(\theta, E_{cm}) \tag{4.1}$$

we have to know the abundance of the selected Φ_q charge state coming out from the gas target with the highest possible precision. We have already underlined (section 3.2.1) that we need not only the equilibrium charge state distribution, but, also, the dependence of the charge states on the pressure. Indeed, the ^{16}O recoils can be created everywhere in the gas target: therefore, if $\mathbf{z}$ is the reaction coordinate along the beam axis with its origin at the entrance of the collimator, $\mathbf{x = l - z}$ is the path of recoils in the gas during which, because of the interactions with atomic electrons, they can change their charge state, eventually reaching the equilibrium if the thickness is large enough. In any case the path length $\mathbf{x}$ (with $\mathbf{0 \leq x \leq l}$) at pressure $\mathbf{p_0}$ is equivalent to a path length $\mathbf{l}$ at pressure $\mathbf{p}$ (with $\mathbf{0 \leq p \leq p_0}$). It is then possible to study the dependence of the recoil charge state distribution at the exit of the gas target as a function of the reaction coordinate $\mathbf{z}$ by measuring it for a fixed path $\mathbf{l}$ as a function of pressure. As we are interested in $^{16}\mathbf{O}$ recoils, we have used $^{16}\mathbf{O}$ beams from the accelerator with different energies and initial charge states to simulate the process taking place since the formation of the recoil in the actual experiment. During the measurements we changed the pressure of the helium target between 0 and 5 $mbar$.

---

[1]This experiment has been partially supported by the *Federico II* University of Naples, by means of the so called *"Progetto giovani ricercatori"*.

Table 4.4: In table there are the results for 5.2 *MeV* energy beam and 3^+ and 5^+ incident charge state. We report the percent of every charge state current for each measured pressure.

q (inc.) 3^+ E (MeV) 5.2 MeV							q (inc.) 5^+ E (MeV) 5.2 MeV						
P (mbar)	charge state probability (%)						P (mbar)	charge state probability (%)					
	1	2	3	4	5	6		1	2	3	4	5	6
0.000	0.0	1.8	93.3	1.5	3.2	0.2	0.000	0.0	0.1	0.7	9.1	88.2	1.9
0.005	0.0	7.0	73.7	15.4	2.7	0.1	0.010	0.0	0.0	5.1	30.3	64.6	0.0
0.010	0.0	8.2	60.3	26.6	4.6	0.3	0.025	0.0	2.0	14.8	44.8	38.3	0.0
0.050	0.0	11.0	35.9	41.9	10.0	0.6	0.100	0.0	9.0	33.9	42.2	13.5	1.3
0.100	0.0	8.0	34.2	44.2	13.2	0.4	0.200	0.0	8.4	33.7	42.3	14.4	1.2
0.200	0.0	8.8	34.0	43.3	12.7	1.0	0.350	0.0	8.3	33.4	42.8	14.3	1.2
0.350	0.0	8.2	32.8	44.1	13.8	1.0	1.000	0.0	8.7	33.8	42.3	14.7	1.2
1.000	0.0	7.8	33.7	43.0	14.3	1.2							

Table 4.5: **In table there are the results for 3.2 MeV energy beam and 3^+, 4^+ and 5^+ incident charge state. We report the percent of every charge state current for each measured pressure.**

q (inc.) 3^+						
E (MeV) 3.2 MeV						
P (mbar)	charge state probability (%)					
	1	2	3	4	5	6
0.000	0.0	5.9	81.0	10.7	1.2	0.0
0.010	0.0	28.3	54.6	15.7	1.3	0.1
0.050	0.0	32.5	45.5	19.0	2.4	0.6
0.080	0.0	33.8	44.6	18.7	2.3	0.5
0.100	0.0	33.0	46.3	18.4	2.1	0.1
0.150	0.0	32.3	46.5	19.2	1.8	0.1
0.500	0.0	35.9	44.7	17.2	1.8	0.3

q (inc.) 4^+						
E (MeV) 3.2 MeV						
P (mbar)	charge state probability (%)					
	1	2	3	4	5	6
0.000	0.0	1.7	14.8	79.5	4.0	0.0
0.100	0.0	32.2	48.3	17.6	1.9	0.0
0.500	0.0	33.8	43.6	20.4	2.2	0.0
1.000	0.0	32.0	46.0	20.0	1.8	0.0

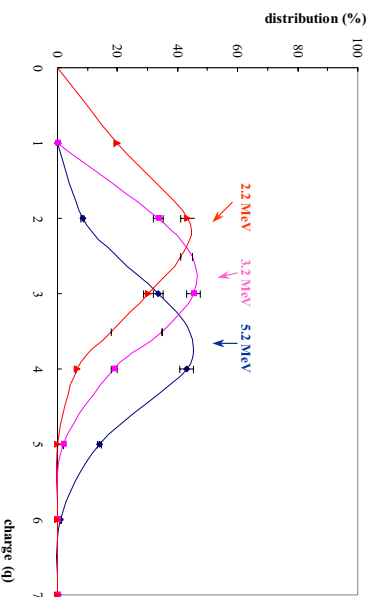| q (inc.) 5^+						
E (MeV) 3.2 MeV						
P (mbar)	charge state probability (%)					
	1	2	3	4	5	6
0.000	0.0	0.8	4.4	24.1	70.1	0.6
0.010	0.0	8.8	26.9	45.9	18.4	0.0
0.025	0.0	19.6	45.0	29.8	5.5	0.0
0.050	0.0	28.6	46.6	22.1	2.7	0.0
0.100	0.0	33.6	45.2	18.9	2.2	0.0
1.000	0.0	33.8	46.0	18.3	1.9	0.0

Figure 4.31: The figure shows the equilibrium charge state distributions considering data with pressure larger than 0.1 *mbar* for the three energies (5.2 *MeV*, 3.2 *MeV* and 2.2 *MeV*) taken into account.

Concerning the energies of the ^{16}O beam we remind that if we consider for the $\alpha(^{12}C, \gamma)^{16}O$ reaction a ^{12}C beam of energy E_b, this corresponds to a center of mass energy of $E_{cm} = 4/16 \cdot E_b$ and a ^{16}O recoil energy of $E_r = 12/16 \cdot E_b$. Therefore we obtain that $\mathbf{E_{cm} = 1/3 \cdot E_r}$. Since we are interested in $\mathbf{E_{cm}}$ values between 0.7 *MeV* and 3 *MeV* - which cover the relevant energy range for the measurement of the $\alpha(^{12}C, \gamma)^{16}O$ -, we have considered ^{16}O beams of energy of 2.2 *MeV*, 3.2 *MeV* and 5.2*MeV*. These energies correspond to 0.73 *MeV*, 1.02 *MeV* and 1.73*MeV* center of mass energy. We have also used different incident charge states, to investigate on the differences in reaching the equilibrium charge state distribution for incident beams of equal energy as a function of the pressure of the gas target.

The procedure followed during the experiment was: we have tuned, first, the ^{16}O beam of the selected charged state on the Faraday cup (FC6 in fig. 3.11) in front of the $\Delta E - E$ telescope. After having filled the gas target with helium, each charge state q, populated after of the interaction with the gas target particles, was retuned through the recoil separator, using the switching magnet to select the different values of q: $\mathbf{B\rho \propto \sqrt{ME}/q}$. The corresponding analyzed current $\mathbf{I_q}$ was measured in the

Faraday cup. The values

$$f_q = \frac{\frac{I_q}{q}}{\sum_q \frac{I_q}{q}} \qquad (4.2)$$

yield the probability of charge state **q** for a given energy, incident charge state and gas pressure. The behaviour of the $\mathbf{f'_q}$'s versus the pressure shows how the charge state distribution approaches the equilibrium one with increasing tickness of the target, while the $\mathbf{f_q}$'s at sufficiently high pressure as a function of **q** display the equilibrium charge state distribution.

In tables 4.4, 4.5 and 4.6 we report the results of all the measurements which we have performed. The first thing which is worth to note is that for pressures larger than 0.1 *mbar* the outgoing charge states reach the equilibrium distribution. This indicates that in all cases the equilibrium thickness is $\tau < \mathbf{9.1 \cdot 10^{16} atm/cm^2}$. Fig. 4.31 shows the equilibrium charge state distributions considering data with pressure larger than 0.1 *mbar* for the three energies taken into account. The lower is the energy the lower is the most abundant charge state. In particular for $E = 5.2\ MeV$ the most abundant are the 3^+ (33.5 %) and 4^+ (43.0 %) states, while for $E = 2.2\ MeV$ are the 1^+ (20 %), 2^+ (43 %) and 3^+ (30 %).

Figures 4.35, 4.34 and 4.33 show the outgoing charge state distribution as a function of the pressure for the different energy beams and incident charge states. Since the incident beam, interacting with helium, can receive or release one electron with cross sections σ^+ and σ^-, the outgoing distribution is progressively shifted from the initial, one peaked around the incident charge state, towards the equilibrium one.

The evolution of the charge state distribution versus particle thickness is described by a coupled differential equation system:

$$\frac{f_q(\tau)}{d\tau} = \sigma^-_{q-1} f_{q-1}(\tau) + \sigma^+_{q+1} f_{q+1}(\tau) - f_q(\tau)(\sigma^+_q + \sigma^-_q) \quad q = 0, z \qquad (4.3)$$

where f_q is the number of particles with charge state q, τ is the target thickness in atm/cm^2 and σ^+_q and σ^-_q are the cross sections of one electron gain or loss process rispectevely, considering the charge state q. Note that the initial condition is given

by the measurements at $\tau = 0$, i.e. gas target hempty. We have solved numerically the equation system 4.3, leaving as free parameter the cross sections σ^+ and σ^- for each charge state. Then, by compariison of the calculated values for $f_q(\tau)$ with the values measured at pressure $\mathbf{p} = (\tau \ \mathbf{p_0})/(\mathbf{n_0} \ \mathbf{l})$ (with p_0 and n_0 atmospheric pressure and number density), the free parameters can be determined. The fit to experimental data has been performed by a program which minimizes the χ^2 defined as $\chi^2 = \sum_j \left[\sum_i \frac{(N_{\tau_i} - f_q(\tau_i))^2}{\Delta N_i} \right]_{q_{inc}=j}$. The fit was performed simultaneously for the data corresponding to the same energy but different initial charge states. The results are shown in figures 4.35, 4.34 and 4.33. In can be seen that, for each incident energy, the same set of charge-exchange cross sections is able to fit the data corresponding to all incident charge states. The σ^+ and σ^- values extracted are shown in fig. 4.32, where it is possible to see that the probability to capture (σ_+) an electron decreases with the increasing charge state q of ^{16}O; the contrary is true for the transfer of an electron. Moreover, when the σ_+ and σ_+ cross sections have similar values then the corresponding charge state is the most populated (in figure it corresponds to the crossing of the two cross sections).

Summarising, the results for equilibrium charge state distribution indicate that the 2^+, 3^+ and 4^+ charge states for ^{16}O recoils should be used for the cross section measurements at the energies of $2.2 \ MeV$, $3.2 \ MeV$ and $5.2 \ MeV$ respectively. Concerning the pressure dependence of the recoil beam charge state distribution inside the gas target, it has to be noted that the equilibrium thickness is smaller, for the system investigated at the energies of interest, than the target thickness which is planned to be used in the jet gas target. However, if the cross section at the energies relevant for the measurements has resonances, one has to take into account the change induced by some non equilibrium effects in the charge state distribution. Indeed, because of the presence of the resonance also very small differences in the distribution could have large effects in the determination of the cross section to determine. In the case of flat cross section since the difference between gas target thickness ($\sim 10^{18} \ atm/cm^2$) and the equilibrium thickness ($\sim 9 \cdot 10^{16} \ atm/cm^2$) is large then it is possible to consider

Table 4.6: **In table there are the results for 2.2 *MeV* energy beam and** 2^+, 3^+ **and** 4^+ **incident charge state. We report the percent of every charge state current for each measured pressure.**

q (inc.) 2^+	E (MeV) 2.2 MeV					
P (mbar)	charge state probability (%)					
	1	2	3	4	5	6
0.000	3.9	73.5	15.7	6.6	0.4	0.0
0.010	10.0	44.7	35.2	8.6	0.5	0.0
0.050	18.7	42.8	29.5	8.8	0.3	0.0
0.100	18.2	46.3	29.4	5.7	0.4	0.0
0.200	18.8	43.9	31.1	5.9	0.3	0.0
1.000	16.8	46.0	31.7	5.3	0.3	0.0

q (inc.) 3^+	E (MeV) 2.2 MeV					
P (mbar)	charge state probability (%)					
	1	2	3	4	5	6
0.000	0.0	31.8	53.2	12.4	2.5	0.0
0.050	24.7	43.0	23.7	8.6	0.0	0.0
0.100	24.9	41.1	27.4	6.6	0.0	0.0
0.500	27.6	39.1	27.9	5.3	0.0	0.0
1.000	18.5	44.0	31.2	6.3	0.0	0.0

q (inc.) 4^+	E (MeV) 2.2 MeV					
P (mbar)	charge state probability (%)					
	1	2	3	4	5	6
0.000	0.0	3.8	16.1	78.8	1.2	0.0
0.050	14.0	50.1	30.3	5.5	.0	0.0
0.100	21.6	45.0	26.4	7.0	0.0	0.0
0.200	20.2	44.0	29.8	6.0	0.0	0.0
0.500	18.5	42.1	30.9	8.5	0.0	0.0
1.000	21.6	45.0	26.4	7.0	0.0	0.0

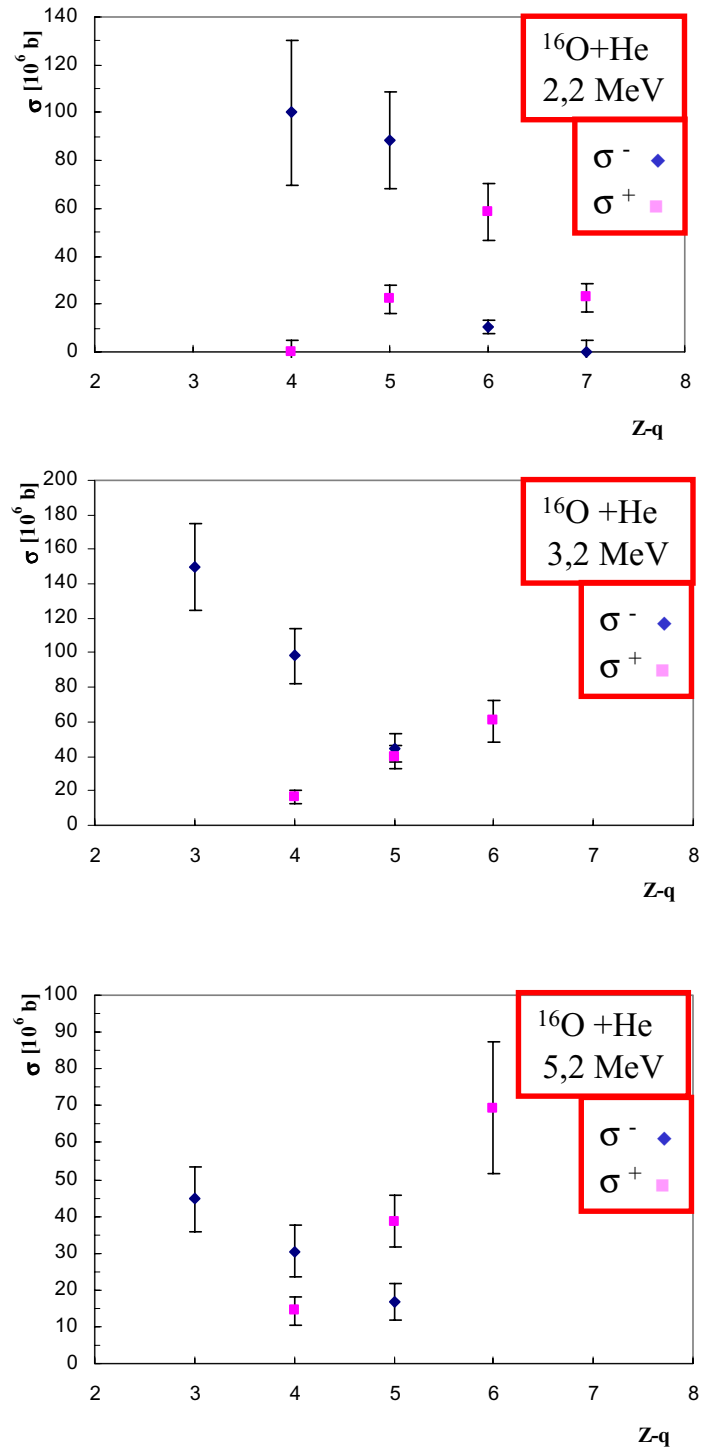that the charge state distribution is at the equilibrium.

142

Figure 4.32: **The σ^+ and σ^- values extracted are by the fit for each energy taken into account.**
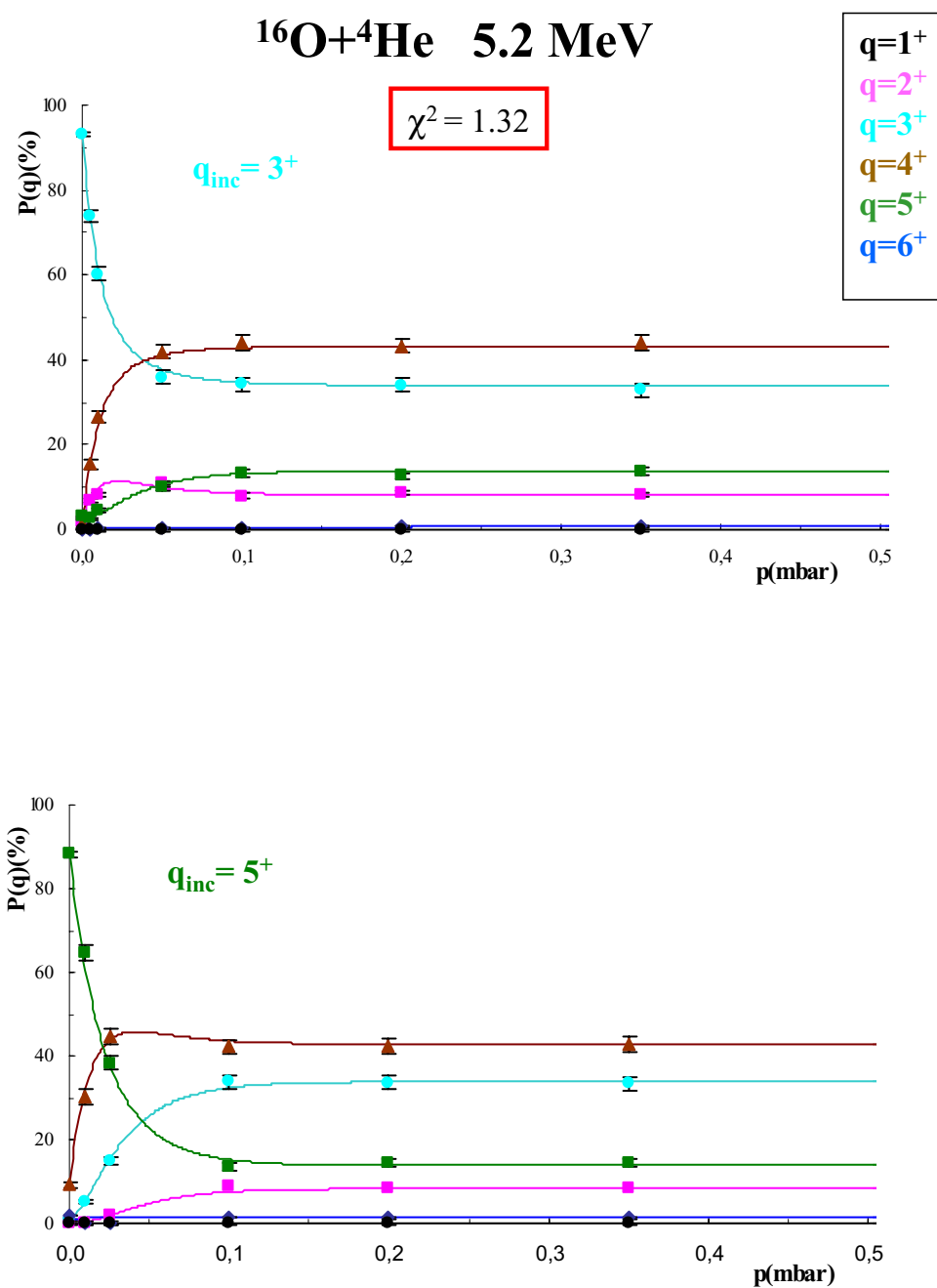
Figure 4.33: **The figure shows the outgoing charge state distribution as a function of the pressure for the** 5.2 MeV **energy beams and for** 3^+ **and** 5^+ **incident charge states.**

Figure 4.34: **The figure shows the outgoing charge state distribution as a function of the pressure for the** $3.2\ MeV$ **energy beams and for** 3^+, 4^+ **and** 5^+ **incident charge states.**
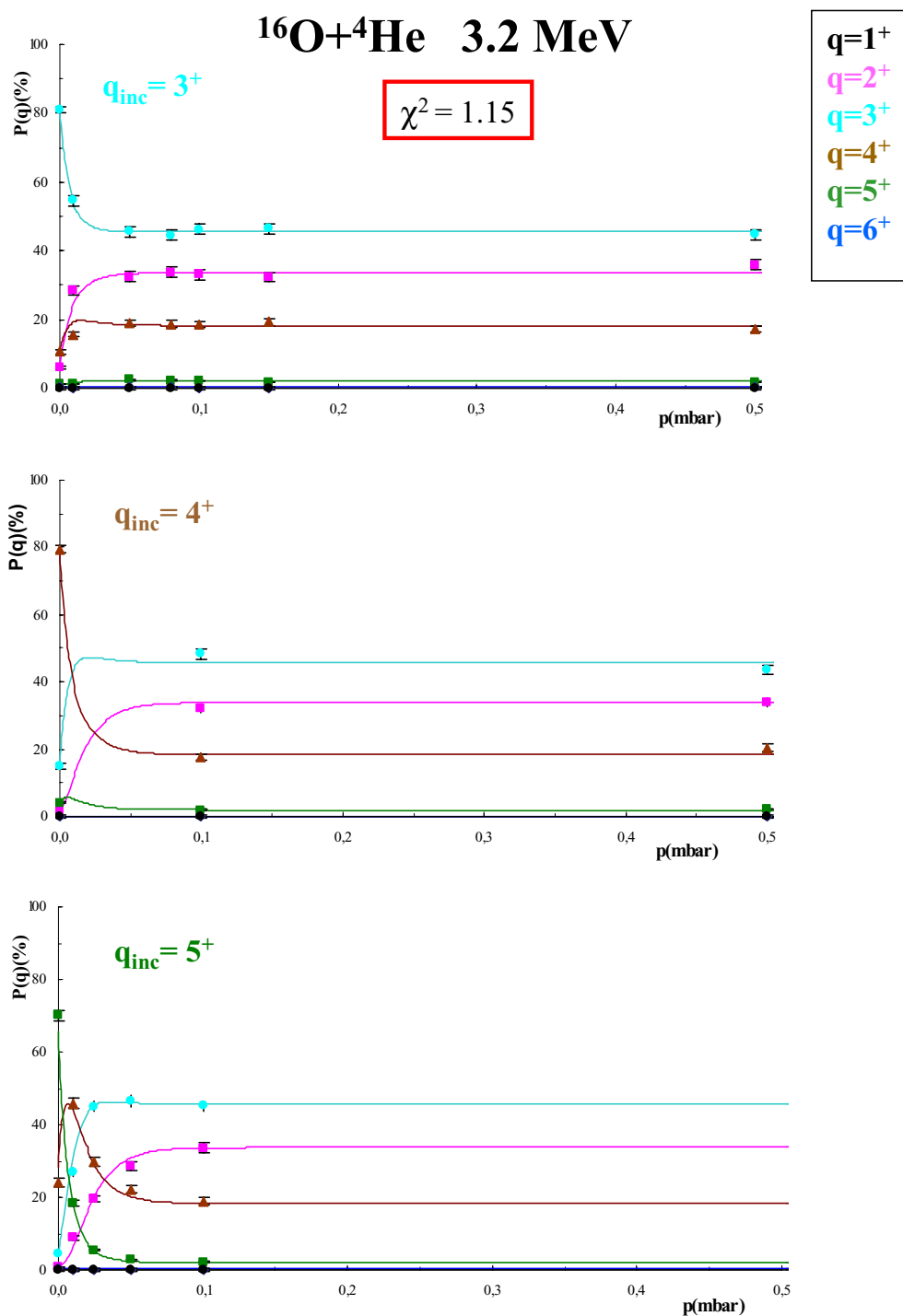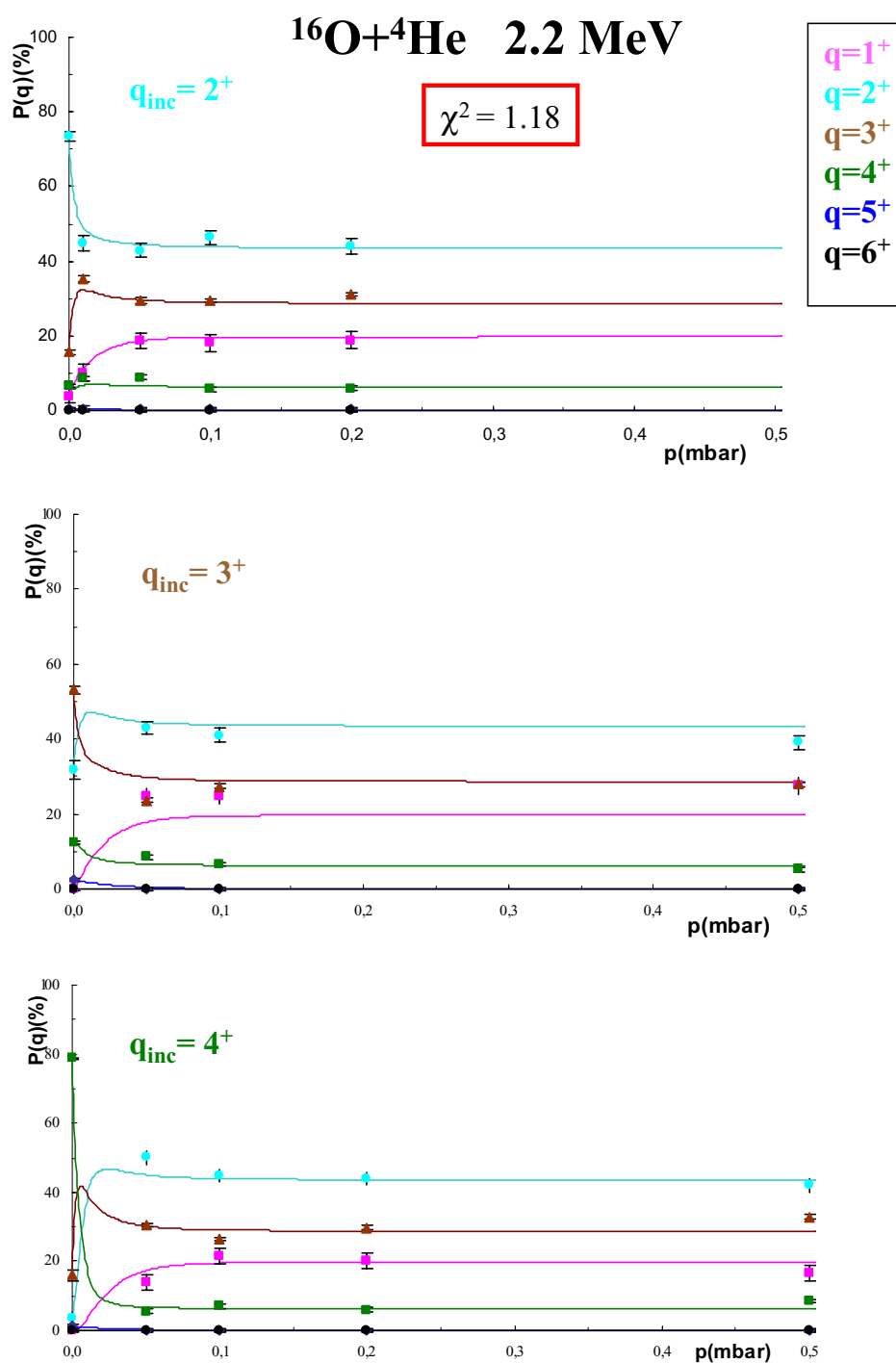
Figure 4.35: **The figure shows the outgoing charge state distribution as a function of the pressure for the** 2.2 MeV **energy beams and for** 2^+, 3^+ **and** 4^+ **incident charge states.**

Conclusions

In this thesis we have presented a new comprehensive study of two nuclear astrophysical S-factor (from both the experimental and theoretical points of view) which are of overwhelming importance in stellar astrophysics and, in turn, in fundamental physics. The first one, the $^7Be(p,\gamma)^8B$, is of crucial importance for the solar neutrino problems and hence to improve our basic knowledge about the physics of the neutrino and of its possible oscillation within the MSW framework. The second one, the $^{12}C(\alpha,\gamma)^{16}O$ reaction rate, plays a key role in almost all the advanced evolutionary phases of stars in a very wide mass interval.

We have estimated the expected neutrino flux from the Sun using the FRANEC evolutionary code and, by the comparison with the data of the five solar neutrino experiments, we have verified that there is no "astrphysical" nor "nuclear" solution for the so called Solar Neutrino Problem. It is not possible to solve this problem using the uncertainties in the physics and the nuclear inputs of the standar solar model; indeed, varying both the opacity and the nuclear cross sections we find an increase of the differences between the expected and measured fluxes. Moreover the possibility of the existence of Non-Standard Solar Models seems to be ruled out by the good agreement between SSM and helioseismological data. We need a neutrino physics beyond the standard electroweak model to change the neutrino energy spectrum after the neutrinos are produced in the center of the sun. The $^7Be(p,\gamma)^8B$ reaction can influence the interpretation of solar neutrino fluxes in the framework of the oscillation theory, in particular considering the MSW theory. Using the NACRE value $\mathbf{S_{17}(0)} = (\mathbf{21 \pm 2}) \ \mathbf{eV} \ \mathbf{b}$ for the astrophysical S-factor of the $^7Be(p,\gamma)^8B$ reaction we find a large

$(\mathbf{sin^2 2\theta = 0.977}$ and $\delta\mathbf{m^2 = 5.11 \cdot 10^{-5}\ eV^2})$ and a small $(\mathbf{sin^2 2\theta = (6.69^{+0.36}_{-0.34})} \cdot$
$\mathbf{10^{-3}}$ and $\delta\mathbf{m^2 = (3.54 \pm 0.12) \cdot 10^{-6}\ eV^2})$ mixing angle solutions in the framework of the MSW theory.

We have performed a new direct measurement of the absolute cross section of the $^1H(^7Be,\gamma)^8B$ reaction in inverse kinematics at $E_{cm} = 990\ keV$ using a novel approach: the Recoil Mass Separator method. We have accelerated a ^7Be radioactive beam using an hydrogen gas target, and measuring simultaneously the scattered proton ions at $45°$ and the ^8B recoils. To obtain the absolute value of the cross section taken into account we measured the elastic scattering cross section of the $^7Be + p$ elastic reaction and we find the value at the angle of $45°$:

$$\frac{\sigma_{cm}}{\sigma_{cm}^R}(45°, 990\ keV) = \frac{\sigma_{cm}}{\sigma_{cm}^R}(45°, 954\ keV) = 1.01 \pm 0.09$$

Finally, we find an astrophysical factor of $\mathbf{S(0) = (15.3 \pm 4.5)\ eV\ b}$, i.e. 30% smaller than the generally adopted vaue, which is $\mathbf{S(0) = (21 \pm 2)\ eV\ b}$. The inclusion of this value in the computation of solar models shows that a comparison between the theoretical predictions and the observation selects the small angle solution in the MSW framework for the solar neutrino problem; indeed, the χ^2 minimum for the large mixing angle is suppressed. The values of this solution are:
$\mathbf{sin^2 2\theta = (3.73^{+0.32}_{-0.33}) \cdot 10^{-3}}$ and $\delta\mathbf{m^2 = (3.53 \pm 0.12) \cdot 10^{-6}\ eV^2}$.

Concerning the second process, i.e. the $^{12}C(\alpha,\gamma)^{16}O$, we have discussed the experimental apparatus which has been set-up in Bochum by the jointed efforts of the Naples and bochum groups. The measurements of the cross section will start at the beginning of 2001. We have however extensively discussed how the new measurement will impact the stellar evolution models. Since this process works in a convective environment, we have, firstly, analyzed all the possible convective mechanisms active during the helium burning for the low mass and massive stars. Performing the evolution of stars in the mass range $\mathbf{0.8 \geq M/M_\odot \geq 25}$ and adopting two values for the $^{12}C(\alpha,\gamma)^{16}O$ cross section within the presently accepted uncertainty range we find these results for the central He burning phase:

1. the central He burning lifetime increases by less than 10% by changing between the low and the high value of this cross section;

2. the path followed by the stars in the HR diagram is essentially unaffected by such a change, apart from an upward shift (by almost one solar mass) of the upper mass limit which separates stars which experience a blue loop in the He burning phase from those which don't;

3. the timescales on which these stars move along their path in the HR diagram is not affected by a changing of the cross section in the quoted range;

4. the C abundance left by the He burning significantly depends on this rate.

Concerning the influence of the convective core on the final Carbon abundance left by the He burning we find that, as a general rule, it does not depend at all on the behavior (and size) of the convective core if its outer border does not vary in mass in the latest phases of the central He burning (i.e. when the central He drops below, say, 0.1 dex by mass fraction). On the contrary, the adoption of whichever mixing scheme which would allow a changing of the convective core during the latest phases of the central He burning would have a big impact on the final C abundance. As a consequence of this last point we stress that it is not wise to discuss the evolutionary phases beyond the He burning in terms of efficiency of this rate but only in terms of the C abundance left by the He burning. Only a better knowledge of this cross section and/or the physics of convection could help in removing the degeneracy between these two components. We also prolonged the evolution of the two 25 $M_\odot$ stellar models (evolved by adopting once the low and once the high value of the $^{12}C(\alpha, \gamma)^{16}O$ cross section) up to the core collapse and computed the relative final explosive yields. Our main results are that the intermediate-light elements, Ne, Na, Mg and Al (which are produced in the C convective shell) scale directly with the C abundance left by the He burning because they descend directly from the amount of fuel available (i.e C and or Ne). All the elements whose final yield is produced by any of the four explosive burnings (complete explosive Si burning, incomplete explosive Si burning, explosive

O burning and explosive Ne burning) scale inversely with the C abundance left by the He burning because the Mass-Radius relation in the deep interior of the star steepens as the C abundance reduces.

Since the knowledge of the charge state distribution is of fundamental importance in the Recoil Mass Separator method, we have studied the variation of the charge state distribution of ^{16}O as a function of the pressure and considering different incident energies in the relevant range for the measurement of the $^{12}C(\alpha, \gamma)^{16}O$ cross section. We have shown that the charge state distribution reaches the equilibrium for $p > 0.1 \, mbar$ (or equivalently for a thickness of $\mathbf{9.1 \cdot 10^{16} atm/cm^2}$) and we have measured the equilibrium charge state as a function of the incident energy. For pressures lower than $p < 0.1 \, mbar$ we have studied the evolution of the charge state versus the pressure.

Bibliography

[1] E.G. Adelberger *et al.*, Rev. Mod. Phys. 70(1998)1265

[2] Alexander, D. R. & Ferguson, J. W. 1994 ApJ, 437, 879

[3] C. Angulo *et al.*, Nucl. Phys. A656(1999)3

[4] Arnett, W.D. 1971 ApJ , 170, L43

[5] Arnett, W.D., 1972 ApJ , 176, 681

[6] R.E. Azuma et *al* 1993, Phys.Rev. C, 50, 1194

[7] Bahcall J.N., Basu S. and Pinsoneault M.H., 1998 Phys. Lett. B, 433, 1

[8] Bahcall J.N. and Pinsoneault M.H., 1995 Rev. Mod. Phys., 67, 781

[9] J.N. Bahcall, Solar Neutrinos, in Unsolved Problems in Astrophysics, Bahcall and Ostriker eds, Princeton University Press, 1997

[10] Bao, Z. Y:, & Käppeler, F. 1987, Atomic Data and Nuclear Data Tables, 36, 411

[11] Basu S. and Antia H.M., 1997 Mon. Not. R. Astron. Soc., 1997, 287, 189

[12] Basu S. and Antia H.M., 1997 Mon. Not. R. Astron. Soc., 1995, 276, 1402

[13] Beaudet, G., Petrosian, V., and Salpeter, E.E. 1967, ApJ, 150, 979

[14] Bethe, H.A., Rev. of Mod.Phys., 1937, 9, 69

152

[15] R. Bonetti, C. Broggini, L. Campajola, P. Corvisiero, A. DAlessandro, M. Dessalvi, A. DOnofrio, A. Fubini, G. Gervino, L. Gialanella, U. Greife, A. Guglielmetti, C. Gustavino, G. Imbriani, M. Junker, P. Prati, V. Roca, C. Rolfs, M. Romano, F. Schuemann, F. Strieder, F. Terrasi, H. P. Trautvetter, and S. Zavatarelli, 1999 Phys. Rev. Lett., 82, 5205

[16] Brunish, W.M., & Becker, S.A., 1990, ApJ , 351, 258

[17] L. Buchmann, R.E. Azuma, C.A. Barnes, J. Humblet, K. Langanke 1996 Phys.Rev. C , 54, 393

[18] L. Buchmann et al 1993, Phys.Rev.Lett.,70, 726

[19] Burbidge, G.R., Burbidge, E.M. Fowler, W.A. and Hoyle, F. 1957, Rev. Mod. Phys., 29, 547

[20] Campajola, L. et al., Nucl. Inst. Meth. B, 1987, 29, 129

[21] L. Campajola et al., Z. Phys. A, 1996, 356, 107

[22] Caputo, F., Chieffi, A., Tornambè, A., Castellani, V., and Pulone, L. 1989, ApJ, 340, 241

[23] Castellani, V., Chieffi, A, Pulone, L., and Tornambè, A. 1985, ApJ, 296, 204

[24] Castellani V., 1985 Astrofisica stellare Zanichelli Editore

[25] Caughlan, G.R., Fowler, W.A., Harris M.J. & Zimmerman, B.A., 1985, Atomic and nuclear data, 32, 197

[26] Caughlan, G.R. & Fowler, W.A., 1988, Atomic and nuclear data tables, 40, 283

[27] Chieffi, A., Limongi, M. and Straniero, O. 1998, ApJ, 502, 737

[28] Chieffi, A. & Straniero, O. 1989 ApJS, 71, 47

[29] Cowan, J. J., Thielemann, F. K., & Truran, J. M. 1991, Phys. Rep., 208, 267

[30] Davis, R.Jr., Harmer D.S., Hoffman K.C., 1968, Phys. Rev. Lett., 20, 1205

[31] Davis, R.Jr., 1993, in Frontiers of Neutrino Astrophysics, ed. Y. Suzuki, K. Nakamura, Tokio, Univ.Acad.Press

[32] Davis, R.Jr., Prog. Part. Nucl. Phys., 1994, 32 , 13

[33] P. Descouvemont and D. Baye, Nucl. Phys. A567(1994)341

[34] De Witt, H., Graboske, H., & Cooper, M. 1973, ApJ, 181, 439

[35] Dicus, D.A., Kolb, E.D., Schramm, D.N., and Tubbs, D.L. 1976, ApJ, 210, 481

[36] D'Onofrio, A., *et al.* to be published

[37] P. Dyer & C.A. Barnes 1974, Nucl. Phys. A, 233, 495

[38] Festa, G.G., and Rudermann, M.A. 1969, Phys. Rev. A, 180, 1227

[39] B.W. Filippone *et al.*, Phys. Rev. C28(1983)2222

[40] B.W. Filippone *et al.*, Phys. Rev. C, 1998, 28, 2222

[41] Fowler, W.A., Burbidge, G.R., Burbidge, E.M. 1955, ApJ, 122, 271

[42] Fuller, G. M., Fowler, W. A., & Newmann, M. 1982 , ApJS, 48, 279

[43] GALLEX Collaboration, P. Anselmann et al., 1995, Phys. Lett. B 342 , 440; GALLEX Collaboration, W. Hampel et al., 1996, Phys. Lett. B 388 , 364

[44] Garmany, C.D. & Massey, P. 1995 ApJ, 438, 188

[45] L.Gialanella *et al.*, Nucl. Instr. Meth. A, 1996, 376, 174

[46] Gialanella, L, 2000 Phd thesis

[47] Graboske, H., De Witt, H., Grossman, A., & Cooper, M. 1973, ApJ, 181, 457

154

[48] Grevesse, N. in Evolution of Stars: The Photospheric Abundance Connection, ed. G. Michaud and A. Tutukov, (Dordrecht:Kluwer), 63, 1991

[49] M. Half, G. Raffelt, A. Weiss, 1994 ApJ 425, 222

[50] F. Hammache *et al.*, Phys. Rev. Lett. 80(1998)928

[51] Haxton W. C., 1995, Annu. Rev. Astron. Astrophys, 33, 459

[52] Hoyle, F. 1954, ApJS, 1, 121

[53] Huebner, W.F., Merts, A.L., Magee, N.H., and Argo, M.F. 1977, Los Alamos Sci. Lab. Rept. (LA-6760-M) (LAOL)

[54] Iben, I., 1972 ApJ , 178, 433I

[55] Iben, I., 1968, Nature , 220, 143

[56] Iglesias, C. A., Rogers, F. J., & Wilson 1992 ApJ, 397, 717

[57] Iglesias, C. A., & Rogers, F. J. 1996, ApJ, 464, 943

[58] Itoh, N., Mitake, S., Iyetomi, H., and Ichimaru, S. 1983, ApJ, 273, 774

[59] Itoh, N., Totsuji, H., & Ichimaru, S. 1977, ApJ, 218, 477

[60] Itoh, N., Totsuji, H., Ichimaru, S, & De Witt, H. 1979, ApJ, 234, 1079

[61] N. Iwasa *et al.* Phys. Rev. Lett., 83(1999)2910

[62] C.W. Johnson *et al.*, Astrophys. J. 392(1992)320

[63] KAMIOKANDE Collaboration, Y. Fukuda *et al.*, Phys. Rev. Lett., 1996, 77 , 1683

[64] R.W. Kavanagh, Nucl. Phys. 15(1960)411

[65] R.W. Kavanagh *et al.*, Bull. Am. Phys. Soc. 14(1969)1209; R.W. Kavanagh, in Cosmology, Fusion and Other Matters, F. Reines ed., Colorado University Press, 1972

[66] R.M. Kremer et *al* 1988, Phys. Rev. Lett., 60, 1475

[67] Kurucz, R.L. 1991, in Stellar Atmospheres: Beyond Classical Model, ed. L. Crivellari, I. Hubeny, and D.G. Hummer (Dordrecht:Kluwer), 441

[68] Landau and Lifsits, 1977 *Fisica statistica* (Fisica teorica **5**), Editori Riuniti, Edizioni Mir

[69] Langer, N., Maeder, A., 1995, A& A, 295, 685J

[70] Limongi, M., Straniero. O. and Chieffi, A., 2000, ApJ, 129, 625

[71] Malaney, R. A., & Fowler, W. A. 1988, ApJ, 333, 14

[72] Mikheyev, SP and Smirnov A, 1985, Sov. J. Nucl. Phys., 42, 913

[73] Mikheyev, SP and Smirnov A, 1986, Nuovo Cimento 9C, 17

[74] Munakata, H., Kohyama, Y., and Itoh, N. 1985, ApJ, 296, 197

[75] Munakata, H., Kohyama, Y., and Itoh, N. 1986, ApJ, 304, 580

[76] Nakamura, T., Umeda, H., Nomoto, K., Thielemann, F., Burrows, A., 1999 ApJ, 517, 193N

[77] J.M.L. Ouellet et *al* 1992, Phys. Rev. Lett., 69, 1896

[78] J.M.L. Ouellet et *al* 1996, Phys. Rev. C, 54, 1982

[79] R. Plaga, H.W. Becker, A. Redder, C. Rolfs, H.P. Trautvetter, K. Langanke 1987, Nucl. Phys. A, 465 291

[80] P.D. Parker, Phys. Rev. 150(1966)851; Astrophys. J. 153(1968)L85

[81] Pontecorvo, B., 1958 Sov. Phys, JETP 7, 172

[82] G. Rafflet, Stars as Laboratories for Fundamental Physics, Chicago Press, 1996

[83] A. Redder et *al* 1985, Phys. Rev. Lett., 55, 1262

[84] A. Redder et *al* 1987, Nucl. Phys. A, 462, 385

[85] Richardson, M.B., Van Horne, H.M., Ratcliff, K.F., and Malone, R.C. 1982, ApJ, 255, 624

[86] Rogalla, D., Theis, S.,Campajola, L., D'Onofrio, A., Gialanella, L., Greife, U., Imbriani, G., Ordine, A., Roca, V., Rolfs, C, Romano, M. , Sabbarese, C., Schumann, F., Strieder, F., Terrasi, F., Trautvetter, H.P., Nucl. Inst. Meth. A, 1999, 437, 266

[87] Rogalla, D., Aliotta, M, Barnes, C.A., Campajola, L., D'Onofrio, A., Fritz, E., Gialanella, L., Greife, U., Imbriani, G., Ordine, A., Ossmann, J., Roca, V., Rolfs, C, Romano, M. , Sabbarese, C., Schumann, F., Strieder, F., Theis, S., Terrasi, F., Trautvetter, H.P., Eur. Phys. J. A, 1999, 6, 471

[88] Rogers, F. J., & Iglesias, C. A. 1992, ApJS, 79, 507

[89] Rolfs, C.E. and Rodney, W.S. 1988, Cauldrons in the Cosmos, University of Chicago Press

[90] G. Roters, C. Rolfs, F. Strieder, H.P. Trautvetter 1999, Eur. Phys. J. A, 6, 451

[91] SAGE Collaboration, V. Gavrin et al., in Neutrino 96, Proceedings of the XVII International Conference on Neutrino Physics and Astrophysics, Helsinki, edited by K. Huitu, K. Enqvist and J. Maalampi (World Scientific, Singapore, 1997), p. 14; V. Gavrin et al., inNeutrino 98, Proceedings of the XVIII International Conference on Neutrino Physics and Astrophysics, Takayama, Japan, June 1998, edited by Y. Suzuki and Y. Totsuka

[92] Sparks, W.M., and Endal, A.S. 1980, ApJ, 237, 130

[93] SRIM-2000, The Transport of Ions in Matter (Handbook of version 95.vi, New York, 1995)

[94] Straniero. O., Chieffi, A. and Limongi, M. 1997, ApJ, 490, 425

[95] F.Strieder *et al.*, Z. Phys. A, 1996, 355, 209

[96] F.Strieder *et al.*, Eur. Phys. J. A, 1998, 3, 1

[97] Strieder, F, 2000 Phd thesis

[98] Straniero, O. 1988, A&AS, 76, 157

[99] Straniero, O., Chieffi, A., Limongi, M., Busso, M., Gallino, R., and Arlandini, C. 1997, ApJ, 478, 332

[100] SuperKamiokande Collaboration, Y. Suzuki, in Neutrino 98, Proceedings of the XVIII International Conference on Neutrino Physics and Astrophysics, Takayama, Japan, June 1998, edited by Y. Suzuki and Y. Totsuka

[101] Terrasi, F. *et al.*, Nucl. Inst. Meth. B, 1990, 52, 259

[102] Testa, V., Ferraro, F., Chieffi, A., Straniero, O., Limongi, M., Fusi Pecci, F., 1999, AJ, 118, 2839T

[103] Thielemann, F. K., Arnould, M., & Truran, J. W. 1987, in *Advances in Nuclear Astrophysics*, eds. Vangioni-Flam, E., Audouze, J., Casse', M., Chieze, J. P., & Tran Thanh Van, J., Editions Frontieres, p.525

[104] F.J. Vaughn *et al.*, Phys. Rev. C2(1970)1657

[105] Wallace, R. K., & Woosley, S. E. 1979, Bull. Am. Astr. Soc., 11, 724

[106] L.Weissman *et al.*, Nucl. Phys. A, 1998, 630 678

[107] Wiesher, M., van Wormer, L., Görres, J., & Thielemann, F. K. 1992, in *International Conference on Radioactive Nuclear Beams*, ed. Delbar, T., Hilger, Bristol (UK), p.353

[108] C. Wiezorek *et al.*, Zeitsch. Phys. A282(1977)121

[109] Woosley, S.E. & Weaver, T.A. 1993 Phys. Rep., 227, 65

[110] Zoccali, M., Cassisi, S., Bono, G., Piotto, G., Rich, R.M., Djorysky, S.G., 2000, ApJ 538, 289Z